Wheel Load Reconstruction for Intelligent Vehicle Control

Kerst, S.M.A.A.

DOI
10.4233/uuid:e7ef8e46-c941-4bd7-a34d-69d78d0df115

Publication date
2020

Document Version
Final published version

Citation (APA)
Kerst, S. M. A. A. (2020). *Wheel Load Reconstruction for Intelligent Vehicle Control*. [Dissertation (TU Delft), Delft University of Technology]. https://doi.org/10.4233/uuid:e7ef8e46-c941-4bd7-a34d-69d78d0df115

Wheel Load Reconstruction *for* ***Intelligent Vehicle Control***

Stijn Kerst

Wheel Load Reconstruction for Intelligent Vehicle Control

Proefschrift

ter verkrijging van de graad van doctor
aan de Technische Universiteit Delft,
op gezag van de Rector Magnificus Prof.dr.ir. T.H.J.J. van der Hagen,
voorzitter van het College voor Promoties,
in het openbaar te verdedigen op
donderdag 22 oktober 2020 om 12:30 uur

door

Stijn Marcus Adriaan Antonius KERST

Master of Science in Mechanical Engineering,
Technische Universiteit Delft, Nederland
geboren te Raamsdonk, Nederland.

Dit proefschrift is goedgekeurd door de promotoren

Samenstelling promotiecommissie bestaat uit:

Rector Magnificus,	voorzitter
Dr. ir. R. Happee	Technische Universiteit Delft, promotor
Dr. B. Shyrokau	Technische Universiteit Delft, copromotor

Onafhankelijke leden:

Prof. dr. ir. J. Hellendoorn	Technische Universiteit Delft
Prof. dr. ir. B. De Schutter	Technische Universiteit Delft
Dr. A. Corrêa Victorino	University of Technology of Compiègne, France
Prof. A. Sorniotti	University of Surrey, UK

Overig lid:

Dr. ir. E. Holweg	ME Engineering

ISBN 978-94-6419-056-4

An electronic version of this dissertation is available at
http://repository.tudelft.nl/.

Summary

After decades of incremental change in the automotive industry, we now face an era of disruption as environmental concerns and social change propel the introduction of electric vehicles and vehicle automation. Besides the clear benefit of zero-emission transport for society, there is a strong commercial incentive for automated driving, as it will lead to more efficient and safer mobility. A vast amount of research and development is therefore dedicated to its realization.

As human drivers are progressively taken out of the loop, intelligent vehicles impose increasing demands on the highly complex control loop, from measurement and perception to vehicle control. Of particular interest are limit and critical conditions, as optimal performance in these situations is paramount to maximize safety. Therefore, accurate real-time knowledge of the wheel forces is essential, since it represents the tire-road interaction of the individual wheels, determining vehicle behaviour and its handling limits. However, no commercially feasible method is available for the measurement of these important vehicle states.

Current vehicle control systems circumvent this measurement issue by focusing on downstream effects, such as wheel slip and body accelerations. Due to the focus on secondary effects these systems are overly complex and lead to sub-optimal performance. For optimal vehicle control of future intelligent vehicles, therefore, the development of wheel force measurement is considered invaluable. By providing direct access to the most important control variables for dynamics control, such measurement allows for less complex control algorithms with improved performance and robustness, and hence will lead to safer mobility.

Although various approaches for the reconstruction of wheel forces have been developed, no cost effective method is yet available. This can be explained by the fact that load measurement approaches generally require mechanical load decoupling to avoid crosstalk, something that is difficult to achieve on a wheel-end suspension setup that is already complex on itself. In this thesis, a novel method for wheel force reconstruction is proposed via load measurement at bearing level.

The concept of bearing load measurement dates back to the early '70s and has been investigated by all major bearing manufacturers ever since. This has led to various measurement approaches based on relative ring displacement and outer-ring deformation. Despite all efforts, currently still no accurate nor robust approach for multi-dimensional load reconstruction is available. The state-of-the-art provides unsatisfying results due to the complexity of bearing behaviour and the inability of the currently applied data-driven methods to leverage unique bearing characteristics.

In this thesis a novel approach to bearing load reconstruction is proposed based on outer-ring deformation measurement and real-time simulation of bearing physics. The novel approach includes an explicit description of important physical effects as the rearrangement of rolling elements and the one-dimensional nature of their load transfer. As such it captures the bearing behaviour and allows to make use of its unique characteristics. The proposed approach is based on Kalman filtering and includes two independent physical models: a bearing strain model and a bearing load model.

The bearing strain model defines the outer-ring surface strain variation as a function of the local rolling element loading and location. The proposed model provides a simple though effective continuous and parameterized description of this behaviour. The model is implemented in an Extended Kalman Filter as a means of signal conditioning to estimate local rolling element forces from the measured outer-ring strain. By considering the change of strain due to the reallocation of rolling elements over time, a differential measurement is performed that results in invariance to thermal effects.

The proposed bearing load model is an extension of traditional rigid bearing modelling by a semi-analytical description of outer-ring flexibility. The latter is achieved by static deformation shapes and a Fourier series-based compliance approximation. The proposed model thereby provides a computationally effective but highly accurate description of rolling element forces for common bearing designs, in which significant raceway deformation occurs. Included in an Unscented Kalman Filter, the model provides the relationship between the estimated rolling element forces and the bearing loading and as such serves as a load reconstruction method. By explicit description of the individual one-dimensional element forces the approach considers the internal load decoupling effect and thereby limits cross-coupling on the estimated loads.

The wheel load reconstruction algorithm has been validated in both laboratory and field conditions on a production vehicle wheel-end bearing instrumented with

strain gauges. The study in laboratory conditions was performed on a bearing test setup at our industrial partner whereas the field validation has been performed on a dedicated test vehicle prepared as part of this thesis. Besides the proposed approach, a state-of-the-art algorithm and a variant including the model based signal conditioning method are evaluated to properly assess the results.

The experimental results show that the proposed approach leads to a considerable improvement in accuracy, reproducibility and robustness in comparison to the state-of-the-art data-driven approach. The proposed strain model-based conditioning approach leads to higher reproducibility and improved accuracy of up to 5 percent full scale due to its invariance to thermal effects and ability to discriminate in- and outboard rolling element forces. Additionally, the model-based load reconstruction method further improves accuracy by leveraging the internal bearing load decoupling behaviour to avoid crosstalk. This results in an improvement of over 5 percent full scale for combined loading conditions. Additionally, the approach is more robust, as important relationships are captured by modelling. The latter is well observed for loading conditions outside the calibration domain as an accuracy improvement of 6.8 to 18.4 percent full scale is achieved for the various reconstructed loads. The application of modelling furthermore leads to a significant reduction of parameters subject to calibration and provides physical meaning to these parameters.

Finally, an application study on anti-lock braking was performed to investigate both the load reconstruction performance in dynamic loading conditions and the advantages of load information for vehicle dynamics control. The study shows that sufficient signal bandwidth is provided and confirms the value of direct wheel force measurement for anti-lock braking control. In particular, as traditional difficulties like velocity estimation and slip threshold determination are circumvented whilst the effects of road friction fluctuations and brake efficiency are minimized.

By providing an accurate, robust and scalable solution for the processing of bearing outer-ring strain to the bearing loading, this thesis sets an important step towards a commercially viable solution for wheel-end load measurement. In addition, it is shown how this new information could push the boundaries of vehicle dynamics control. Next is the development of a suitable hardware setup to apply these results in a commercial solution, a topic currently pursued by the author.

Contents

Summary iii

1 Introduction 1
- 1.1 Research motivation . . . 2
  - 1.1.1 System analysis and control . . . 2
  - 1.1.2 Condition monitoring . . . 4
- 1.2 Bearing load measurement . . . 5
  - 1.2.1 Displacement-based methods . . . 6
  - 1.2.2 Deformation-based methods . . . 7
- 1.3 Aim of this thesis . . . 10
- 1.4 Thesis approach . . . 10
- 1.5 Contributions of this thesis . . . 11
- 1.6 Thesis outline . . . 12

2 Novel Bearing Load Model 13
- 2.1 Introduction . . . 14
  - 2.1.1 Coordinate systems . . . 14
- 2.2 Bearing model . . . 15
  - 2.2.1 Definition of element load and contact angle . . . 15
  - 2.2.2 Rigid body displacements of inner-raceway . . . 16
  - 2.2.3 Outer raceway modelling . . . 17
  - 2.2.4 Force and moment calculation . . . 18
- 2.3 Raceway deformation model . . . 18
  - 2.3.1 Static deformation shapes . . . 19
  - 2.3.2 Compliance approximation . . . 19
  - 2.3.3 Raceway deformation . . . 20
  - 2.3.4 Solution scheme for model solving . . . 21
- 2.4 Simulation based validation . . . 22
  - 2.4.1 Semi-analytical model setup . . . 22

2.4.2 Reference study setup 24
2.4.3 Single load simulation results 26
2.4.4 Combined loading simulation results 28
2.4.5 Discussion 30
2.5 Load distribution behaviour 31
2.6 Conclusion 32

3 Novel Bearing Strain Model 33
3.1 Introduction 34
3.1.1 Coordinate systems 36
3.2 Outer-ring deformation 36
3.2.1 Bulk deformation 38
3.2.2 Local deformation 39
3.2.3 Bulk and local deformation in frequency domain 41
3.3 Local strain model 42
3.4 Conclusion 43

4 Kalman Filter Based Load Reconstruction Algorithm 45
4.1 Introduction 46
4.1.1 Signal conditioning 46
4.1.2 Load calculation 47
4.1.3 Algorithm development 48
4.2 Bulk deformation data-driven approach 50
4.2.1 Signal conditioning 50
4.2.2 Load calculation 51
4.2.3 Tuning 51
4.2.4 Calibration 52
4.2.5 Running the algorithm 52
4.3 Local strain data-driven approach 53
4.3.1 Adaptive filters 53
4.3.2 EKF bearing strain model 54
4.3.3 Load calculation 56
4.3.4 Tuning 57
4.3.5 Calibration 57
4.3.6 Running the algorithm 57
4.4 Local strain model based approach 58
4.4.1 Adaptive filtering 59
4.4.2 EKF strain model 59
4.4.3 UKF bearing model 60
4.4.4 Calculation of load and deformation 62
4.4.5 Tuning 62
4.4.6 Calibration 62

4.4.7 Running the algorithm . . . 63
4.5 Conclusion . . . 63

5 Prototypes and Testing Facilities 65
5.1 Instrumented bearing prototype . . . 66
5.2 Bearing test system . . . 68
5.3 Test vehicle . . . 70
5.3.1 Miscellaneous . . . 70
5.3.2 Load estimation . . . 71
5.3.3 Dynamics control . . . 72
5.4 Test track . . . 73

6 Laboratory and Field Validation 75
6.1 Introduction . . . 76
6.2 Calibration . . . 77
6.3 Experimental results . . . 78
6.3.1 Test rig: Cornering and braking combined loading . . . 80
6.3.2 Test rig: Slalom manoeuver . . . 82
6.3.3 Test rig: Alternative loading . . . 84
6.3.4 Test vehicle: Cornering . . . 86
6.4 Discussion . . . 88
6.4.1 Bulk deformation data-driven approach . . . 89
6.4.2 Local strain data-driven approach . . . 90
6.4.3 Local strain model based approach . . . 90
6.5 Conclusion . . . 92

7 Anti-Lock Braking Application Study 95
7.1 Introduction . . . 96
7.2 Wheel corner dynamics . . . 97
7.3 Load based wheel slip derivative control . . . 98
7.4 Proposed anti-lock braking algorithm . . . 100
7.4.1 Phase 1 – decreasing wheel slip . . . 100
7.4.2 Phase 2 – increasing wheel slip . . . 101
7.4.3 Phase triggering mechanism . . . 101
7.4.4 Activation logic . . . 102
7.5 Experimental setup . . . 103
7.5.1 Bearing load measurement . . . 103
7.5.2 Brake torque control . . . 103
7.5.3 Test procedure . . . 103
7.5.4 Algorithm modifications . . . 104
7.6 Experimental results . . . 105
7.6.1 Reconstruction of wheel loading . . . 105
7.6.2 Anti-lock braking algorithm . . . 106

7.7 Conclusion 109

8 Discussion and Conclusion **111**
8.1 Reflection on the state-of-the-art 112
8.1.1 On conditioning 112
8.1.2 On load reconstruction 112
8.2 Concluding discussion 113
8.2.1 On bearing model development 113
8.2.2 On strain model development 113
8.2.3 On model-based strain conditioning 113
8.2.4 On model-based load reconstruction 114
8.2.5 On load-based anti-lock braking 114
8.3 Recommendations 115
8.4 Conclusion 116

Acknowledgements **119**

Curriculum Vitæ **121**

List of Publications **123**

Bibliography **125**

Propositions **135**

Chapter 1

Introduction

Rolling bearings are used in a wide variety of products and machinery for the rotational motion of shafts. They constrain components to the desired motion only and reduce friction between the moving parts. The low frictional interface is achieved by the use of rolling elements constrained between two raceways that provide limited rolling resistance and minimal sliding. Bearings find vast application in many domains, ranging from simple devices to highly complex mechanisms. As they often perform an essential role, much effort is put in research related to bearing technology.

In this thesis the topic of bearing load measurement is investigated in the context of vehicle state estimation and dynamics control. Although currently still a niche topic, bearing load measurement has much potential in the field of condition monitoring, offers promising possibilities for real-time system analysis and control and could support automated driving features.

1.1 Research motivation

Serving as the interface between static and rotating components, bearings are located at key locations and fulfil an essential role [33] in many systems. Bearing breakdowns often lead to product or system failure and, therefore, quality and reliability improvement is of great interest to both bearing manufactures and their customers. This is reflected by the extensive amount of research and development on topics such as condition monitoring [17, 24, 52, 90], lubrication, materials and mechanical design [68, 85].

In this thesis the topic of bearing load measurement is investigated from both a system and bearing level perspective as a valuable advancement in technology is foreseen in both areas. First of all, the measurement of bearing loads is valuable for system analysis and control, as bearings are often located at important system interfaces, as indicated in Figure 1.1. Additionally, load measurement could be used for self-diagnosis to complement the field of condition monitoring. As such, bearing load measurement would provide a valuable asset for future intelligent vehicles.

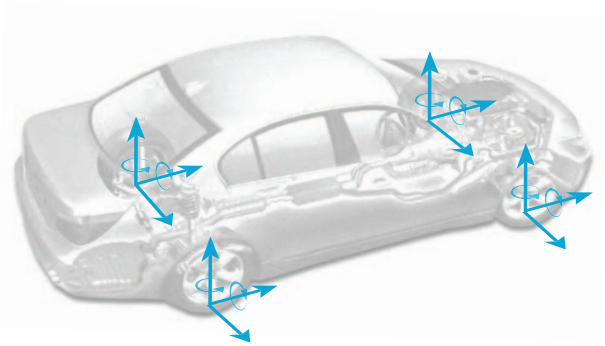

Figure 1.1: Bearing load measurement can be applied to determine wheel-end loading and therefore would form a valuable addition to vehicle dynamics control and safety functions

1.1.1 System analysis and control

Bearings provide the main support for system rotation and movement and as a result they are often located at the structure's main load path. Knowledge of the loads they transfer is therefore a valuable measure for system analysis, state estimation and/or control. Although a wide range of applications for various sorts of machinery could be considered, in this thesis special interest is given to load measurement on wheel-end bearings. This is of particular interest, as various application studies have shown promising results for wheel-end load estimation in the field of vehicle dynamics control and active safety systems. The numerous application examples of load-based dynamics control range from state estimation

[53, 57, 64, 84, 92] and anti-lock braking control [42, 75, 76, 89] to full chassis control [27, 29, 38, 83].

The usage of wheel loads in dynamic control and safety features is of interest, since force and moment information is more valuable than the currently available kinematic measurands. Force measurement provides a direct measure of the control variables and therefore allows for the design of less complex algorithms with enhanced performance, whilst robustness to changing conditions is maintained [42]. Forces can be measured at individual wheels, providing unique and valuable information on dynamic behaviour and tire slip states, that is of interest for vehicle safety functions, automated driving and overall redundancy in intelligent vehicles. The lack of application of force information in automotive systems is related to the fact that no accurate, robust and cost- effective measurement approach has yet been developed.

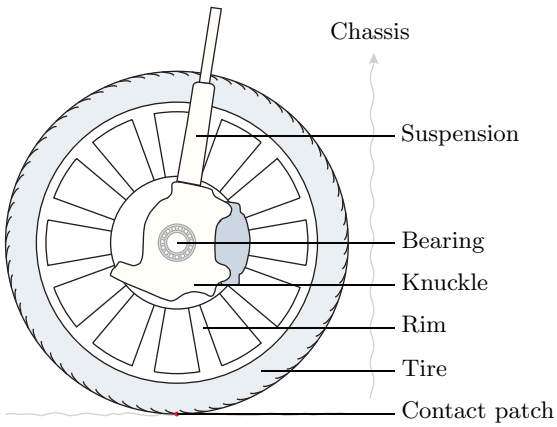

Figure 1.2: The various components that have been investigated for the reconstruction of wheel forces

In both academic research and industry, various approaches have been developed with the aim of estimating or measuring wheel forces. As indicated by Figure 1.2, many of the components located between the contact patch and chassis have been subject to study. This includes approaches based on: tire inner-liner acceleration [10, 11, 31, 51], tire sidewall deformation [28, 74, 91, 100], wheel rim deformation [80, 81], knuckle deformation [69], brake torque [1] and suspension deformation [9]. Additionally, various sensor-less approaches have been proposed [36, 93].

The commercial feasibility of any of these approaches depends on many factors, for instance the cost of instrumentation, complexity of the method, its robustness, the actual measured loads and their respective accuracy and precision. Often there is a trade-off to be made between the various aspects. Rim-based approaches for instance allow for accurate measurement of all wheel loads, but require an expen-

sive and complex mechanical structure to achieve this. Tire-based approaches on the other hand are based on a less expensive instrumentation, but are affected by factors such as wear and inflation pressure, furthermore they require wireless data acquisition and provide only limited force information.

A detailed investigation of the various wheel load measurement and estimation methods is not within the scope of this introduction. It can however be noted that the numerous developed approaches reflect the research community' interest in the field of wheel load reconstruction. The lack of any commercially available method on the other hand reflects the difficulty of developing an accurate, robust and cost-effective solution.

As noted, the lack of commercial success of any of the reconstruction approaches (to this day) is due to a variety of reasons. Several clear advantages of a bearing-based load measurement can be summarized that support its development:

- *Durability* - as the wheel-end bearing usually serves the entire vehicle lifetime
- *Robustness* - as it is invariant to tire and rim changes
- *Minimally invasive* - as only minor modifications are required
- *Location* - as measurement takes place at the first non-rotating part, considerably simplifying data acquisition
- *Weight* - due to the minor weight of the instrumentation
- *Degrees of Freedom* - as all relevant loads can be estimated (this thesis)
- *Quality* as high accuracy and bandwidth can be achieved (this thesis)

For these reasons, all major bearing manufactures have worked on the development of the bearing upgrade to load-cell [3, 47, 59, 67, 70, 94]. However, the state-of-the-art still includes numerous complexities that need to be resolved before commercialization of the concept could take place.

1.1.2 Condition monitoring

As in many facets of mechanical engineering, increasing demands are put on rolling bearings. This is reflected by numerous developments in areas such as lubrication, sealing and fatigue life. Considering their essence in machinery, special interest lies in lifetime prediction and fault detection of bearings in order to avoid unnecessary maintenance and breakdowns.

A wide variety of damage modes might cause premature bearing failure. Examples are numerous and include manufacturing errors, excessive or improper loading, misalignment, overheating, corrosion and lubrication failure [34]. Apart from premature failure modes, a bearing will eventually fail due to fatigue of the bearing

material. It is noted that bearing failure is one of the most common reasons for machinery breakdowns [99].

Incipient bearing failure is often characterized by a local defect on one of the bearing components; the detection of such defects is the main focus of condition monitoring [55]. Various approaches based on vibration [23, 25, 61, 72], acoustic emission [6, 60], sound pressure, lubrication [102] and thermal analysis [4, 54] have been developed for the detection and diagnosis of bearing defects [17, 24, 52, 90]. The large variety of methods developed for condition monitoring reflects the complexity and diversity of failure modes, as well as the interest in the topic.

Vibration or acceleration analysis is the most common approach in both academic research and industry and is based on various types on analysis in the vibration spectrum [23, 72]. Advantages of these approaches relate to the basic sensory equipment needed, their effectiveness and the ability to detect the location of the defect [25, 61]. Acoustic emission approaches have also been successfully applied and studies show that they allow for the detection of subsurface cracks before spalling occurs [6, 60]. The approach itself, however, is considerably more extensive as sensor location is crucial and signal processing is more complex. In lubrication analysis on- or off-line debris detection is applied on the bearing lubricant [102]. A major benefit of this approach is the independence of background noise and machine operating conditions; however, its drawbacks include processing complexity and classification. Thermal analysis-based condition monitoring approaches [4, 54] provide similar advantages and drawbacks. For improved fault diagnostics, combinations of different approaches and analysis techniques can be applied [66, 73].

Excessive loading, bearing misalignment or improper loading are the root cause for a considerable portion of bearing defect initiation and growth. As load monitoring enables for the detection of these improper conditions, it would allow for observation of the cause of defect initiation. The latter could result in earlier detection of bearing defects or allow for avoidance of defect growth by taking appropriate action in time, and is therefore considered a valuable development for condition monitoring.

1.2 Bearing load measurement

Research on the topic of bearing load measurement started decades ago, as reflected by numerous patent applications dating from the end of the 1970s [32, 50, 88]. Since then all major bearing manufacturers have filed a variety of patents on the matter. However, despite the large number of claims for patents, bearing load measurement is still a niche topic, if one considers the number of actual developed applications, which is limited to several custom-built industrial setups [65, 77, 96]. The lack of commercial implementation can be attributed to the lack of a scalable solution, as data-driven (in-situ calibrated) approaches are the norm due to a va-

riety of technical challenges. Additionally, market interest is an important factor for the scope of bearing load measurement. Although it has fluctuated over time, it is currently steadily increasing, driven by the popularity of data science, the increasing costs of system downtime and the decrease of component costs.

Load measurement at the bearing level can be classified by the measurand used for reconstruction, since either the relative inner- to outer ring displacement or the deformation of the stationary outer-ring can be used for load reconstruction. As both physical measurements are intrinsically different, they have different properties with respect to load reconstruction and their applicability.

1.2.1 Displacement-based methods

Displacement-based load measurement is founded on the fact that the rolling elements that separate inner- and outer bearing ring can be considered as spring elements. By measuring the relative inner- to outer ring displacement and understanding of the combined rolling element stiffness, the bearing load can be reconstructed. Considering for instance the one-dimensional case of Figure 1.3, it is easily understood that with knowledge of the displacement-force relationship the measurement of δ_x allows for the estimation of F_x.

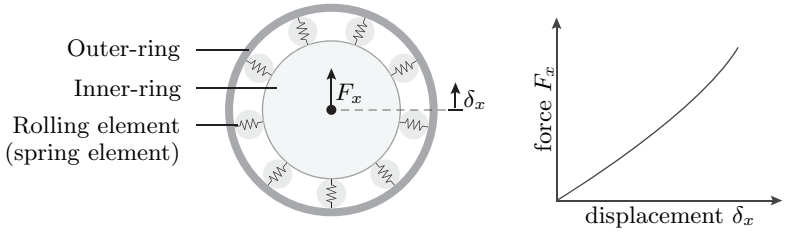

Figure 1.3: By measurement of displacement δ_x and knowledge of the displacement-force relationship bearing load F_x can be reconstructed

In order to measure the inner-ring displacement, various methods like hall effect [70, 101], eddy-current [22] and capacitive [77] sensing can be used. Depending on the location, orientation and amount of proximity sensing elements, the radial translation, axial translation and/or inclination of the inner-ring can be measured. By using a load-displacement relationship or stiffness matrix, either obtained by an experimental calibration or a simulation study, the respective bearing loads can be estimated. Figure 1.4 presents three approaches which respectively use hall effect (a) and eddy current (b) sensors in axial direction and capacitive sensing (c) in radial direction for the reconstruction of axial loading and moments (a and b) and radial forces (c).

Due to the early stage of development of the discussed methods, no validation studies reflecting on the quality of load estimation are available. Nonetheless, it

can be noted that none of the proposed setups is capable of reconstructing the bearing loading for all five[1] relevant Degrees of Freedom (DoFs). Although in theory this could be achieved by placement of sensing elements in both radial and axial direction, the practical implementation of this is debatable because of the space required and modifications necessary. Furthermore, the achievable accuracy for combined loading is questionable, as axial and radial displacement differ considerably in magnitude, which negatively affects the accuracy for combined loading. Based on these limitations, displacement-based methods are considered less feasible for full wheel-end load reconstruction.

1.2.2 Deformation-based methods

Deformation-based load reconstruction is widely used in applications such as load cells and is founded on the fact that any structure deforms when loaded. For load cells the structure is designed in such a way that a predictable or linear relationship between loading and deformation arises, such that an accurate reconstruction of the loading can be achieved. In deformation-based bearing load reconstruction, the non-rotating outer-ring strain is measured by the use of either strain gauges [47, 59, 67], ultrasonic sensors [13] or optical fibers [79, 96]. The non-rotating outer-ring is used, as this considerably simplifies both instrumentation and signal processing. Only limited changes to the bearing structure are made, usually only for instrumentation purposes, and thus any approach relies more heavily on signal processing. Regardless of the measurement technique applied, any strain measurement notes the superposition of two distinct deformation effects as described in [67] and depicted in Figure 1.5. According to [67], the two effects consider strain owing to the external force and strain due to the motion of rolling elements. Although this description is a simplification of the actual behaviour, and therefore

[1] In bearing load measurement the rotational degree of freedom provided by the bearing is not considered, in particular as it reflects internal friction and not external loading

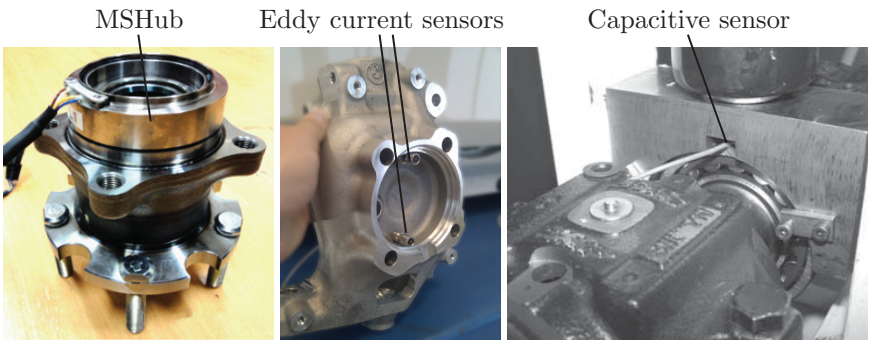

Figure 1.4: Three prototypes for displacement based bearing load reconstruction based on (a) hall effect [70], (b) eddy current [22] and (c) capacitive [77] sensors

is elaborated in this thesis, it serves well to describe the state-of-the-art in this introduction.

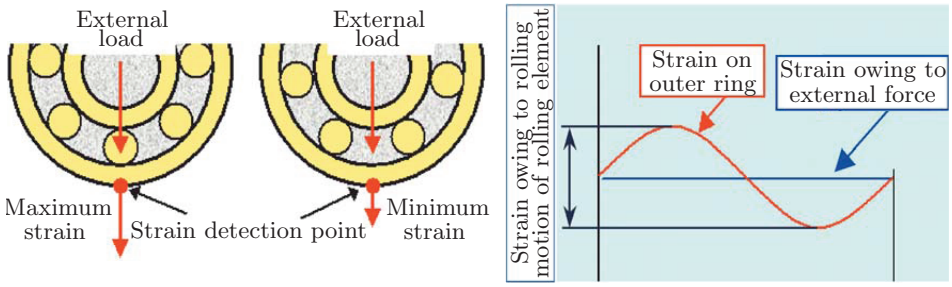

Figure 1.5: Differentiation of bearing strain from [67]

As both effects are informative for the bearing loading, an important aspect is the choice which deformation effect to focus on, as well as the method applied for conditioning. The former is of particular importance, since both deformation effects have rather distinct properties with respect to load reconstruction due to their different origin. Considering the state-of-the-art, it is observed that both effects have been considered by various bearing manufacturers [58, 67, 70, 94]. The strain due to the external force is for instance obtained by low-pass filtering in [58] and specific strain gauge design in [67]. The rolling element-related strain variance is conditioned using a peak-to-peak detection method and power calculation of the AC component in [58]. The former two methods were tested using the prototypes in Figure 1.6 (a) and (b) respectively, whereas the latter two are tested on (c).

From these studies several limitations with respect to signal conditioning are noted. Methods focused on the external force are limited due to influences of thermal effects [18, 37], whereas the strain variance-based approaches are limited in bandwidth, precision and applicability for double-row bearings [43].

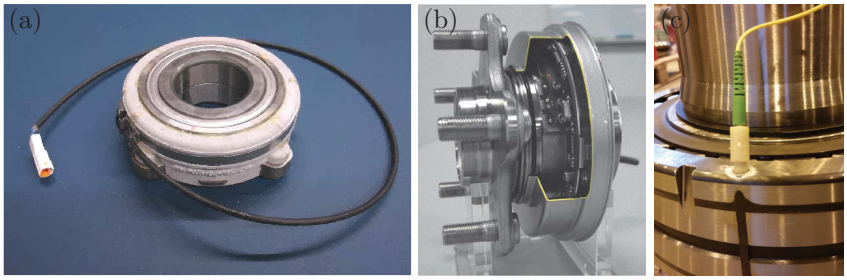

Figure 1.6: Bearing prototypes for deformation based load measurement considering strain gauges (a) [29] and (b) [67] and optical fibers (c) [96]

Besides the complexity in strain conditioning, the load calculation step is chal-

lenging because of the non-linear relationship between the conditioned strain and bearing loading, due to the behaviour of the rolling elements. In order to overcome this high non-linearity, current approaches aim for partial and/or case-specific solutions [22, 56, 95] or an artificial neural network approach [53]. Although attempts of piecewise linearization and neural networking may provide acceptable results in specific cases, as noted before, the scalability of such an approach is limited, as it inevitably leads to numerous parameters subject to calibration. Considering the tolerances in manufacturing, this would require extensive calibration of every load-sensing bearing. Even for small production sizes this would be an expensive and time-consuming procedure.

1.3 Aim of this thesis

The main aim of this thesis is to advance deformation-based bearing load reconstruction to a higher level with respect to load estimation dimensionality, scalability, accuracy and calibration effort. The result should form a basis for the future development of bearing load measurement and enable the development of load-based intelligent vehicle features and dynamics control.

In order to achieve this goal, the following research objective is defined:

To develop a generally valid bearing load reconstruction approach for the estimation of all relevant bearing loads while limiting the number of parameters subject to calibration

General validity refers to load estimation for all realistic loading conditions, without the necessity of external inputs or additional measurements. An important aspect of this thesis is the aim for invariance to thermal effects. In the meantime, the number of parameters subject to calibration should be kept at a minimum, in order to attain an effective calibration procedure for future commercialization.

It can be noted that the research objective aims to tackle the limitations of current data-driven approaches, since their case dependency, thermal errors and vast number of calibration coefficients limit their applicability.

1.4 Thesis approach

The initial goal of this thesis was to study the advantages of the application of bearing load measurement for vehicle dynamics control. For this purpose, a test vehicle was instrumented and modified and a novel load-based anti-lock braking algorithm was developed. During this study, presented in Chapter 7, it quickly became apparent that a significant advance in dynamics control could be achieved. However, it was also noted that the main challenge lies in the development of an effective bearing load measurement approach, due to the difficulties discussed in Section 1.2. It was therefore chosen to focus the thesis on the development and validation of bearing load measurement itself, as this would provide a more valuable contribution to research society.

With the available experimental setup in place and given the discussed lack of theory on bearing behaviour in load measurement, a research approach was defined. As previous data-driven studies on the topic had not resulted in an effective solution, a physics-based methodology was adopted.

1.5 Contributions of this thesis

With the aim of advancing bearing-based load reconstruction, the following contributions to the field are made:

- **Physics-based load reconstruction**
  This thesis proposes a completely novel method of solving the complex topic of bearing load reconstruction. A physics-based approach is presented by modelling the (i) bearing load to rolling element loads and (ii) rolling element loads to outer-ring strain. By explicit inclusion of both physical models, the non-linear system behaviour is captured effectively.

- **Model development for outer-ring local strain**
  Based on analysis of local deformation effects and with the cascaded physics perspective in mind, a local strain approximation model is proposed. The model describes the relationship between the local rolling element loads and the resulting local strain, and therefore can be used to extract rolling element loads from a strain gauge instrumented bearing.

- **Model development for flexible outer-ring bearing behaviour**
  The standard Harris bearing model is extended by a semi-analytical description of the outer-ring deformation. By the use of deformation shapes and a Fourier series compliance approximation, an accurate and computationally low-cost description of bearing and rolling element loads for flexible outer-ring structures is achieved.

- **Cascaded Kalman filter based load reconstruction**
  A cascaded Extended and Unscented Kalman filter approach, implementing respectively the strain and bearing model, is proposed. By a parallel EKF implementation of the strain model, rolling element loads can be effectively extracted from an instrumented bearing. The subsequent bearing model UKF leads to an accurate estimation of the bearing loading.

- **Load based anti-lock braking algorithm**
  An anti-lock braking algorithm is designed, based on bearing load information only. The proposed approach shows the potential applicability of wheel load information for vehicle dynamics control.

- **Experimental validation of proposed methods**
  An experimental study in both laboratory and field conditions is performed for the validation of the load reconstruction approach. Furthermore, the anti-lock braking algorithm is experimentally validated in field conditions, showing the potential of load-based dynamics control.

1.6 Thesis outline

The model-based algorithm for load reconstruction developed in this thesis considers bearing load and strain behaviour, which relate the bearing loading and outer-ring strain as indicated by Figure 1.7. In Chapter 2 and 3 both physical phenomena are studied to support algorithm development. In Chapter 2 the bearing load model is developed, providing a computationally low-cost but accurate description of bearing load behaviour. Furthermore, this Chapter provides a simulation-based validation study to assess the accuracy of the proposed methodology. In Chapter 3 bearing strain behaviour is studied, showing that bearing outer-ring strain can be categorized by bulk and local effects. The local effect is elaborated, and a model considering all important physical aspects is introduced.

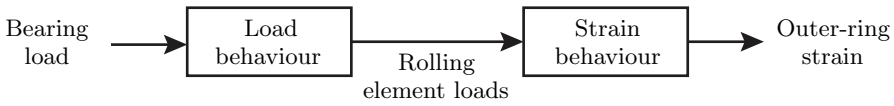

Figure 1.7: The two physical aspects that underlie the model based approach presented in this thesis

In Chapter 4 three load reconstruction algorithms are proposed, ranging from a state-of-the-art data-driven method to a full model-based approach using Kalman Filtering. A variety of algorithms is presented, as this supports an in-depth analysis of the advantages of the model-based approach. Chapter 5 then introduces the developed bearing prototypes and the laboratory and field setups that have been used in this thesis. Chapter 6 presents the experimental validation study of each of the algorithms. The study includes an extensive discussion to address the state-of-the-art of bearing load measurement, compared to the novel model-based approach for signal conditioning and load reconstruction. Following the validation study, in Chapter 7 an application study to the topic of anti-lock braking is presented, that shows the added value that bearing load measurement can provide in practice. Finally, in Chapter 8 a reflection on the work is provided through a discussion on the main results. Additionally, future work is discussed and final conclusions are drawn.

Chapter 2

Novel Bearing Load Model

Given the aim of developing a physics-based approach to bearing load reconstruction, an accurate and computationally efficient description of bearing loading and rolling element loading is paramount. Although various bearing modelling approaches have been introduced in both literature and industry in the past, the specific requirements for bearing load reconstruction limit the application of currently available models. In particular, real-time calculation and model accuracy for the relevant flexible outer-ring structures are essential. To meet these requirements, in this Chapter a novel semi-analytical bearing model is introduced. The proposed bearing model is founded on (computationally efficient) traditional rigid analytical bearing theory, but additionally introduces raceway flexibility for improved accuracy in common bearing designs with flexible outer-ring structures. The latter is included by the use of deformation shapes and a Fourier series-based compliance approximation. As the compliance is case-specific for each bearing setup, an approach tuning the Fourier coefficients by the use of a Finite Element study is introduced. The bearing load model is validated by the use of a comparison to well-established simulation software, showing good results for all test cases.

S. Kerst, B. Shyrokau and E. Holweg. "A semi-analytical bearing model considering outer race flexibility for model based bearing load monitoring", *Mechanical Systems and Signal Processing 104 (2018): 384-397*. [45]

2.1 Introduction

Modelling bearing behaviour for real-time load monitoring is a complex issue as an accurate description of the rolling element forces is desired whilst computing power is limited. Additionally, size and weight considerations during system and bearing development often results in flexible structures that deform considerably even at standard operational loads. The latter leads to altered load distributions, deflections, contact stresses and fatigue endurance compared to calculations using rigid assumptions. Considering the structural bearing deformation is thus of paramount importance for accurately describing rolling element loads and the bearing loading for the purpose of bearing load reconstruction.

Well established computational low cost analytical bearing models [20, 33, 39] are thus inapplicable due to their assumptions of rigidity. The usage of Finite Element Modelling [5], allowing for an accurate description of the flexibility, on the other hand is too computationally costly. Model reduction of for instance contact mechanics [16, 26, 48] or deformation behaviour [97] furthermore does not provide sufficient computational gain for real-time calculation. Therefore the most appropriate modelling approach for real-time load estimation is found in-between the analytical and Finite Element based approaches in the form of a semi-analytical flexible bearing model [8, 21, 49].

The semi-analytical flexible bearing models are formed by extension of traditional rigid analytical modelling by a semi-analytical description of the bearing outer-ring deformation. The in-plane deformation or ovalization of the outer-raceway is described using a Fourier series representation. The Fourier coefficients are either analytically derived from Timoshenko's theory [8, 21, 49] or determined based on a Finite Element Analysis of the structure [8]. A major limitation of the current modelling approaches is the assumption of axisymmetric geometries. This limits the applicability in real-life situations as bearing housings in general do not comply to this strict geometric limitation.

2.1.1 Coordinate systems

For the development of the bearing model two coordinate systems are used, namely a Cartesian and cylindrical system. Figure 2.1 shows the groove curvature loci of inner and outer race and their associated parameters in the Cartesian x, y, z space. The origin of the Cartesian space is located at the inner ring reference point at its initial position. The x and y-axis are respectively the vertical and horizontal radial bearing direction whilst the z-axis is aligned with the bearing axis. All rigid body displacements and bearing loads are defined in this Cartesian system. A cylindrical r, ψ, z system is used for description of the raceway approach and calculation of the rolling element loads. The origin and z-axis align with the Cartesian system and ψ is the angle between the r-axis and the Cartesian x-axis with $[-\pi \leq \psi < \pi]$.

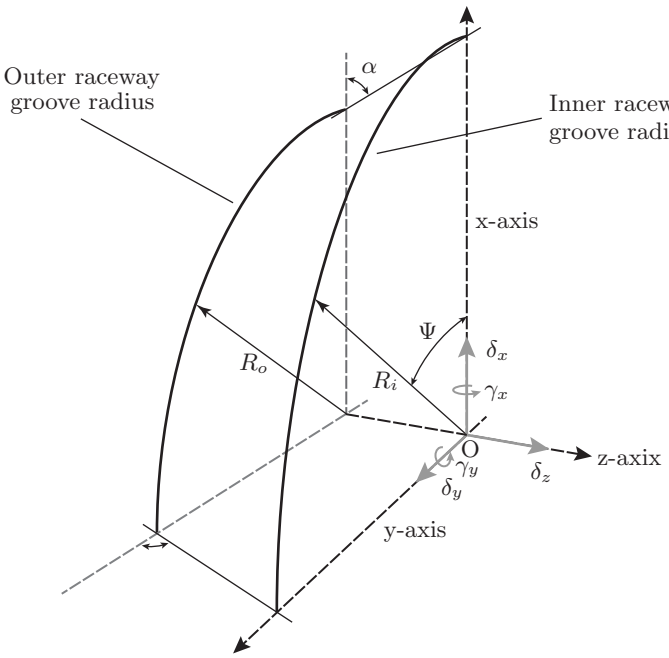

Figure 2.1: Loci of raceway groove curvature centres in Cartesian space

2.2 Bearing model

The following important assumptions and simplifications are applied: (i) as low speeds are considered the effect of centrifugal forces is neglected, (ii) both friction and cage interaction forces are neglected as they are insignificant compared to the rolling element normal loads and (iii) only radial deformation of the outer race is considered as the axial component in general is considerably less excited and influential. Furthermore some minor assumptions are provided within the work itself.

2.2.1 Definition of element load and contact angle

The rolling element loads are defined based on the deflection of the rolling elements by both raceways [33]. The ball-raceway normal load Q as function of deflection is defined as:

$$Q = K_n \delta_n^{2/3} \tag{2.1}$$

where K_n is the load-deflection factor and δ_n the sum of the normal approaches between rolling element and raceways. The load-deflection factor depends on the materials and curvatures of the bodies in contact and in this thesis is calculated in line with [33]. The normal approach δ_n is defined as the approach of the curvature

loci of the raceway grooves according to:

$$\delta_n = s - A \tag{2.2}$$

where s is the inner and outer race curvature loci distance and A is the curvature loci distance at first contact (and zero loading) defined as:

$$A = r_i + r_o - D \tag{2.3}$$

where r_i and r_o are respectively the inner and outer raceway groove curvature radii and D is the ball diameter. The inner and outer race curvature centre positions in the radial (R_i and R_o) and axial (Z_i and Z_o) direction are presented in Figure 2.2.

The overlap of the inner and outer groove raceway curvature centres is defined as:

$$s = \sqrt{(R_i - R_o)^2 + (Z_i - Z_o)^2} \tag{2.4}$$

and the operating contact angle α as:

$$\tan(\alpha) = \frac{Z_i - Z_o}{R_i - R_o} \tag{2.5}$$

2.2.2 Rigid body displacements of inner-raceway

In line with common literature [33] it is chosen to fix the outer ring in space whilst the inner ring is allowed for rigid body displacements. All five relevant DoFs are captured in the displacement vector that is attached to the inner ring at origin O

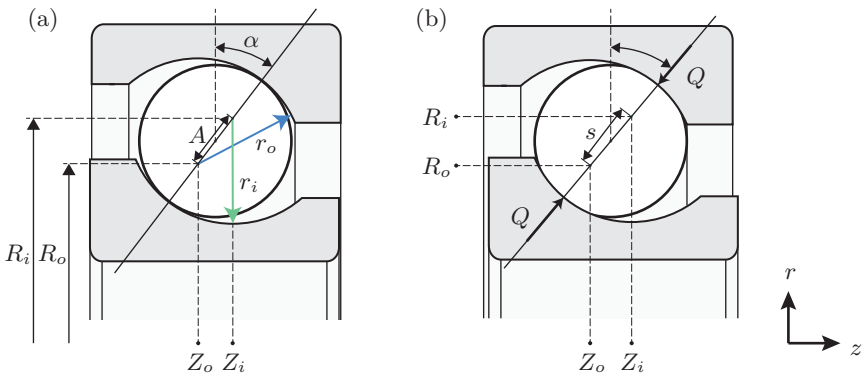

Figure 2.2: Radial ball bearing section view including relevant variables for (a) unloaded and (b) loaded conditions

as shown in Figure 2.1. The displacement vector is defined as:

$$\delta_D = \begin{bmatrix} \delta_x & \delta_y & \delta_z & \gamma_x & \gamma_y \end{bmatrix}^T \tag{2.6}$$

where δ_x, δ_y, δ_z are the axial translations, γ_x and γ_y are the rotations over the x and y-axis respectively. With the assumption of small angles the displacement vector defines the inner raceway groove curvature loci as a function of the bearing azimuth ψ in radial and axial direction according to:

$$R_i(\psi) = R_{i0} + \delta_x \cos(\psi) + \delta_y \sin(\psi) \tag{2.7}$$

$$Z_i(\psi) = Z_{i0} + \delta_z + R_{i0}\gamma_x \sin(\psi) + R_{i0}\gamma_y \cos(\psi) \tag{2.8}$$

where R_{i0} is the radius of locus of the inner raceway groove curvature centre and Z_{i0} is the initial axial displacement of the groove curvature centre.

2.2.3 Outer raceway modelling

The raceway deformation is accommodated by the use of a semi-analytical approximation model. The proposed implementation extends the classical static definition of the outer raceway groove curvature loci in radial direction:

$$R_o(\psi) = R_{o0} + u_r(\psi) \tag{2.9}$$

where R_{o0} is the static radius of the curvature loci and u_r the deformation of the raceway. For reasons of clarity the explicit description of the latter will be discussed in Section 2.3. As no deformation in axial direction is considered, the axial position of the groove curvature loci Z_o is static and equals Z_{o0}.

2.2.4 Force and moment calculation

The rigid body displacement vector δ_D and outer race flexibility model define the rolling element normal load Q and operating contact angle α for all bearing azimuth angles. The normal load Q can be resolved in radial and axial components:

$$Q_r = Q\cos(\alpha) \tag{2.10}$$

$$Q_z = Q\sin(\alpha) \tag{2.11}$$

where Q_r and Q_z are the radial and axial load respectively. Now introducing the index n for representation of the n^{th} rolling element and its corresponding ball azimuth position ψ_n, the bearing forces and moments can be described by summation over all rolling elements:

$$\begin{aligned} F_x &= \sum_{n=1..N_{re}} Q_{r,n}\cos(\psi_n) \\ F_y &= \sum_{n=1..N_{re}} Q_{r,n}\sin(\psi_n) \\ F_z &= \sum_{n=1..N_{re}} Q_{z,n} \\ M_x &= \sum_{n=1..N_{re}} Q_{z,n}R_m\sin(\psi_n) \\ M_z &= \sum_{n=1..N_{re}} Q_{z,n}R_m\cos(\psi_n) \end{aligned} \tag{2.12}$$

where N_{re} is the total number of rolling elements and R_m is the bearing pitch radius which equals $(R_i + R_o)/2$.

2.3 Raceway deformation model

Flexibility of the outer raceway is implemented by the use of a semi-analytical approximation of the static elastic radial bearing deformation. The deformation of any point on the raceway due to a single rolling element load can be deduced from the static components of the equation of motion:

$$u_r(\psi) = K^{-1}Q_r(\Psi) \tag{2.13}$$

where u_r is the race deformation in radial direction at azimuth position ψ, Q_r is the radial component of the applied load at azimuth Ψ and K^{-1} is the inverse stiffness or compliance. The latter represents a complex non-linear relationship between load and deformation and depends on mechanical properties, azimuth position ψ of interest and the azimuth Ψ of the applied load. Based on the principle

of superposition it is proposed to model the compliance by the use of a set of deformation shapes and related individual compliance approximation functions:

$$K^{-1} = \boldsymbol{\phi}(\psi)\boldsymbol{\Theta}(\Psi) \tag{2.14}$$

where $\boldsymbol{\phi}(\psi)$ is a column vector containing the set of normalized deformation shapes as function of azimuth position ϕ and $\boldsymbol{\Theta}(\Psi)$ is a row vector containing the compliance approximation as function of azimuth Ψ of the applied load. The former is dimensionless and the latter is of dimension $[m/N]$. In the following two subsections the static deformation shape vector $\boldsymbol{\phi}(\psi)$ and compliance vector $\boldsymbol{\Theta}(\Psi)$ will be defined respectively.

2.3.1 Static deformation shapes

The static deformation shapes define the deformation degrees of freedom of the bearing outer race. They allow for an effective and accurate representation of the normalized raceway deformation. A wavelike representation is proposed:

$$\boldsymbol{\phi}(\psi) = \Big[\sin(\psi m)_{m=1} \quad \cdots \quad \sin(\psi m)_{m=M} \quad \cos(\psi m)_{m=1} \quad \cdots \quad \cos(\psi m)_{m=M}\Big] \tag{2.15}$$

where each column represents a deformation shape as function of bearing azimuth position ψ. The number of deformation shapes is defined by M and can be set according to the detail of interest. A choice for (co)sinusoidal description with an integer wavelength is made as these are orthogonal and continuous (C^∞) over the entire bearing azimuth. The latter is important as the bearing elastic deformation should result in a continuous surface.

2.3.2 Compliance approximation

The compliance approximation is a vector composed of $2M$ compliance functions:

$$\boldsymbol{\Theta}(\Psi) = \begin{bmatrix} \theta_1(\Psi) \\ \vdots \\ \theta_{2M}(\Psi) \end{bmatrix} \tag{2.16}$$

where each compliance function $\theta_m(\Psi)$ describes the relationship between load Q at azimuth Ψ and the excitation of the m^{th} deformation degree of freedom. These functions depend on the location of the applied load and mechanical properties of the structure. To limit the function complexity only the load azimuth Ψ is considered whilst the effect of operating contact angle α is neglected. As the mechanical behaviour of a bearing can be considered periodic in nature, a Fourier

series approximation is proposed to cast the properties of the compliance. The following description for each compliance function is proposed:

$$\theta_m(\Psi) = \frac{1}{2}a_{m,0} + \sum_{k=1..K} a_{m,k}\cos(k\Psi) + \sum_{k=1..K} b_{m,k}\sin(k\Psi) \tag{2.17}$$

where a_m and b_m are the Fourier coefficients for deformation shape m and K is the order of the Fourier series. The Fourier coefficients are determined a priori based on the real deformation behaviour of the outer race structure. For the latter a Finite Element study on the flexible structure is adopted.

By the use of a Finite Element Analysis the raceway deformation $u^{ref}(\psi, Q(\Psi))$ is determined after applying load Q at azimuth Ψ and nominal contact angle α_0. Now combining equation 2.14 - 2.17 and substitution of $u_r(\phi)$ by $u^{ref}(\psi, Q(\Psi))$ one obtains:

$$\theta_m(\Psi) = \int_{-\pi}^{\pi} \frac{u^{ref}(\psi, Q(\Psi))}{\phi_m(\psi)Q(\Psi)} d\psi \tag{2.18}$$

The equation provides the Fourier function values for all $2M$ compliance functions for a load at azimuth Ψ. Now by performing a Finite Element study for load Q at multiple azimuths ranging from $[-\pi < \Psi \leq \pi]$ standard Fourier theory can be applied to obtain the Fourier coefficients for all $2M$ compliance approximation functions.

2.3.3 Raceway deformation

The single load-deformation relationship presented in this Section can be extended to an arbitrary number of deformation locations N_{def} and rolling element loads N_{re} for a complete description of the raceway deformation. Equation (2.19) shows how additional deformation locations (N_{def}) are added by extension of the static deformation shape vector/matrix with a row for each location of interest. Furthermore the amount of rolling element loads (N_{re}) can be increased by extending the compliance vector/matrix with extra columns and the load vector with additional rows.

$$\begin{bmatrix} u_r(\psi_1) \\ \vdots \\ u_r(\psi_{N_{def}}) \end{bmatrix} = \begin{bmatrix} \boldsymbol{\phi}(\psi_1) \\ \vdots \\ \boldsymbol{\phi}(\psi_{N_{def}}) \end{bmatrix} \begin{bmatrix} \boldsymbol{\Theta}(\Psi_1) & \cdots & \boldsymbol{\Theta}(\Psi_{N_{re}}) \end{bmatrix} \begin{bmatrix} Q_r(\Psi_1) \\ \vdots \\ Q_r(\Psi_{N_{re}}) \end{bmatrix} \tag{2.19}$$

2.3.4 Solution scheme for model solving

Due to the recursive dependency of the rolling element loads and raceway deformation an iterative approach is necessary for calculation of the rolling element and bearing loads for any displacement vector. Figure 2.3 presents the solution scheme for the proposed semi-analytical model.

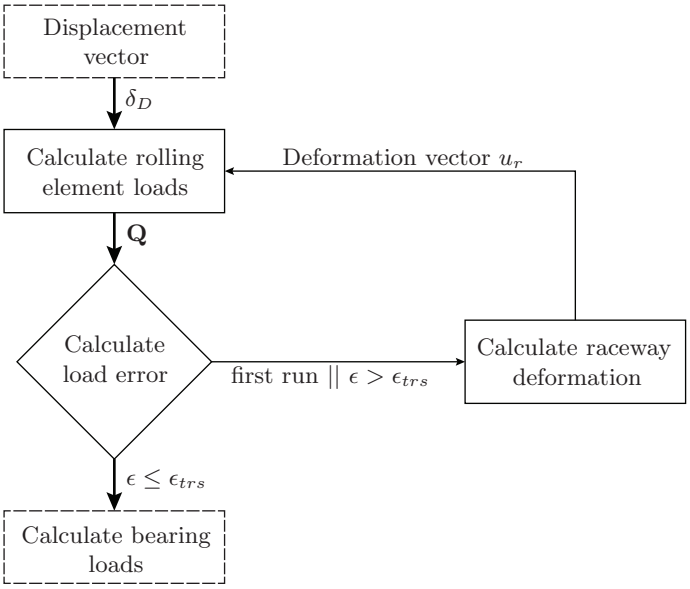

Figure 2.3: Solution scheme for the flexible bearing model

The iterative nature rises due to the 'calculate load error ϵ' block that compares the current and previously calculated rolling element loads in order to determine convergence of the raceway deformation. The load error ϵ is the summation of the absolute rolling element load differences. When this error is smaller or equal to the tolerance threshold ϵ_{trs} the model has converged, otherwise a new calculation cycle is performed. This latter is always done during the first run as the convergence criterion cannot be checked then. The value ϵ_{trs} is chosen based on the desired accuracy. Note that the presented approach can be optimized for stability and convergence; this however is not focused upon in this research.

2.4 Simulation based validation

The proposed model is validated by a comparison study with well-established SKF bearing simulation software [62, 63, 86, 87]. More specifically, the accuracy of the rolling element load distribution of the semi-analytical model is assessed in a variety of load cases by comparison to results obtained by the SKF BEAring Simulation Tool (BEAST). Next to the validation with respect to the BEAST reference model also the differences with respect to a rigid model are considered to assess the improvement with respect to traditional modelling. The latter model is obtained by setting $M = 0$ which effectively corresponds to the rigid modelling presented in [33].

The validation study considers a HBU3 bearing unit which is commonly used as wheel-end bearing in automotive applications. This double row angular contact ball bearing is designed to be light and compact. It provides its own housing and both the inner and outer-ring contain a flange for mounting to the wheel and knuckle respectively. The design considerations result in a relatively thin outer-ring which deforms considerably even at normal operating conditions. The bearing is therefore an ideal case study to assess the validity of the proposed model. Table 2.1 and Figure 2.4 provide the relevant parameters of the considered bearing.

2.4.1 Semi-analytical model setup

The semi-analytical model is set-up according to Section 2.2 and 2.3 by the use of the bearing parameters presented in Table 2.1. The model consists of two inner and outer raceways with the origin located as indicated in Figure 2.4. The inner raceways are considered rigid and their groove curvature loci are described by displacement vector $\boldsymbol{\delta}_D$. The outer races are considered flexible. The bulk deformation of both in- and outboard raceways is assumed identical and thus is

Table 2.1: Parameters of the double row ball bearing

Parameter	Description	Value
N_{re}	Nr. rolling elements	2x15
r_i	Inner raceway groove curvature	6.59 mm
r_o	Outer raceway groove curvature	6.73 mm
R_{i0}	Inner raceway groove radius	33.19 mm
R_{o0}	Outer raceway groove radius	32.69 mm
Z_{i0}	Axial offset inner raceway	8.44 mm
Z_{o0}	Axial offset outer raceway	8.81 mm
D	Rolling element diameter	12.70 mm
α_0	Nominal contact angle	36 deg
R_{ref}	Reference profile radius	$R_o + r_o$
	Axial interference	30 μm

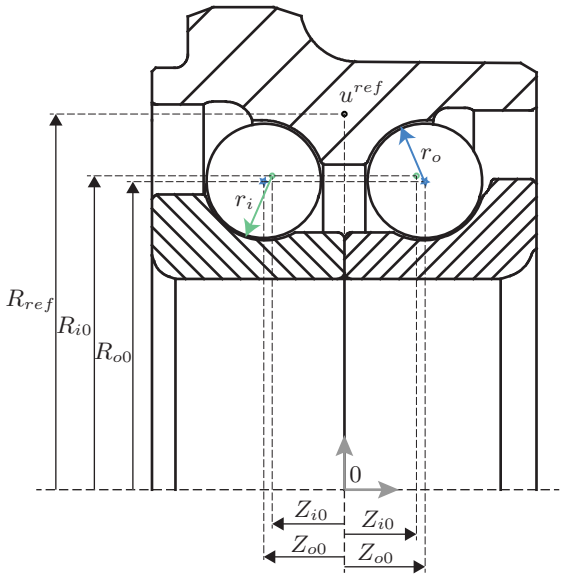

Figure 2.4: Cross-sectional view of the HBU3 bearing considered in this study

captured by a single set of deformation shapes.

The outer-ring geometry is modelled in a 3D CAD package and a Finite Element Analysis in COMSOL [14] is performed to determine the Fourier compliance coefficients. As the knuckle to which the bearing is mounted is relatively flexible, its influence cannot be neglected. Therefore the knuckle behaviour is studied as well, and a model reduction technique is applied such to reflect knuckle behaviour on the interface with the bearing model. The reduced system is used to determine bearing deformation behaviour in order to limit calculation effort.

The reference deformation profile $u^{ref}(\Psi)$ is determined in-between both raceways, as shown in Figure 2.4, at a constant interval over the full bearing azimuth as indicated in Figure 2.5. This latter figure also shows the azimuth interval distribution of the point load cases $Q(\Psi)$. The interval values are provided in Table 2.2. Note that each load $Q(\Psi)$ is applied individually whilst the FEA results of the 120 deformation points are used according to the procedure presented in Section 2.3 to determine the deformation model. In order to assess the effect of the number of deformation shapes on the model accuracy several model variants are determined with different values for M.

Table 2.2: Deformation and load parameters

Parameter	Description	Value
$\Delta\psi$	Deformation profile azimuth interval	3 deg
$\Delta\Psi$	Load azimuth interval	5 deg

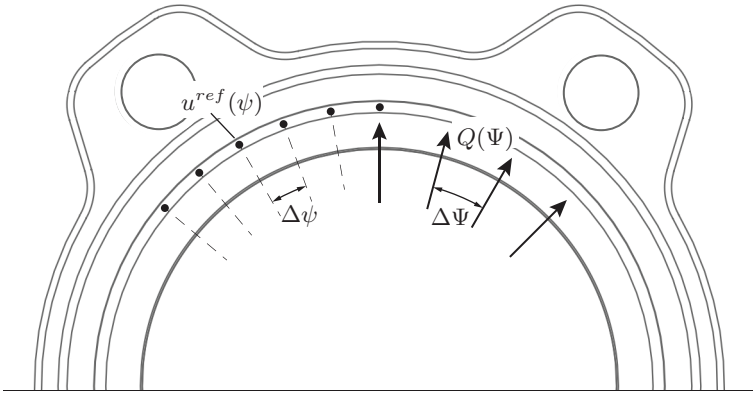

Figure 2.5: Visualisation of deformation $u^{ref}(\Psi)$ interval and point load $Q(\Psi)$ interval

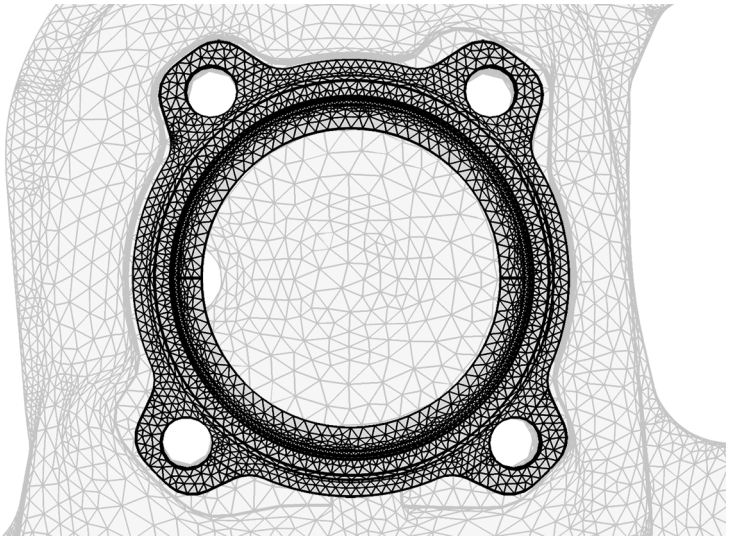

Figure 2.6: Mesh of bearing and knuckle in COMSOL that are used to determine the Fourier coefficients of the compliance function

2.4.2 Reference study setup

As interest lies in the reconstruction of the rolling element load distribution for the purpose of real-time load monitoring it is chosen to use the BEAST software tool as reference. The choice for the BEAST software is related to its ability and efficiency for studying bearing behaviour of running bearings in time domain. This is a result of the detailed and efficient contact analysis and parallelization of contact calculations over multiple processors for reduction of calculation times. Although by default bodies are considered rigid, BEAST allows for flexibility of all components based on a reduced mode shape representation of the deformation.

For a detailed description of how this latter is handled in BEAST the reader is referred to [62]. The BEAST tool has been verified against finite element models and experiments and gives an exact solution for Hertzian contacts [86, 87].

The model implemented in BEAST consists of inner ring, outer ring, 2x15 rolling elements and a separate cage for both inboard and outboard raceway. The outer ring is modelled as a flexible body by a model order reduction of the Finite Element mesh using a free interface method resulting in a total of 270 mode shapes. All other components are modelled as rigid. The inner-ring is rotated with constant speed and is loaded according to the provided input loads. As a rotating bearing is considered a settling period is taken in account for the system to reach steady state after which results are captured.

2.4.3 Single load simulation results

This first set of load cases focuses on pure radial loading. In Figure 2.7 the in- and outboard rolling element loads and operating contact angles for a 5kN radial load case are presented for the proposed-, rigid- and reference BEAST model.

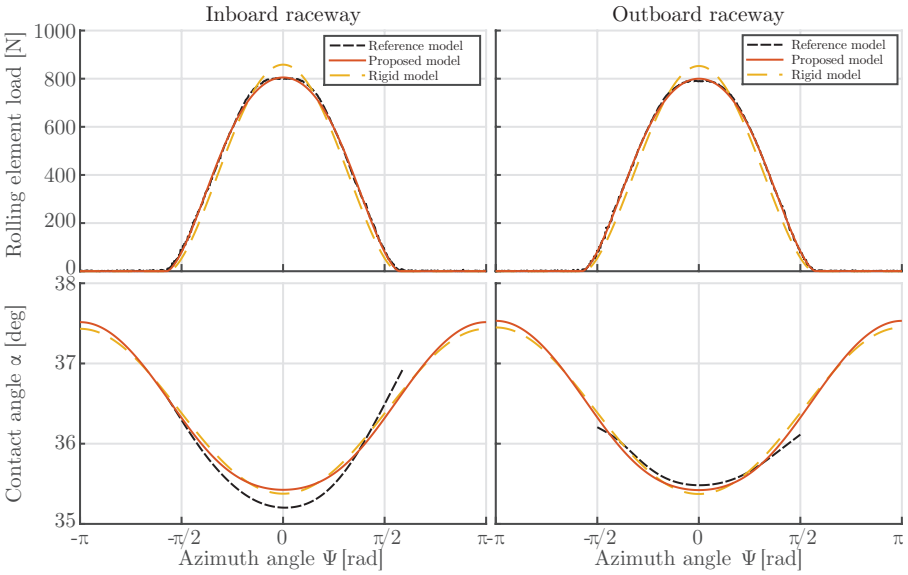

Figure 2.7: In- and outboard rolling element load distribution and corresponding operating contact angles for the BEAST reference, proposed (M=4) and rigid model for an applied radial bearing load of 5 kN

Considering the BEAST reference results, an almost symmetrical response with a peak force of approximately 800N on both in- and outboard raceways can be observed. As the loading is relatively low the operating angles are close to nominal. A small difference between in- and outboard contact angles can be noted which relates to local bending of the outer race. It can be observed that entering ($\psi = -\pi$) and leaving ($\psi = \pi$) the loaded zone takes place at different contact angles.

Comparing the proposed $M = 4$ and rigid model with respect to the reference model it can be observed that the proposed model more accurately describes the rolling element loads. The flexible model peak force at zero azimuth is slightly lower whilst a slight increase of element loading is found at the sides of the bearing ($\psi = -\pi/2$ and $\psi = \pi/2$) with respect to the rigid model. The flexible model behaviour corresponds to the BEAST reference study as it allows for the bearing structure to deform oval as a response to the applied loading. The asymmetry in operating contact angles is not represented by the flexible (and rigid) model as the local effect causing it is not captured by the bulk deformation shapes.

A quantitative insight in the accuracy of the proposed flexible model, including

the effect of the number of deformation shapes, is provided by Table 2.4. The latter presents the rolling element load distribution root-mean-square error (RMSE) values of the rigid and the proposed model ($M = [1, 2, 3, 4, 6, 10]$) with respect to the reference model for four different load cases as indicated in Table 2.3.

Table 2.3: Single load cases

Load case	**Applied load**
	Fx
1	3.0 kN
2	4.0 kN
3	5.0 kN
4	6.0 kN

Table 2.4: RMSE values of the load distribution for four different single load cases

Load case	**Model variant**						
	Rigid	M = 1	M = 2	M = 3	M = 4	M = 6	M = 10
1	15 N	15 N	7 N	5 N	5 N	5 N	5 N
2	22 N	22 N	9 N	5 N	5 N	5 N	5 N
3	30 N	30 N	10 N	6 N	6 N	6 N	6 N
4	38 N	38 N	13 N	8 N	8 N	7 N	7 N

As observed in the qualitative analysis the table shows that the proposed model provides a more accurate description of the rolling element loads than the traditional rigid model. Results indicate that the first deformation shapes corresponding to $M = 1$ have no effect, however a significant accuracy improvement is observed with $M = 2$ and $M = 3$ as RMS errors decrease by an average of 62% and 75% respectively. Further increasing the number of static deformation mode shapes seems not to significantly improve the accuracy any further. A relative improvement of the RMS error between $M = 10$ and rigid model of respectively 68%, 77%, 80% and 80% is found for the 3kN, 4kN, 5kN and 6kN load cases.

2.4.4 Combined loading simulation results

This second set of load cases focuses on combined loading situations. Figure 2.8 presents the rolling element loads and operating contact angles based on the proposed-, rigid- and reference BEAST model for a 5kN radial, 4kN axial and 1.2kNm moment combined load case.

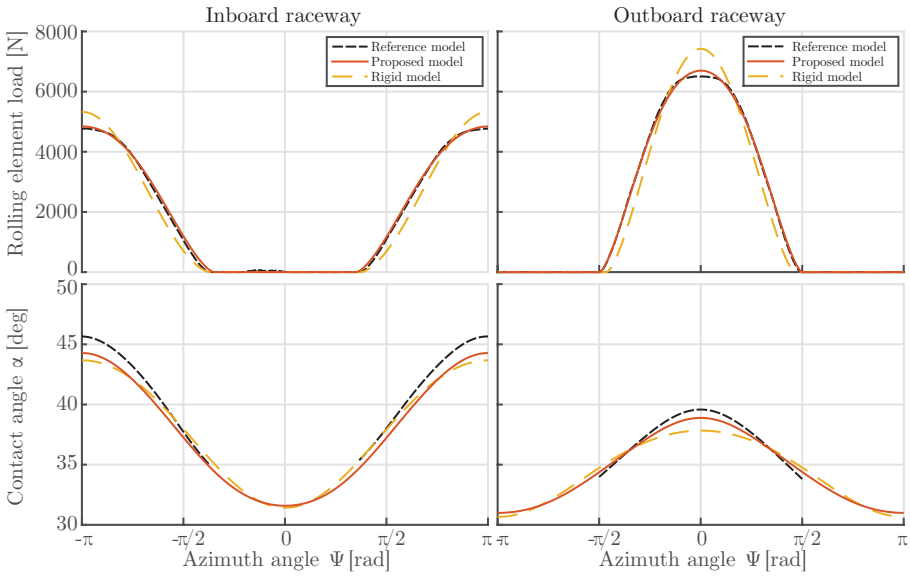

Figure 2.8: In- and outboard rolling element load distribution and corresponding operating angles for the BEAST reference, proposed (M=4) and rigid model for a combined load case

The applied moment results in opposing azimuth positions for the in- and outboard peak loads. As the radial force is applied in positive x-direction the outboard peak load is considerably higher than the inboard peak load. The axial bearing force furthermore causes the inboard load distribution to be significantly wider than the outboard counterpart. Considering the operating contact angles it is observed that the combined load causes significant differences between in- and outboard raceway. Especially the inboard contact angle deviates considerably from the nominal angle.

Comparing the proposed and rigid model with respect to the reference model it can be observed that the proposed model is considerably more accurate. While the rigid model significantly overestimates the peak loads, these are accurately described by the proposed model. Next to that also the load distribution at the sides of the bearing is better represented by the proposed model. In line with the pure radial loading case the improved accuracy by the proposed model is related to the oval deformation of the bearing due to the applied load. For the operating

Table 2.5: Combined load cases

Load case	**Applied load**		
	Fx	Fz	Mx
5	4.9 kN	5.1 kN	1.5 kNm
6	5.0 kN	2.9 kN	0.9 kNm
7	5.0 kN	-2.9 kN	-0.9 kNm
8	4.9 kN	-5.1 kN	-1.5 kNm

Table 2.6: RMSE values of the load distribution for combined loading conditions

Load case	**Model variant**						
	Rigid	M = 1	M = 2	M = 3	M = 4	M = 6	M = 10
5	424 N	424 N	139 N	120 N	98 N	92 N	92 N
6	232 N	232 N	110 N	90 N	77 N	74 N	74 N
7	214 N	214 N	89 N	87 N	72 N	66 N	67 N
8	423 N	423 N	136 N	137 N	111 N	100 N	101 N

contact angles we see a slight improvement using the proposed model although errors up to 1.5deg are observed at the peak loads.

Table 2.6 provides the rolling element load distribution RMSE values for four different combined load cases as indicated in Table 2.5. As in previous Section the rigid- and proposed model results are compared to the BEAST reference model.

In line with the results of the single load test cases it can be observed that increasing the number of deformation shapes improves the accuracy of the rolling element load distribution. Again it is observed that the deformation shapes related to $M = 1$ do not have any effect whilst up to the $M = 6$ model considerable improvements are found. The deformation shapes related to $M = 2$ provide most significant improvement as RMS errors decrease by an average of 62%. The M=10 case shows a slight decrease in accuracy compared to M=6. Comparing the relative RMS error between M=6 and rigid model an improvement of respectively 78%, 68%, 69% and 76% is found for the 1.5kNm, 0.9kNm, -0.9kNm and -1.5kNm cases.

2.4.5 Discussion

The presented load cases show that the proposed model provides a more accurate rolling element load distribution than the traditional rigid model for the analysed bearing as an improvement of up to 80% can be achieved depending on the amount of deformation shapes considered. For both load cases it is found that heavier load conditions result in more improvement in both absolute as relative sense. This can be explained as these test cases result in more deformed structures, and thus considering deformation effects is more advantageous. Furthermore it is noted that only a limited improvement on the estimated contact angles is achieved. The latter is related to the consideration of a single deformation shape for both raceways, as well as due to the assumption of radial deformation only. The noted error on the contact angle however is limited and therefore acceptable.

Regarding to the effect of the number of deformation shapes it is clearly observed that the deformation shapes corresponding to $M = 1$ are insignificant and thus do not reflect any occurring real deformation. The deformation shapes corresponding to $M = 2$ result in most significant improvement of approximately 62% whilst a slight accuracy gain to about 80% is observed until $M = 4$ for the single load cases and $M = 6$ for the combined load cases. Most probably this pattern is representative for most cases, as in general the first mode shapes take in account for the bulk of deformation. However this depends on the geometry and boundary conditions of the structure. The results furthermore show that in more complex loading combinations it is advantageous to take in account more deformation shapes. The absolute improvement is case dependent as geometry, mechanical properties, boundary conditions and loading affect the results.

With respect to the BEAST benchmark simulation it is observed that a highly accurate representation of the rolling element load distribution is obtained for a fraction of its computational costs. For the complex combined load cases RMS Errors are as low as 100 N whilst a peak load of over 6 kN characterizes the load distribution. No extensive study is performed to assess the computational gain, as the differences are considerable: where the BEAST simulations generally took up several hours on multiple computational cores, the proposed algorithm solves in a fraction of a second. The latter is paramount for the inclusion in the real-time load reconstruction algorithm presented in Chapter 4.

2.5 Load distribution behaviour

By the use of the validated semi-analytical bearing model the rolling element load behaviour as a function of bearing loading can be addressed. In particular, it is interesting to analyse the rolling element loading at various bearing azimuth angles for different load cases in order to assess the complexity or non-linearity of this relationship. Although an in-depth analysis of this behaviour is not within the scope of this thesis a basic analysis for two combined load cases is provided for discussion.

Table 2.7: Two combined load cases

Load case	**Applied load**		
	Fx	Fy	Mx
9	5.0 kN	4.0 kN	1.50 kNm
10	5.0 kN	4.0 kN	-0.75 kNm

Figure 2.9 presents the load distributions for the combined load cases 9 and 10, summarized in Table 2.7, for the bearing considered in this Chapter. Both load cases consider identical radial loads whilst the applied moment over the x-axis is varied. It is well observed that the load distributions of case 9 and 10 are completely different as a result of the change of the applied moment. Due to this non-linear behaviour, reconstruction of any of the (radial) loads requires the consideration of the other loaded degrees of freedom.

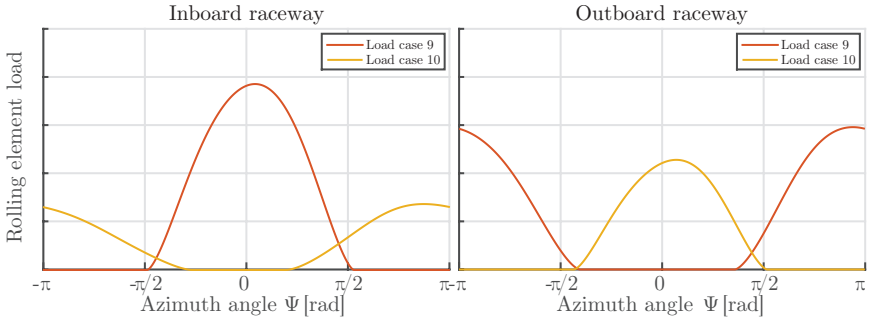

Figure 2.9: Any individual load can be represented by various load distributions depending on the combined bearing loading

2.6 Conclusion

For the purpose of model based bearing load reconstruction a computationally low-cost and accurate description of the relationship between bearing and rolling element loading is paramount. This Chapter addresses this topic by the introduction of a semi-analytical bearing model that includes flexibility of the bearing outer-ring structure. By combining static deformation shapes and a Fourier series based compliance approximation, which is tuned by a Finite Element Study on the bearing structure, an accurate description of the deformation of the raceway structure is obtained. A comparison study to a well-established bearing simulation tool shows that the model provides an accurate description of the rolling element loading for various load cases. Furthermore, the proposed model outperforms traditional rigid bearing models in case of a (common) flexible outer-ring structure. The achieved improvement depends on the number of static deformation shapes considered. For the case study it is found that the first set of relevant deformation shapes results in an average decrease of rolling element load distribution RMS errors of 62%, whilst an improvement of up to 80% can be obtained when a higher number of shapes is taken in account. In contradiction to other bearing models considering raceway flexibility the proposed model is of low computational costs due to its semi-analytical description and provides no limitations on the structure's geometry.

Chapter 3

Novel Bearing Strain Model

The second stage of the proposed physics-based approach considers the relationship between rolling element loading and bearing outer-ring strain. Due to the industrial secrecy regarding the developments of bearing load measurement and the application of black box data-driven methods, only limited literature is available on this topic. In this Chapter, therefore, a quantitative description of bearing outer-ring strain is presented, based on simulation and experimental studies performed for this thesis. Additionally, a local strain model is presented that parameterizes the relationship between local rolling element loading and local outer-ring surface strain. The latter model forms the basis for the model-based strain conditioning proposed in Chapter 4.

S. Kerst, B. Shyrokau and E. Holweg. "A model-based approach for the estimation of bearing forces and moments using outer-ring deformation", *Transactions on Industrial Electronics (2019): 10.1109/TIE.2019.2897510*. [46]

S. Kerst, B. Shyrokau and E. Holweg. "Wheel force measurement for vehicle dynamics control using an intelligent bearing", In *Advanced Vehicle Control* pages 547-552 (2016). [44]

3.1 Introduction

Literature on the topic of bearing load measurement, and in particular on strain behaviour and conditioning is limited. The work by NTN in [67] provides the best insight on the state-of-the-art in strain behaviour for bearing load reconstruction. As discussed in the introduction of this thesis (Figure 1.5) this technical review considers two important strain components: *"a strain component due to the external force"* and *"strain owing to the rolling motion of rolling elements"*. Although from a physics perspective this description is not fully correct, it does reflect the two important aspects related to bearing outer-ring strain: a contribution that can be directly related to the bearing loading and an effect due to the changing rolling element arrangement.

As both strain components defined in [67] are affected by the bearing load, both effects can be considered for bearing load reconstruction. This is reflected by research on load estimation by our industrial partner SKF, which has developed Generation 1 and Generation 2 load sensing, applying both effects as visualized by Figure 3.1. Results of these developments at SKF have not been published due to industrial privacy reasons and therefore only limited details like patent applications [58, 59] and product presentations [85] are available.

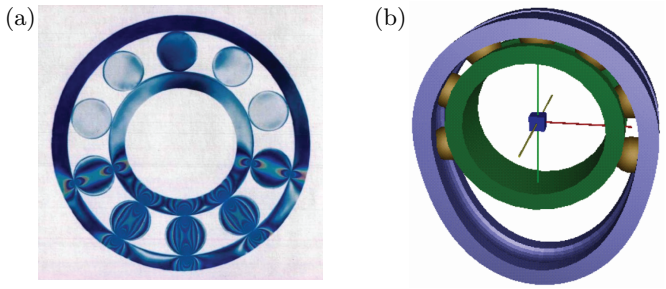

Figure 3.1: SKF generation 1 & 2 load estimation: (a) reflects the contact stresses and strains by rolling elements whereas (b) presents the global deformation due to loading (out of scale representation)

Generation 1 (GEN1) load sensing focuses on the varying local contact strain due to rolling of the rolling elements and is implemented using either a peak-to-peak detection algorithm or a signal power analysis conditioning approach. It is the oldest method and it has been applied for testing in industrial machinery with single row bearings for estimation of 1 and 2 DoFs load cases with success. It is invariant to thermal effects but due to its basic signal conditioning provides a limited bandwidth, is prone to measurement noise and cannot be applied for complex load cases or double row bearings.

The second generation load sensing (GEN2), introduced in 2000, is based on the outer-raceway global deformation as a direct consequence of the external force.

It applies low-pass filtering of the strain measurement to determine deformation mode shapes. It was introduced to cope with double row bearings and provides an increased bandwidth with respect to the GEN1 approach. However, considerable complexities are noted due to thermal drift and the influence of boundary conditions.

Although developed for double row bearings, thermal drift and non-linear behaviour with respect to bearing loading limits the applicability of the GEN2 method for such setups. As the GEN1 basic signal conditioning approaches at the same time have shown to be inapplicable, currently no approach is viable for load reconstruction on widely applied (automotive common) double-row bearings. Additionally, both methods are affected by rotation of the bearing, and cannot be applied at standstill.

In order to cope with standstill situations, NTN has developed a specific sensor design for bearing load reconstruction. As indicated in Figure 3.2 (a) this sensor consists of two strain gauges separated by a distance of 1/2 ball pitch. This leads to direct measurement of the *external force* dependent strain (Figure 3.2) without the need of additional signal processing. It however does not avoid issues related to thermal drift. Both SKF and NTN apply a black box data-driven post-processing for reconstruction of the bearing loading.

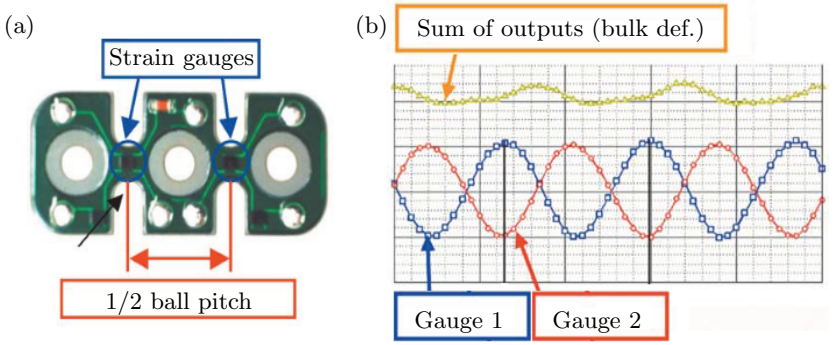

Figure 3.2: NTN sensor arrangement for direct measurement of the bulk deformation [67]

The previously presented strain description and conditioning methods are the only available descriptions on this topic in literature to this day. As industry is not eager to share these details, this Chapter provides a qualitative description of two outer-ring strain effects. Additionally a model is presented for description of bearing local strain for the application in model based bearing load reconstruction. This model allows for determination of rolling element loads based on outer-ring strain, and combined with the model presented in Chapter 2 allows for model based load reconstruction. The strain description is developed based on experimental and simulation studies during the research. Explicit validation of this model by the

use of a simulation study is considered to be outside of the scope of this thesis, however an implicit validation is provided by the experimental study in Chapter 6.

3.1.1 Coordinate systems

In this chapter two coordinate systems are applied. The first is a cylindrical bearing coordinate system to define strain measurement and rolling element locations. Figure 3.3 (a) shows this coordinate system, that defines the bearing azimuth angle ψ with range $[-\pi < \psi \leq \pi]$.

The second coordinate system is a local coordinate system for each defined strain measurement location. Assuming equal separation between rolling elements, the system is rotation symmetric and it suffices to only define the location of the closest rolling element for any strain measurement location as explained in Figure 3.3 (b). The local rolling element phase φ is defined in a range of $[-\pi < \varphi \leq \pi]$.

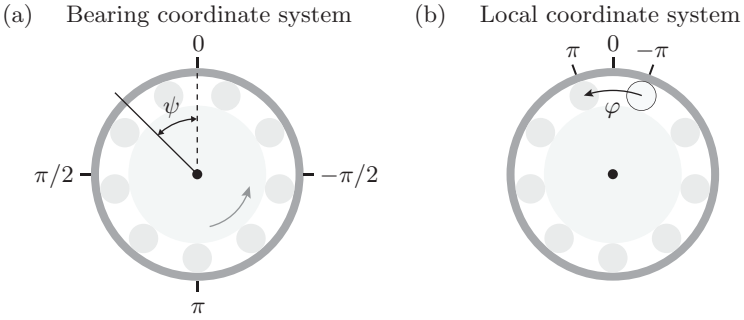

Figure 3.3: Coordinate systems used in this Chapter

3.2 Outer-ring deformation

The outer-ring deformation considers two distinct strain components. This is a consequence of the bearing specific behaviour of reallocation of rolling elements that leads to a continuously changing internal load path. For a running bearing the deformation therefore varies even if the loading is constant.

The outer-ring strain at any azimuth angle ψ is the superposition of the strain due to loading of each individual rolling element. The strain contribution of each element depends on its loading and sensitivity. The rolling element loading acts as a scalar and its distribution is discussed and modelled in Chapter 2. The sensitivity is the transfer function of rolling element load to strain and depends on the rolling element azimuth ψ, strain measurement azimuth ψ and the (case specific) mechanical characteristics of the bearing. An example of the rolling element sensitivity for a measurement location on the bearing considered in this study is provided in Figure 3.4. This Figure is generated by the use of a simulation

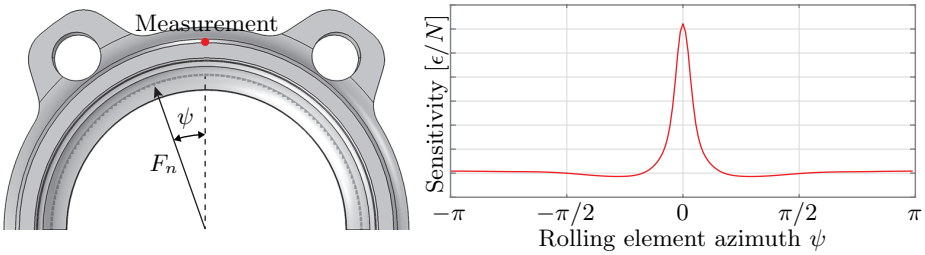

Figure 3.4: The transfer function of rolling element load to outer-ring strain at any measurement azimuth ψ is a function of the rolling element azimuth ψ

study on the bearing outer-ring by applying rolling element loads at various bearing azimuth angles and evaluating its effect at the specific measurement location. For the latter, the Finite Element model of Chapter 2 is used.

If equal element spacing is considered due to usage of a cage, a cyclic behaviour with a frequency equal to the ball-pass frequency results which can be described in the local coordinate system of the strain measurement location. For a constant loading the outer-ring strain variance is a consequence of the change of sensitivity of each rolling element. Due to the peak sensitivity and gradients near the measurement location, well observed in Figure 3.4, loaded rolling elements in this area provide the main contribution to the strain variance. The strain variance therefore provides a measure for the local rolling element loading.

The strain at any measurement azimuth ψ can be split in a constant and varying component. The constant part is affected by all rolling elements and is defined as the bulk deformation. The varying part is most predominantly affected by local rolling element loading and is referred to as local deformation. As indicated in Figure 3.5 the outer-ring deformation is considered as the sum of bulk and local effects.

The following definitions are considered for bulk and local deformation and strain:

- The *bulk* effect is the average deformation over a full ball-pass period for any applied bearing loading. It is a result of all loaded rolling elements and the constant component of their respective sensitivities.

- The *local* effect is the variance of deformation as a result of the changing arrangement of loaded local rolling elements. It is a result of the change of sensitivities of rolling elements dependent on their location.

As both bulk and local strain are load dependent, either components can be considered for bearing load reconstruction. However, as both effects have a different origin their properties with respect to load estimation differ. In the following the bulk and local deformation effects are described more thoroughly.

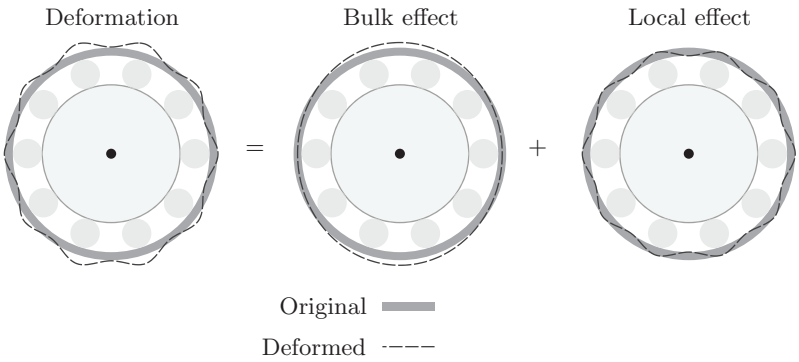

Figure 3.5: The bearing outer-ring deformation is defined by bulk and local effects (out of scale representation)

3.2.1 Bulk deformation

The bulk deformation is the average strain during a full rolling element passage for any loading. It considers the sum of all rolling element loads multiplied by their average sensitivity. As in described in [67], it is considered to be the direct consequence of the applied bearing loading as it reflects the DC-component or average of the outer-ring load induced strain.

Most considerable challenge in usage of the bulk deformation for load reconstruction relates to the measurement of the signal itself. As it considers the DC part of the strain it is biased by other low-frequency contributions as thermal effects and boundary conditions. As these disturbances are considerable, they need to be attributed for accurate measurement of the (load dependent) bulk deformation.

Internal bearing friction and external thermal influences as air flow and brake application (for wheel-end applications) can lead to considerable variance in bearing temperature and consequent thermal deformation. Experimental studies have shown that the thermal deformation is in a similar order of magnitude as the bulk deformation measure. It will thus significantly bias the strain measurement and a method to correct for this offset is therefore paramount. For this purpose, in [18] a thermal model and thermal state estimator are developed. Although in controlled conditions reasonable results could be achieved, difficulties in estimating heat flux and thermal gradients within the bearing make the approach unsuccessful for correction of the thermal deformation bias in operating conditions.

Next to the thermal bias, the boundary conditions enforced by the support structure lead to difficulties in usage of the bulk deformation for load reconstruction. The bulk behaviour is highly case-specific as besides the bearing characteristics the support structure's geometry, material properties and conditions due to mounting have shown to affect its behaviour considerably [37]. As the boundary conditions differ depending on the setup and its effect is often considerable, bulk behaviour can vary significantly and is hard to generalize. It is for these reasons

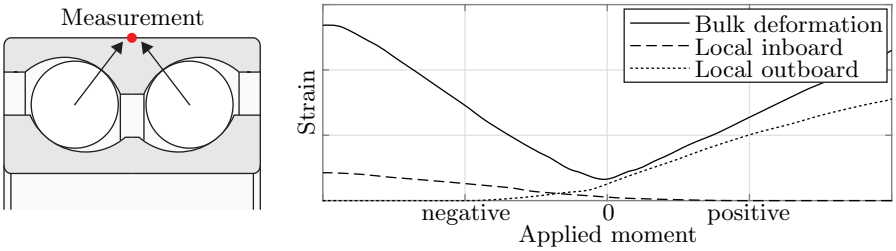

Figure 3.6: Estimated bulk and local strain while applying a varying moment. The Figure is created using the proposed algorithms of this thesis and shows that local strain considers in- and outboard contributions whereas the bulk deformation provides a single measure

that simulation studies on bulk behaviour show considerable errors with respect to experimental results and data driven methods using in-situ calibration are applied in the state-of-the-art.

Additionally, an important limitation of bulk deformation measurement on double row bearings is related to lumping of in- and outboard strain. Due to the latter, any individual bulk strain measurement does not discriminate in- and outboard loading. The latter can be observed in Figure 3.6, that shows conditioned bulk and local strain during one of the experiments performed during this thesis. As the super-positioned bulk effects cannot be split, it adds to the non-linearity of bulk deformation to bearing loading.

3.2.2 Local deformation

The local deformation considers the strain variance due to rearrangement of rolling elements and is a result of the azimuth dependent sensitivity and loading of rolling elements. This periodic signal, the AC-component or variance of the outer-ring strain, has a fundamental frequency equal to the ball-pass frequency f_{bp}. As it reflects the AC component of the signal, the local strain is not affected by low frequency effects as thermal deformation. As the strain variance is caused by the change of sensitivity over the bearing azimuth, and as the change of sensitivity is most significant for rolling elements near the measurement location, the local deformation provides a measure for local rolling element loading.

An important aspect of local deformation is the spread of the sensitivity or transfer function peak as it defines the contribution of each of the local elements. The shape and spread of the sensitivity function depends on bearing and housing geometry and aspects as material properties, interfaces and mounting methods. In case of a narrow peak, for instance due to a thin outer-ring structure, the local strain will be closely related to only the closest rolling element. A wider shape on the other hand results in influence by multiple local rolling elements. However, if a fixed load distribution with varying magnitude is assumed, the local deformation

can be regarded as a linear measure of the most local rolling element load.

Strain measurement properties, local geometry and mechanical properties define the shape of the sensitivity peak of Figure 3.4. It consequently defines the shape and sensitivity of the cyclic strain due to passing of local loaded rolling elements. When symmetry is assumed in both geometry and local load distribution, a strain peak and valley are observed when the local rolling element respectively is in line ($\varphi = 0$) and at a midpoint ($\varphi = \pi$) as depicted in Figure 3.7.

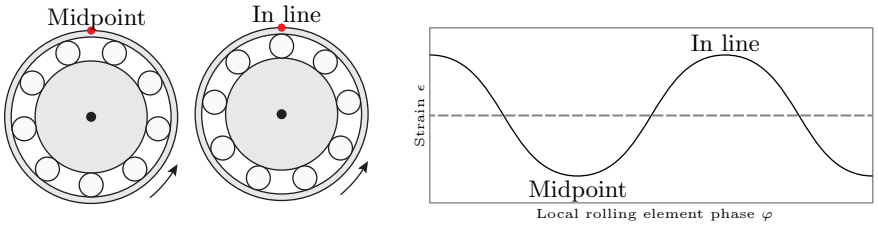

Figure 3.7: Local strain resulting due to reallocation of rolling elements

If either the load distribution or local geometry are not symmetric, the cyclic shape will become skewed with respect to the presented symmetric case. Non-symmetric local geometries are not considered in this study as it is hard to address and could be avoided by appropriate placement of measurement points. Non-symmetric load distributions cannot be avoided but its effect is neglected as it mainly affects the harmonics of the cyclic strain. It is neglected as it considerably simplifies the strain description and leads to only a limited decrease in accuracy.

Besides the dependency on local element phase φ, the sensitivity of the local strain to local rolling element load is related to the rolling element contact angle or load line as well as axial location of the strain measurement location. Its exact behaviour with respect to these effects has been analysed in simulation, but as it is heavily affected by geometry no global description of its shape and magnitude can be defined. Nevertheless, one can assume that the sensitivity with respect to the contact angle can be described by a polynomial with a shape similar to Figure 3.8. In the case of a double row bearing with little axial spacing between

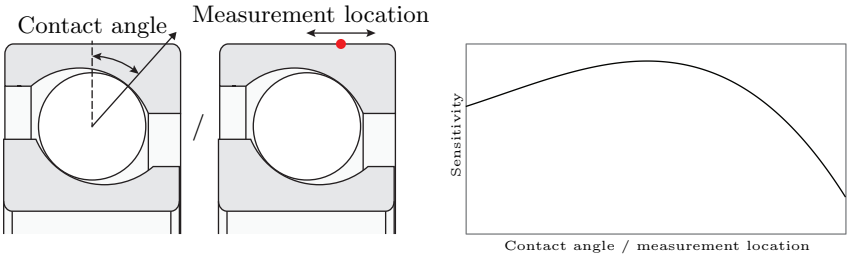

Figure 3.8: Effect of measurement point location and contact angle

both raceways any axially centred measurement location will capture a lumped measurement of both local in- and outboard strain effects. Assuming linear elastic mechanical behaviour the superposition principle holds and hence the measured local strain is the sum of in- and outboard local effects as depicted in Figure 3.9.

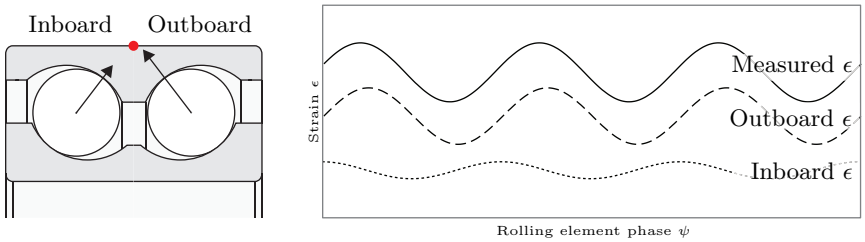

Figure 3.9: Superposition of in- and outboard effects

The axial location of the strain gauge and difference of in- and outboard local geometry will affect the sensitivity of the measurement location to both in- and outboard local rolling element loading. The difference of local strain shape that results due to this allows for discrimination of in- and outboard loading.

3.2.3 Bulk and local deformation in frequency domain

As any strain measurement on the bearing outer-ring surface captures both bulk and local deformation, pre-conditioning is necessary to extract either bulk (DC component) or local (AC component) effects. As the bulk deformation can be considered as a direct effect of the bearing loading, its bandwidth equals the load bandwidth. The local deformation on the other hand is a harmonic signal itself and its related frequencies equal the ball pass frequency f_{bp} and its harmonics.

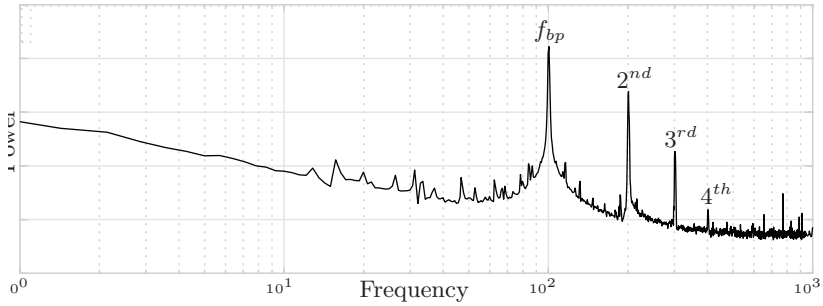

Figure 3.10: A FFT of strain gauge data of an experiment performed during this thesis. The local strain can be clearly identified as several peaks in the frequency domain

Separation of both effects can be achieved by signal conditioning when ball pass frequency f_{bp} exceeds the bandwidth of the external loading. In that case, low-

pass filtering or multiple notch-filters on ball-pass frequency f_{bp} and its harmonics can be applied to extract the bulk deformation. The local strain can be obtained by a band-pass filter over ball pass frequency f_{bp} and its harmonics.

Figure 3.10 shows a FFT of raw strain gauge data of an experiment performed during this thesis. The frequency domain plot clearly shows the local effect in the form of peaks at ball pass frequency f_{bp} and its harmonics. The ball pass frequency during this experiment was approximately 100 Hz.

With respect to the strain gauge design of NTN, it can be understood that by placement of two strain gauges at a half-ball pitch interval a 180 degree phase difference at the ball-pass frequency results. Summation of these signals then leads to attenuation of the peaks at f_{bp} and its n harmonics at 2^n. It thus does not lead to full attenuation of the local effect as it does not consider the 3^{rd} harmonic, which is well observed in example of NTN in Figure 3.2.

3.3 Local strain model

Based on the phenomena discussed in Section 3.2 the following local strain approximation model is proposed for any measurement location on the outer-ring of a single raceway bearing:

$$\varepsilon_l(\psi) = Q(\psi)G(\varphi)\eta(\alpha) \tag{3.1}$$

where ε_l is the outer-ring local strain variation at azimuth ψ, Q is the rolling element force at azimuth angle ψ, G is a normalized periodic transfer function dependent on the local rolling element phase φ and η represents the measurement location sensitivity as function of contact angle α.

The periodic transfer function captures the effect of the changing load paths on the outer-ring local deformation. Assuming a constant rolling element force during the ball-passing period, the local strain variation can be fully addressed to the periodic transfer function. The following representation for the *periodic transfer function* is proposed:

$$G(\varphi) = \sum_{n=1}^{N_h} a_n \cos(\varphi n + \phi_n) \tag{3.2}$$

where a_n and ϕ_n represent the magnitude and relative phase shifts of each of the n harmonics and N_h defines the number of harmonics considered. The local rolling element phase φ is periodic with $-\pi \leq \varphi < \pi$ and equals 0 when an element is in line. Function normalization is achieved by setting the first harmonics' magnitude a_1 to unity and phase ϕ_1 to zero.

Due to normalization of the periodic function the element load to strain magnitude is solely reflected by the measurement location sensitivity. For the sensitivity, which is a function of contact angle α, the following polynomial description for the *sensitivity function* is proposed:

$$\eta(\alpha) = \sum_{n=0}^{N_p} c_n \alpha^n \tag{3.3}$$

where c_n are the polynomial coefficients and N_p is the order of the polynomial.

In case a double row bearing is considered (3.1) can be extended according to the superposition principle as linear elastic deformation is considered. The modelling equations for a *double row bearing* therefore become:

$$\varepsilon_l(\psi_i, \psi_o) = Q_i(\psi_i) G_i(\varphi_i) \eta_i(\alpha_i) + Q_o(\psi_o) G_o(\varphi_o) \eta_o(\alpha_o) \tag{3.4}$$

where the i and o subscripts refer to the inboard and outboard effects and functions respectively.

3.4 Conclusion

This chapter discusses the separation of bearing outer-ring deformation and strain in bulk and local effects. The different effects are a consequence of the bearing specific behaviour of reallocation of rolling elements that leads to a continuously varying internal load path. The root cause of the different effects is shown to be related to the phase variant strain-to-load transfer function or sensitivity. Where the bulk deformation is a consequence of the average sensitivity over rotation the local deformation is related to the change of sensitivity. As the change of sensitivity is furthermore most significant close to the measurement location, the local effect is reflective of the local loading. The bulk effect on the other hand is affected by all rolling element loads.

For the development of a model based local strain conditioning approach a novel strain model is presented in this Chapter. This model provides a physical description of bearing outer-ring strain as a function of local rolling element loading. The model considers the strain amplitude to be directly related to local rolling element loading and includes all important aspects involving the local strain: (i) it contains a periodic transfer function to model the movement of rolling elements and (ii) a contact angle dependent function to describe the measurement sensitivity. A possible extension for double row bearings is provided based on the principle of superposition. By combining the strain model with the previously introduced load model, a deterministic relationship between bearing loading and outer-ring strain can be established.

No explicit validation of the model is provided as this is considered to be outside of the scope of this thesis. However, an implicit validation is provided by the implementation of the model in a Kalman Filter based conditioning approach, presented in Chapter 4, and experimental validation study in Chapter 6. The latter additionally shows that the model is applicable for discrimination of in- and outboard strain effects.

Chapter 4

Kalman Filter Based Load Reconstruction Algorithm

Based on the load and strain models presented in previous Chapters, a physics-based bearing load reconstruction algorithm is developed. As the load and strain model cannot be assessed individually with the experimental setup, three algorithms with increasing usage of physical modelling are developed for the proper assessment of their effectiveness and accuracy. The first and rather basic approach was developed as a proof of concept and considers a data-driven state-of-the-art method. Subsequently, the second algorithm considers the inclusion of a model-based conditioning approach by using the strain model introduced in Chapter 3. Finally, a full model-based approach including the load model from Chapter 2 is proposed. For the sake of readability of this thesis, this Chapter only presents the description of the three algorithms, whereas the validation and comparison studies are provided in Chapter 6.

This Chapter combines results published in:

S. Kerst, B. Shyrokau and E. Holweg. "A model-based approach for the estimation of bearing forces and moments using outer-ring deformation", *Transactions on Industrial Electronics (2019): 10.1109/TIE.2019.2897510*. [46]

S. Kerst, B. Shyrokau and E. Holweg. "Reconstruction of wheel forces using an intelligent bearing", *SAE International Journal of Passenger Cars-Electronic and Electrical Systems 9.2016-01-0092 (2016): 196-203*. [43]

4.1 Introduction

This Chapter considers the algorithm development for model based bearing load reconstruction. Figure 4.1 provides an overview of the proposed load reconstruction methodology, which includes an instrumented bearing equipped with N_{sg} strain measurements and processing by a load reconstruction algorithm to determine the bearing load estimate. The reconstruction algorithm consists of two processing steps of which the first considers the signal conditioning of the raw strain measurements whereas the second comprises the bearing load calculation. As signal conditioning for the purpose of load reconstruction is discussed in Chapter 3, only a limited recap of relevant aspects for the considered wheel-end bearing is provided in this introduction. Additionally the state-of-the-art on load calculation is discussed, and its considerations for this thesis are provided. Finally the introduction provides an overview of the developed algorithms and their applicability.

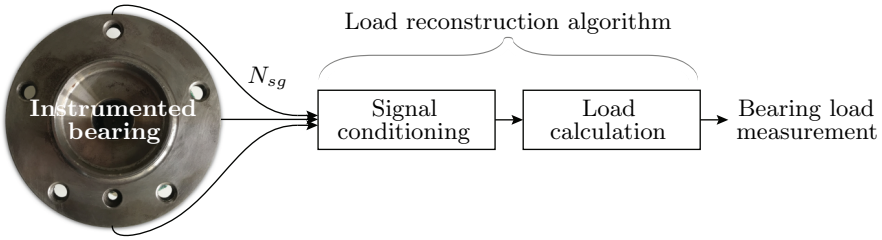

Figure 4.1: Basic stages of load reconstruction

4.1.1 Signal conditioning

The first stage of any load reconstruction algorithm concerns the conditioning of the raw strain measurement. As this measurement consists of two distinct load indicative strain components, bulk and local strain, considerations on signal conditioning do not only regard the method to apply, but also the signal content to focus on. The latter is of particular importance as both components' properties differ considerably. As this thesis focuses on wheel-end bearings, the limited axial raceway distance that leads to lumping of strain contributions is taken into consideration for development of the load reconstruction algorithm.

Figure 4.2 (a) shows a Hub Bearing Unit wheel-end bearing that can be considered for development of the load reconstruction approach. Additionally, Figure 4.2 (b) shows an example of the in- and outboard strain (ϵ), indicated by respectively blue and yellow, that would result by loading of the respective raceways at any particular bearing azimuth angle. Any strain measurement however will only observe the superposition of both effects as indicated by red due to the limited axial distance between both raceways. As a consequence of this superposition or lumping effect, state-of-the-art conditioning methods have limited applicability

for the considered setup. For any bulk deformation based approach it will lead to an increased non-linearity with respect to the bearing loading. Application of peak-to-peak measurement of AC power analysis on the other hand becomes non-conclusive due to asynchronicity of both raceways which leads to alternating constructive and destructive interference often referred to as the beating effect.

These various challenges limit state-of-the-art conditioning approaches for the purpose at hand. This thesis therefore proposes the development of a model based local strain conditioning methodology. By focussing on local strain, thermal issues related to the bulk deformation are avoided. Furthermore, the proposed approach implements continuous tracking of the local strain by the proposed strain model which results in the decomposition of the in- and outboard strain contributions of the superpositioned local strain measurement.

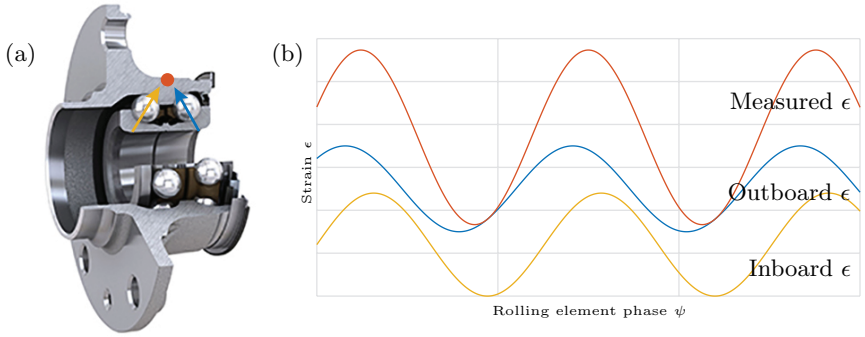

Figure 4.2: Wheel-end bearing strain superposition due to small axial distance between in- and outboard raceway

4.1.2 Load calculation

After conditioning of the raw strain, the bearing loading is reconstructed in the load calculation stage. State-of-the-art load calculation applies data-driven methods as neural networking or fitting based approaches for reconstruction of the bearing loading. These methods are however limited for commercial application because of the non-linear relationship between bearing loading and outer-ring strain as noted in Chapter 2. More specifically, due to the high non-linear bearing behaviour any empirical method requires a large number of parameters (subject to calibration) for decent reconstruction of the bearing loading.

For example, the approach presented in Figure 4.3, presented in [67], considers a database of different strain-load coefficients to cope with the non-linearity between different operating regions of the bearing. Although this may lead to decent estimates of the three force vectors F_x, F_y and F_z, it necessitates the introduction of a selection procedure as well a large database of strain-load coefficients. The latter limits its feasibility as it will require extensive calibration for each bearing

to cope with production tolerances.

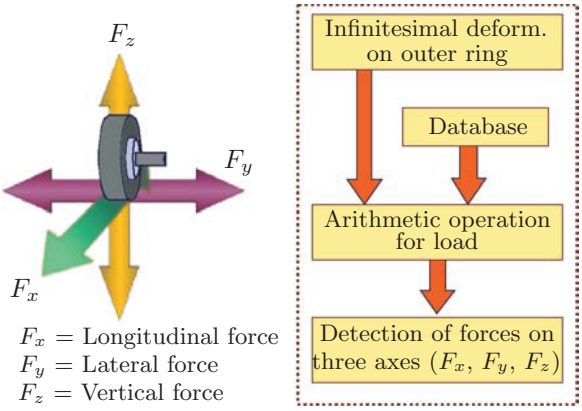

Figure 4.3: Data driven load reconstruction approach presented in [67]

An empirical approach to the load calculation stage thus requires either an extensive neural network, higher order fitting or piecewise linearization to capture the non-linear behaviour of the bearing. This consequently leads to a large number of parameters subject to calibration which on its turn is not feasible for commercial or industrial application. This thesis therefore focuses on a fundamentally different model based approach to capture the non-linear behaviour more effectively and thereby limit calibration effort.

4.1.3 Algorithm development

For the sake of analysis of bearing behaviour and the application of model based load reconstruction this thesis considers the development of three different load reconstruction algorithms.

1. The first algorithm is based on the state-of-the-art and therefore implements a *bulk deformation data-driven approach*. It serves as the baseline reference with respect to estimation quality and evaluates the usage of bulk deformation and coefficient fitting for load estimation.

2. The second algorithm involves a model based approach for conditioning of the local strain effect. In line with the first algorithm, it applies a data-driven coefficient based load calculation step and is referred to as the *local strain data-driven approach*. It allows for the assessment of the model based strain conditioning method by comparison to the bulk deformation based approach.

3. The third algorithm considers a model based approach for both conditioning of local strain and load calculation. It is the final developed algorithm in

this thesis and is referred to as the *local strain model based approach*. Due to the inclusion of modelling in load reconstruction the chance of over-fitting is reduced and calibration effort is limited with respect to the data-driven approaches.

A step-wise approach towards a full model based algorithm is taken within the algorithm development study. This stepwise approach allows for a more effective analysis and validation of the model based conditioning and load calculation approaches. In particular, as it allows for an extensive comparison study. In the following the description, tuning and calibration methods for each of the three algorithms is presented. An extensive analysis and experimental validation of the proposed algorithms is finally performed in Chapter 6.

4.2 Bulk deformation data-driven approach

The proposed *bulk deformation data-driven approach* is inspired by the state-of-the-art and was developed for the proof of concept study on the anti-lock braking application presented in Chapter 7. Additionally, now it serves as the state-of-the-art reference and allows for evaluation of the applicability of bulk deformation and coefficient fitting for load estimation.

The approach is founded on a cascade of basic data processing steps for signal conditioning to extract the outer-ring bulk deformation. Additionally, it includes a thermal compensation method to minimize the effect of thermal drift. The bearing loading is finally calculated by the use of a coefficient matrix. An overview of the algorithm, which is more thoroughly explained in the following subsections, is provided in Figure 4.4.

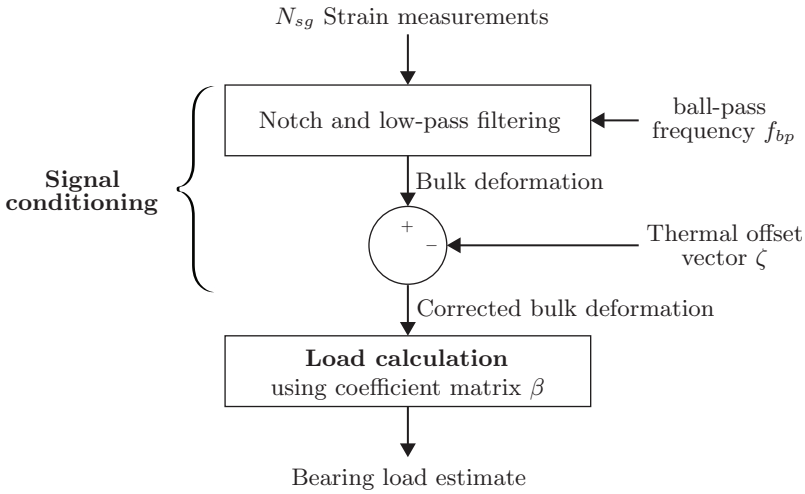

Figure 4.4: Overview of the bulk deformation data-driven approach

4.2.1 Signal conditioning

The signal conditioning considers independent filtering of each of the N_{sg} raw strain measurements to determine the outer-ring bulk deformation at each measurement location. The bulk deformation is determined by the use of multiple N_{notch} notch filters for attenuation of the local strain. Additionally, a low-pass filter is applied for noise suppression of frequencies outside the band of interest. Finally, a thermal correction is applied to attenuate the thermal effects on the bulk deformation measure.

In the first conditioning stage multiple 2^{nd} order IIR notch filters are applied. The first notch filter frequency, or fundamental frequency, equals the (variant) ball-pass frequency f_{bp}. The number of necessary or relevant notch filters depends on

the number of significant harmonics and is case dependent. By appropriate tuning of the Q-factor, the local strain can be fully attenuated. For proper functioning of the algorithm, the ball-pass frequency f_{bp} is required as external input.

In addition to the notch filters, a 2^{nd} order Butterworth low-pass filter is applied to suppress noise above the bandwidth of interest. The filter cut-off frequency f_c of this low-pass filter is case specific, and can be defined by analysis of raw measurements.

As the obtained bulk deformation is a measure of both load and thermal induced deformation, a correction is applied for attenuation of the latter:

$$\hat{\varepsilon}_{b,n} = \varepsilon_{b,n} - \zeta_n \tag{4.1}$$

where ζ is an estimate of the thermal induced strain, $\hat{\varepsilon}$ is the resultant load dependent bulk deformation and the n subscript refers to the n^{th} measurement within $n = 1..N_{sg}$. The method to determine ζ is discussed in calibration Subsection 4.2.4.

Although measurement of the thermal induced strain is not feasible for real-life applications, it serves well for research purposes to examine the applicability of bulk deformation for load reconstruction. Note that, depending on the significance of heat flux, the compensation will become inaccurate. However, it does provide a temporary and effective suppression of thermal strain. Additionally, it allows for observation of the degenerative effect over time of the thermal induced error.

4.2.2 Load calculation

After determining the load dependent bulk deformation for each strain gauge, all conditioned measurements are combined to deformation vector $\boldsymbol{x}_r$ that includes first and second order terms:

$$\boldsymbol{x}_r = \begin{bmatrix} \hat{\varepsilon}_{b,1} & \dots & \hat{\varepsilon}_{b,N_{sg}} & \hat{\varepsilon}^2_{b,1} & \dots & \hat{\varepsilon}^2_{b,N_{sg}} \end{bmatrix} \tag{4.2}$$

Based on the deformation vector, the bearing loading is reconstructed using a coefficient based approach in line with [67]. The load calculation is described by:

$$\boldsymbol{y}_r = \boldsymbol{x}_r \boldsymbol{\beta}_r + \boldsymbol{v}_r \tag{4.3}$$

where $\boldsymbol{y}_r$ is the vector of bearing load estimates, $\boldsymbol{x}_r$ is the deformation vector, $\boldsymbol{\beta}_r$ is the coefficient matrix and $\boldsymbol{v}_r$ is the noise term.

4.2.3 Tuning

As the algorithm is set-up using basic filtering components, only the filter frequencies and notch Q-factor need to be defined. These values are case dependent, and

can be best determined using an FFT on raw measurements of the instrumented bearing.

4.2.4 Calibration

Calibration of coefficient matrix $\boldsymbol{\beta}_r$ is performed by a multivariate linear least squares regression analysis. This linear approach determines a coefficient matrix $\boldsymbol{\beta}$ such that the quadratic errors of noise term $\boldsymbol{v}_r$ are minimized for the calibration data. It can be well understood that for such approach the quality and dimensionality of the calibration data plays an important role in the overall validity of coefficient matrix $\boldsymbol{\beta}$. The calibration dataset used for this approach is identical to that of all other algorithms and is detailed in Chapter 6.

Next to the coefficient matrix, thermal offset vector ζ for compensation of thermal effects of the bulk deformation is to be calibrated. This is achieved by applying a reference load for which strain levels are known. In such case, the thermal offset can be determined. Due to the significant variance of thermal strain, this calibration is performed on a regular basis. For the load estimation quality studies, the re-calibration is performed during unloaded conditions (test rig, every 5 min) and lifting of the wheel (test vehicle, every half an hour) to avoid large estimation errors. During the application study for load based anti-lock braking, the system is re-calibrated prior to each braking manoeuver.

4.2.5 Running the algorithm

For functioning of the algorithm, the ball-pass frequency f_{bp} must be supplied. In the current study this external input is obtained from the available wheel-speed encoders. Due to the nearly fixed relationship between ball-pass frequency f_{bp} and the bearing rotational frequency this has shown to be effective. In case no speed encoders are available, a frequency estimation can be applied.

4.3 Local strain data-driven approach

The second algorithm, the *local strain (semi-model) data-driven approach*, considers model based conditioning of the local strain. Although this requires a considerably more complex conditioning procedure it results in a higher output dimensionality due to separation of in- and outboard effects and to thermal invariance because of the focus on local strain.

The conditioning, aimed at extracting the amplitudes of both in- and outboard local strain, is performed in two steps. In the first stage, the local strain is obtained by the use of a speed dependent high-pass filter. In the second stage Kalman filtering [41] is applied as an Extended Kalman Filter (EKF) including the proposed local strain model is used for estimating the in- and outboard strain amplitudes. Subsequently the bearing loading is calculated by the use of a coefficient mapping. The latter method is similar to the bulk deformation based approach, and therefore both algorithms allow for a comparison between the bulk and local strain based methodologies. The general scheme of the algorithm is presented in Figure 4.5.

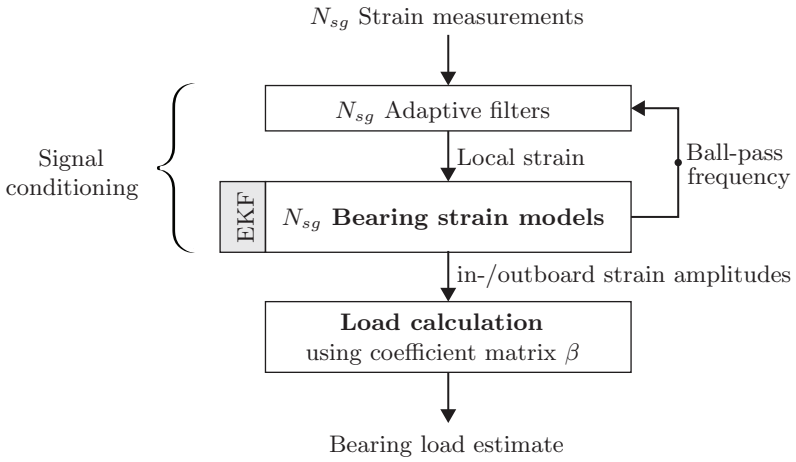

Figure 4.5: Overview of the semi-model local strain data-driven approach

In the following, the three algorithm phases, of which the first two can be considered to be the signal conditioning phases, are extended.

4.3.1 Adaptive filters

In this first stage of the algorithm all N_{sg} strain measurements are high-pass filtered to extract the local strain component from the raw measurements. Effective separation of the local effects from the bulk deformation is only possible when the ball-pass frequency f_{bp} exceeds the bandwidth of the external load and bulk

deformation. It is assumed that the latter is either static and known, or dynamic and related to the rotational frequency of the bearing. For high-pass filtering a 2^{nd} order Butterworth filter is proposed, with a static or dynamic cut-off frequency f_c of:

$$\begin{array}{lll} f_c = c_{bw}\bar{f}_{bw} & \text{if} & \bar{f}_{bw} = \text{const.} \\ f_c = c_{bp}f_{bp} & \text{if} & \bar{f}_{bw} \neq \text{const.} \end{array} \tag{4.4}$$

where $\bar{f}_{bw}$ is the upper frequency of the static bearing load bandwidth, f_{bp} is the ball-pass frequency estimate and c_{bw} (> 1) and c_{bp} (< 1) are tuning constants providing separation between bulk deformation and ball-pass frequencies. The case specific tuning constants should be chosen such that in operating conditions the high-pass filter provides respectively maximal and minimal attenuation of low and high frequency content such to maximize signal to noise ratio of the local strain. The ball-pass frequency for adapting the filter frequency is obtained from the state vector of the subsequent algorithm stage.

4.3.2 EKF bearing strain model

In the second conditioning stage of this algorithm the aim is to estimate the in- and outboard strain amplitudes from the local strain measurement. As the contact angle is not available in this approach, the strain gauge sensitivity cannot be determined. Therefore the strain model of Chapter 3 is simplified by setting both sensitivity η_i and η_o of (3.1) to one and substitution of rolling element load Q by strain amplitude A:

$$\varepsilon_l(\psi) = A_i(\psi)G_i(\varphi_i) + A_o(\psi)G_o(\varphi_o) \tag{4.5}$$

where A_i and A_o are the in- and outboard local strain amplitudes respectively. This simplified model is implemented in an EKF approach to estimate in- and outboard local strain amplitudes, phases and frequencies from the N_{sg} local strain measurements. In order to do so, for each local strain measurement a separate EKF is set up according to the description as follows.

The EKF system equations are defined as:

$$\boldsymbol{x}_{n,k} = \boldsymbol{F}\boldsymbol{x}_{n,k-1} + \boldsymbol{w}_n \tag{4.6}$$

$$\boldsymbol{y}_{n,k} = f(\boldsymbol{x}_{n,k}) + \boldsymbol{v}_n \tag{4.7}$$

where $\boldsymbol{x}_n$ and $\boldsymbol{y}_n$ are respectively the state and measurement vector of the n^{th} filter, $\boldsymbol{F}$ is the linear process model, f is the non-linear measurement model and $\boldsymbol{w}_n$ and $\boldsymbol{v}_n$ are the n^{th} filter process and measurement noise matrixes respectively, which are assumed as zero-mean Gaussian white noise with covariance $\boldsymbol{Q}_n$ and

$\boldsymbol{R}_n$. The state, measurement and external input vector are defined as:

$$\boldsymbol{x}_{n,k} = \begin{bmatrix} \omega_{n,i,k} & \varphi_{n,i,k} & A_{n,i,k} & \omega_{n,o,k} & \varphi_{n,o,k} & A_{n,o,k} \end{bmatrix}^T \tag{4.8}$$

$$\boldsymbol{y}_{n,k} = \begin{bmatrix} \varepsilon_{n,l,k} & \bar{\omega}_{i,k} & \bar{\omega}_{o,k} \end{bmatrix}^T \tag{4.9}$$

where ω_n is the ball-pass frequency, $\varepsilon_{n,l}$ is the local strain determined by the adaptive filtering phase and $\bar{\omega}_i$ and $\bar{\omega}_o$ are pseudo measurements of the ball-pass frequency.

The ball-pass frequency pseudo measurements are added to avoid observability issues during low excitation of the respective raceways and equal the current most trusted ball-pass frequency estimate. The linear process model $\boldsymbol{F}$ is defined as the identity matrix with two off-diagonal terms on $(2,1)$ and $(5,4)$ equalling $1/t_s$, where t_s is the sampling period, to increment in- and outboard phases with the current respective rotational frequency estimates.

Extended Kalman Filter equations

initialization

$$\hat{\boldsymbol{x}}_{n,0} = E[\boldsymbol{x}_n] \tag{4.10}$$

$$\boldsymbol{P}_{n,0} = E[(\boldsymbol{x}_n - \hat{\boldsymbol{x}}_{n,0})(\boldsymbol{x}_n - \hat{\boldsymbol{x}}_{n,0})] \tag{4.11}$$

1. Time update

$$\hat{\boldsymbol{x}}^-_{n,k} = \boldsymbol{F}\hat{\boldsymbol{x}}_{n,k-1} \tag{4.12}$$

$$\boldsymbol{P}^-_{n,k} = \boldsymbol{F}\boldsymbol{P}_{n,k-1}\boldsymbol{F}^T + \boldsymbol{Q}_{n,k} \tag{4.13}$$

2. Measurement update

$$\boldsymbol{K}_{n,k} = \boldsymbol{P}^-_{n,k}\boldsymbol{H}^T_{n,k}(\boldsymbol{H}_{n,k}\boldsymbol{P}^-_{n,k}\boldsymbol{H}^T_{n,k} + \boldsymbol{R}_{n,k})^{-1} \tag{4.14}$$

$$\hat{\boldsymbol{x}}_{n,k} = \hat{\boldsymbol{x}}^-_{n,k} + \boldsymbol{K}_{n,k}(\boldsymbol{y}_{n,k} - f(\hat{\boldsymbol{x}}^-_{n,k}, \boldsymbol{u}_{n,k})) \tag{4.15}$$

$$\boldsymbol{P}_{n,k} = \boldsymbol{P}^-_{n,k} - \boldsymbol{K}_{n,k}\boldsymbol{H}_{n,k}\boldsymbol{P}^-_{n,k} \tag{4.16}$$

where $\boldsymbol{H}_{n,k} = \partial f(\hat{\boldsymbol{x}}^-_{n,k})/\partial\hat{\boldsymbol{x}}^-_{n,k}$, which is the linearization of the output equation at the current state estimate.

4.3.3 Load calculation

In line with the bulk deformation based approach, a coefficient based load reconstruction phase is applied. First all in- and outboard strain amplitudes determined by the N_{sg} parallel EKF filters are combined in one local strain amplitude vector $\boldsymbol{x}_a$ that considers both first and second order terms:

$$\begin{aligned}\boldsymbol{x}_a = \Big[&A_{1,i} \quad \dots \quad A_{N_{sg},i} \quad A_{1,o} \quad \dots \quad A_{N_{sg},o} \\ &A^2_{1,i} \quad \dots \quad A^2_{N_{sg},i} \quad A^2_{1,o} \quad \dots \quad A^2_{N_{sg},o}\Big]\end{aligned} \tag{4.17}$$

Using the strain amplitude vector, the bearing loads are calculated by multiplication with coefficient matrix $\boldsymbol{\beta}_a$:

$$\boldsymbol{y}_a = \boldsymbol{x}_a \boldsymbol{\beta}_a + \boldsymbol{v}_a \tag{4.18}$$

where $\boldsymbol{y}_a$ is the vector of bearing load estimates, $\boldsymbol{x}_a$ is the local strain amplitude vector, $\boldsymbol{\beta}_a$ is the coefficient matrix and $\boldsymbol{v}_a$ is the noise term.

4.3.4 Tuning

As common in the application of Kalman filtering, the process and measurement noise covariance $\boldsymbol{Q}$ and $\boldsymbol{R}$ matrixes are tuned for improved convergence and robustness of the nonlinear filters. More specifically, a rule based tuning is applied for changing these matrixes when either a positive or negative tilting moment is applied to the bearing. This is particularly effective as both situations consider significant differences in raceway loading and therefore excitation of the strain measurement locations.

4.3.5 Calibration

Calibration of coefficient matrix $\boldsymbol{\beta}_a$ is performed by a multivariate linear least squares regression analysis identical to the approach for the *bulk deformation data-driven approach*. Additionally, the same calibration data, detailed in Chapter 6, is used for calibration. In case of any N_h harmonics considered in the periodic transfer function, these need to be included in the calibration procedure as well.

4.3.6 Running the algorithm

For robust initialization of the algorithm, the initial rotational frequency is required. In the experimental setup, this is acquired using the wheel speed encoders. In contradiction to algorithm 1, while running, no external input of the ball-pass frequency f_{bp} is required as it is estimated within the EKF. The latter thus also functions as frequency estimator for the adaptive filters.

4.4 Local strain model based approach

This third algorithm, the *local strain model based approach*, extends the second algorithm by implementation of a model based load calculation stage. Due to this model based approach, principal relationships are defined by physical modelling and therefore the chance of over-fitting and the amount of parameters subject to calibration are decreased. Additionally, physical meaning is added to the calibration parameters.

The algorithm, shown in overview in Figure 4.6, is characterized by two subsequent non-linear Kalman filters. The first filter, an EKF, implements the strain model for translation of local strains to rolling element loads. The second filter, an Unscented Kalman Filter [40, 98] (UKF) includes the bearing load model for translation of these element loads to the bearing state. The bearing state is then used for calculation of the bearing loading and to update the raceway deformation that is included in the bearing load model.

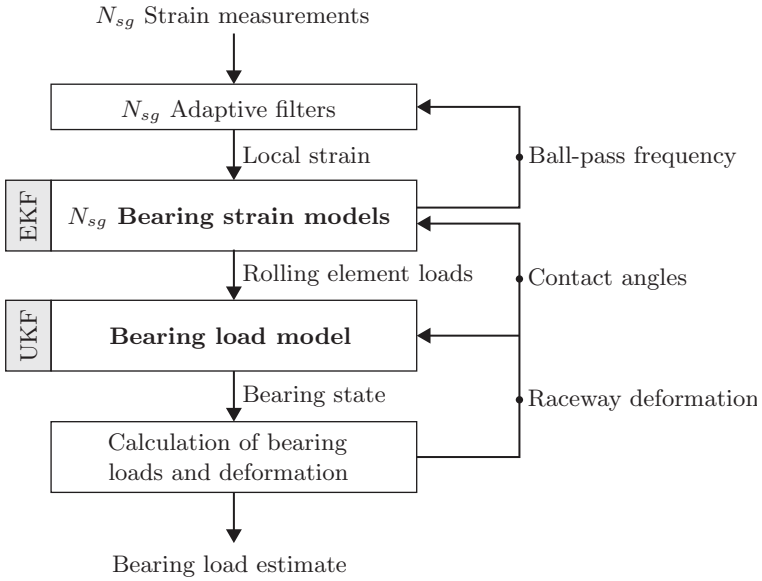

Figure 4.6: Overview of the local strain model based load reconstruction algorithm

For computational efficiency the first filter is of the EKF type, whereas an UKF is applied in the second stage due to the high non-linearity of the model. Besides for simplified tuning furthermore a cascaded approach is chosen as two independent physical phenomena without cross-covariance are described.

In the following the four algorithm phases are extended. The first two phases consider conditioning of the local strain in a slightly extended manner as algorithm two as contact angles are now available due to implementation of the bearing

load model. The latter two phases apply this load model in a model based load reconstruction approach.

4.4.1 Adaptive filtering

The adaptive filtering phase of this algorithm is identical to the method applied in the *local strain data-driven approach*. For its description the reader is referred to Subsection 4.3.1.

4.4.2 EKF strain model

In line with the semi-model based approach, an EKF is used for the local strain analysis. In contradiction to the second algorithm, the original description of Chapter 3 can be implemented as contact angles are available from the subsequent load calculation stage. By the use of the strain model local in- and outboard rolling element forces, phases and frequencies from the N_{sg} conditioned strain measurements can be estimated. For each conditioned strain measurement a separate filter is set up according to the description as follows.

The EKF system equations are defined as:

$$\boldsymbol{x}_{n,k} = \boldsymbol{F}\boldsymbol{x}_{n,k-1} + \boldsymbol{w}_n \tag{4.19}$$

$$\boldsymbol{y}_{n,k} = f(\boldsymbol{x}_{n,k}, \boldsymbol{u}_{n,k}) + \boldsymbol{v}_n \tag{4.20}$$

where $\boldsymbol{x}_n$ and $\boldsymbol{y}_n$ are respectively the state and measurement vector of the n^{th} filter, $\boldsymbol{F}$ is the linear process model, f is the non-linear measurement model, u_n is the external input vector and $\boldsymbol{w}_n$ and $\boldsymbol{v}_n$ are the n^{th} filter process and measurement noise matrixes respectively, which are assumed as zero-mean Gaussian white noise with covariance $\boldsymbol{Q}_n$ and $\boldsymbol{R}_n$. The state, measurement and external input vector are defined as:

$$\boldsymbol{x}_{n,k} = \begin{bmatrix} \omega_{n,i,k} & \varphi_{n,i,k} & Q_{n,i,k} & \omega_{n,o,k} & \varphi_{n,o,k} & Q_{n,o,k} \end{bmatrix}^T \tag{4.21}$$

$$\boldsymbol{y}_{n,k} = \begin{bmatrix} \varepsilon_{n,l,k} & \bar{\omega}_{i,k} & \bar{\omega}_{o,k} \end{bmatrix}^T \tag{4.22}$$

$$\boldsymbol{u}_{n,k} = \begin{bmatrix} \alpha_{n,i,k} & \alpha_{n,o,k} \end{bmatrix}^T \tag{4.23}$$

where ω_n is the ball-pass frequency, $\varepsilon_{n,l}$ is the local strain determined by the adaptive filtering phase, $\alpha_{ib,k}$ and $\alpha_{ob,k}$ are the rolling element contact angles obtained from the bearing load calculation stage for the n^{th} filter and $\bar{\omega}_i$ and $\bar{\omega}_o$ are pseudo measurements of the ball-pass frequency. The i and o subscripts refer

to in- and outboard effects respectively.

In line with algorithm 2, the ball-pass frequency pseudo measurements are added to avoid observability issues during low excitation of the respective raceways and equal the current most trusted estimated ball-pass frequency. The linear process model and the applied Extended Kalman Filtering equations are identical to the description in section 4.3.2.

4.4.3 UKF bearing model

The bearing model is implemented in an Unscented Kalman Filter (UKF) to estimate the bearing state based on the estimated rolling element forces. The UKF system equations are defined as follows:

$$\boldsymbol{x}_{b,k} = \boldsymbol{x}_{b,k-1} + \boldsymbol{w}_b \tag{4.24}$$

$$\boldsymbol{y}_{b,k} = g(\boldsymbol{x}_{b,k}, \boldsymbol{u}_{b,k}) + \boldsymbol{v}_b \tag{4.25}$$

where $\boldsymbol{x}_b$ is the state vector, y_b is the measurement vector, g is the non-linear measurement model, $\boldsymbol{u}_b$ is the external input vector and $\boldsymbol{w}_b$ and $\boldsymbol{v}_b$ are the process and measurement noise which are assumed to be zero-mean Gaussian white noise with covariance of respectively $\boldsymbol{Q}_b$ and $\boldsymbol{R}_b$. Note that no process model is described as it equals the identity matrix. The state, measurement and external input vector are defined as:

$$\boldsymbol{x}_b = \begin{bmatrix} \delta_x & \delta_y & \delta_z & \gamma_x & \gamma_y \end{bmatrix}^T \tag{4.26}$$

$$\boldsymbol{y}_b = \begin{bmatrix} \delta_{i,1} & \delta_{o,1} & \dots & \delta_{i,N_{sg}} & \delta_{o,N_{sg}} \end{bmatrix}^T \tag{4.27}$$

$$\boldsymbol{u}_b = \begin{bmatrix} u_r(\psi_1) & \dots & u_r(\psi_{N_{sg}}) \end{bmatrix}^T \tag{4.28}$$

where the measurement vector consists of the normal approaches calculated using the previously estimated rolling element forces using (2.1). This transformation is applied as this leads to a better convergence of the bearing model due to the nature of (2.1) that results in a discontinuity in the calculated element force. The raceway deformation is regarded as external input and is obtained from the subsequent bearing model calculation phase. The applied UKF equations are described below.

Unscented Kalman Filter equations

initialization

$$\hat{\boldsymbol{x}}_{b,0} = E[\boldsymbol{x}_b] \tag{4.29}$$

$$\boldsymbol{P}_{b,0} = E[(\boldsymbol{x}_b - \hat{\boldsymbol{x}}_{b,0})(\boldsymbol{x}_b - \hat{\boldsymbol{x}}_{b,0})] \tag{4.30}$$

$$W_0^c = \lambda/(L+\lambda) + (1 - \alpha^2 + \beta) \tag{4.31}$$

$$W_i^c = 1/(2(L+\lambda)) \quad i = 1, ..., 2L \tag{4.32}$$

1. Time update

$$\hat{\boldsymbol{x}}_{b,k}^- = \hat{\boldsymbol{x}}_{b,k-1} \tag{4.33}$$

$$\boldsymbol{P}_{b,k}^- = \boldsymbol{P}_{b,k-1} + \boldsymbol{Q}_{b,k} \tag{4.34}$$

$$\boldsymbol{X}_{b,k}^- = \left[\hat{\boldsymbol{x}}_{b,k}^- \quad \hat{\boldsymbol{x}}_{b,k}^- + \gamma\sqrt{\boldsymbol{P}_{b,k}^-} \quad \hat{\boldsymbol{x}}_{b,k}^- - \gamma\sqrt{\boldsymbol{P}_{b,k}^-}\right] \tag{4.35}$$

$$\boldsymbol{Y}_{b,k}^- = g(\boldsymbol{X}_{b,k}^-, \boldsymbol{u}_{b,k}) \tag{4.36}$$

$$\hat{\boldsymbol{y}}_{b,k}^- = g(\hat{\boldsymbol{x}}_{b,k}^-, \boldsymbol{u}_{b,k}) \tag{4.37}$$

2. Measurement update

$$\boldsymbol{P}_{\hat{\boldsymbol{y}}_{b,k}\hat{\boldsymbol{y}}_{b,k}} = \sum_{i=0}^{2L} W_i^c (\boldsymbol{Y}_{b,k}^- - \hat{\boldsymbol{y}}_{b,k}^-)(\boldsymbol{Y}_{b,k}^- - \hat{\boldsymbol{y}}_{b,k}^-)^T + \boldsymbol{R}_{b,k} \tag{4.38}$$

$$\boldsymbol{P}_{\hat{\boldsymbol{x}}_{b,k}\hat{\boldsymbol{y}}_{b,k}} = \sum_{i=0}^{2L} W_i^c (\boldsymbol{X}_{b,k}^- - \hat{\boldsymbol{x}}_{b,k}^-)(\boldsymbol{Y}_{b,k}^- - \hat{\boldsymbol{y}}_{b,k}^-)^T \tag{4.39}$$

$$\boldsymbol{K}_{b,k} = \boldsymbol{P}_{\hat{\boldsymbol{x}}_{b,k}\hat{\boldsymbol{y}}_{b,k}} \boldsymbol{P}_{\hat{\boldsymbol{y}}_{b,k}\hat{\boldsymbol{y}}_{b,k}}^{-1} \tag{4.40}$$

$$\hat{\boldsymbol{x}}_{b,k} = \hat{\boldsymbol{x}}_{b,k}^- + \boldsymbol{K}_{b,k}(\boldsymbol{y}_{b,k} - \hat{\boldsymbol{y}}_{b,k}) \tag{4.41}$$

$$\boldsymbol{P}_{b,k} = \boldsymbol{P}_{b,k}^{-} - \boldsymbol{K}_{b,k}\boldsymbol{P}_{\hat{\boldsymbol{y}}_{b,k}\hat{\boldsymbol{y}}_{b,k}}\boldsymbol{K}_{b,k}^{T} \tag{4.42}$$

where α and β control the sigma point spread, L is the length of the state vector and λ is defined as $\lambda = \alpha^2 L - L$.

4.4.4 Calculation of load and deformation

By the use of UKF state vector and (2.1 - 2.12) all rolling element loads, contact angles and subsequent bearing loads can be calculated based on the current raceway deformation estimate. The calculated rolling element loads are then used for updating the raceway deformation estimate by the use of (2.19).

4.4.5 Tuning

In line with the *local strain data-driven approach*, a rule based tuning of covariance matrixes $\boldsymbol{Q}$ and $\boldsymbol{R}$ of the EKF filter is proposed. Additionally, the measurement covariance matrix of the UKF is adjusted to omit unloaded raceways in the calculation of the bearing state. The latter is applied as unloaded conditions provide no information to the UKF. The tuning of the EKF is applied based on internal filter states, the UKF is tuned based on the EKF state vector.

4.4.6 Calibration

A considerable advantage of a model based approach with respect to data-driven methods is that parameters have physical meaning and therefore can be bounded or defined a priori such to minimize calibration effort. The choice for the latter or a calibration procedure depends on parameter sensitivity and accuracy at which the parameter can be determined on beforehand.

As the bearing model is a validated modelling part it is defined a priori. By the use of technical drawings the geometrical parameters are defined whilst the bearing compliance is determined by a Finite Element study as explained in Chapter 2.

Quantification of the introduced strain model parameters is achieved by the use of a calibration routine. The periodic transfer function and sensitivity polynomial orders are set to $N_h = 2$ and $N_p = 3$ respectively. As the bearing is plane symmetric, the front and rear strain model parameters are considered to be equal, resulting in a total of 18 parameters for calibration. The calibration is performed by a non-linear calibration routine with the aim of minimizing the quadratic error of noise term $\boldsymbol{v}_b$.

4.4.7 Running the algorithm

In line with algorithm 2, the initial rotational frequency is required as prior knowledge for robust convergence after initialization of the algorithm. This information is obtained from the available wheel-speed encoders. As the algorithm does not require any external inputs, no additional information is required while running the algorithm.

4.5 Conclusion

In this Chapter a physics based load reconstruction algorithm is developed based on the previously introduced bearing load and strain model. This novel algorithm, coined as the *local strain model based approach*, applies the bearing strain model for conditioning of the local strain and implements the bearing load model for reconstruction of the bearing loading. Additionally a *local strain data-driven approach* and *bulk deformation data-driven approach* are introduced. The latter represents the state-of-the-art, whereas the former is partially model driven as it employs a physics based conditioning approach.

The three algorithms represent the chronological development and milestones of the bearing load reconstruction approaches developed during this thesis. All are incorporated in this final work as the comparison of the algorithm results allows for addressing the advantages of physics based modelling in the field of load reconstruction. The latter is presented in the following of this thesis.

Chapter 5

Prototypes and Testing Facilities

The three proposed load reconstruction algorithms are compared and validated by an experimental study in both laboratory and field conditions. For this purpose, an off-the-shelf wheel-end bearing is instrumented with strain gauges and extensively tested on both a dedicated test-rig as well as on a test vehicle. In this Chapter the bearing instrumentation as well as the test facilities are introduced.

This Chapter presents an extended description of the experimental setup and facilities developed and used for all publications related to this thesis.

5.1 Instrumented bearing prototype

For experimental testing and validation of the developed load reconstruction algorithms a Hub Bearing Unit 3 (HBU3) type wheel-end bearing is chosen. This bearing type is commonly used in automotive wheel-end applications. It is a double row angular contact ball bearing that is designed to be light and compact. It provides its own housing and both the inner and outer-ring contain a flange for mounting by bolts to the wheel and steering knuckle respectively. The relatively thin outer-ring structure deforms considerably, even at normal operating conditions, and therefore serves well for deformation based load reconstruction.

As a BMW 5-series test vehicle is considered, the wheel-end bearings of this particular vehicle type, shown in Figure 5.1, are instrumented for testing. During the course of this thesis, two different sets of prototypes have been developed which differ with respect to the amount and placement of strain gauges.

The first set of prototypes, instrumented with six strain gauges equally spaced around the bearing circumference, is used for proof of concept studies and the Anti-lock application study as presented in Chapter 7. The second set of prototypes, instrumented with four strain gauges at a 90 degree interval placed in line with the principal axis of the bearing, are used for the experimental study presented in this Chapter.

Both sets of instrumented bearings are equipped with general-purpose strain gauges aligned such that the bearing circumferential strain is measured. The strain gauges, specified in Table 5.1, are applied in a Wheatstone bridge setup and are protected from the harsh wheel-end environment by a silicone coating. As the signals coming from the bearing are low-voltage a well shielded wire is used to avoid electrical interference and thereby minimize noise levels. In both test setups the low-voltage signals are amplified by the use of a Peekel 9236 type amplifier.

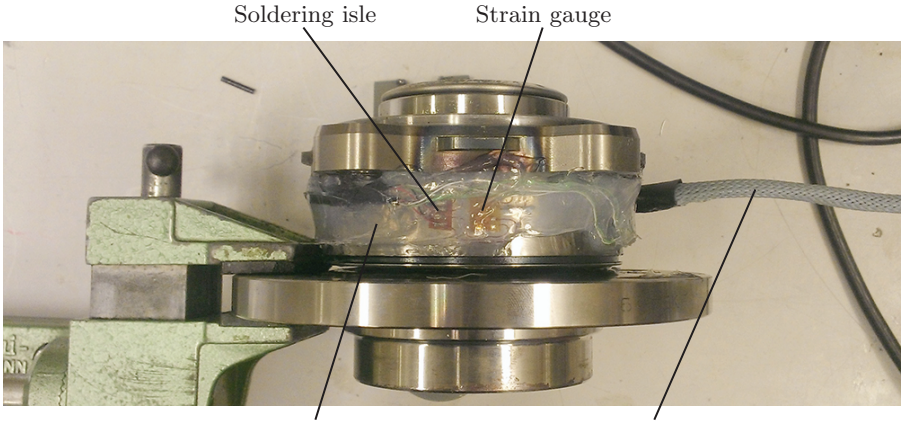

Figure 5.1: Top view of the instrumented bearing

Table 5.1: Strain gauge specifications

Parameter	**Value**
Type	CEA-06-062UR-350
Strain range	±3%
Resistance	350 Ohms
Gauge factor	2.150 ± 0.5%
Pattern Type	Rectangular Rosette
Active length	1.57 mm
Active width	1.57 mm
Operating temperature	-75 to 175 ºC

Initially the bearings are mounted in the bearing test rig for calibration and testing in line with Section 5.2. Afterwards they are fitted to the test vehicle as discussed in Section 5.3.

5.2 Bearing test system

For testing and validation of the bearing load measurement approach in laboratory conditions a dedicated bearing test rig is available at our industrial partner SKF. This test rig allows for extensive and repetitive bearing testing under various loading conditions while driven by an electric motor.

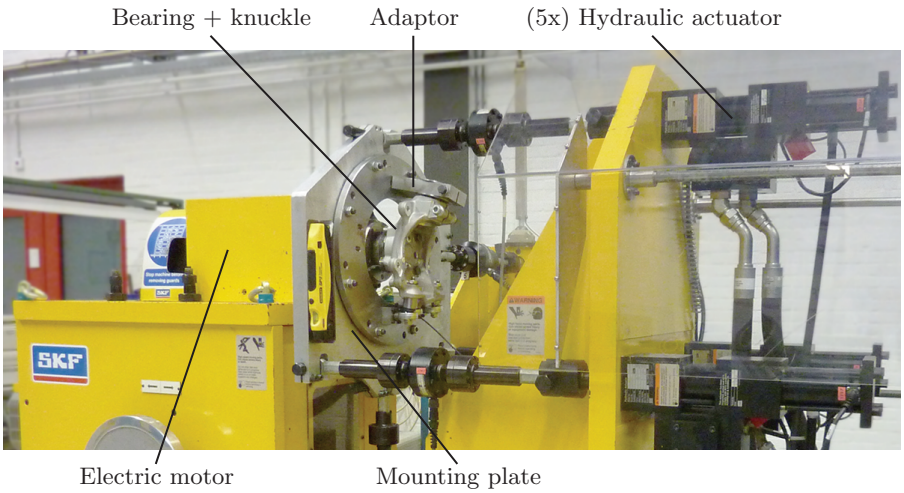

Figure 5.2: The bearing test system (BETSY) located at industrial partner SKF

The test system, shown in Figure 5.2, uses 5 hydraulic force controlled actuators to apply the bearing load on the setup. The wheel-end side of the bearing is connected to an electric motor via a shaft to drive the bearing. The knuckle is mounted to an aluminium plate via an adapter. Different adapters are available to connect various bearings/knuckles. The bandwidth of up to 10 Hz in combination with the large operating range and custom load profiles allows for road realistic loading of the instrumented bearings. The load range and rotational speeds that can be achieved by the test setup are indicated in Table 5.2.

Besides the ability to test for repeatability, a particular advantage with respect to real road testing, in which loads usually are coupled, is the possibility to provide custom loading patterns. The latter allows for testing for the response on excitation of individual loads as well as alternative load cases that are not necessarily road realistic. The latter helps to understand the general validity of the load reconstruction approaches.

The setup used for the experimental study consists of both the HBU3 bearing as well as the original BMW steering knuckle. The inner-ring flange of the bearing is connected to a driveshaft to the electric motor. The knuckle on the other hand is fixed to the mounting plate by the use of a custom made adaptor. In Figure 5.2 the setup is shown marking all discussed components. The steering knuckle is included

in the setup as it affects the deformation behaviour of the bearing considerably. Thereby boundary conditions of the test vehicle are mimicked such that differences between the laboratory and field setup are minimized. As noted by the results in Chapter 6, this leads to a good match between laboratory and field conditions. A notable consequence of the addition however resides in the increased flexibility of the setup that leads to minor deflections and rotations during heavily loaded conditions. The latter negatively affects the experimental results as any rotation results in misalignment of the applied loading and bearing coordinate system. As emphasis lies on assessment by comparison of the algorithms, and not specifically on performance, it is chosen not to compensate for this rotational effect.

Data acquisition is performed by the use of a Yokogawa DL750P mixed signal oscilloscope at a sampling rate of 2 kHz. The proposed load reconstruction algorithm is applied using Matlab on a regular PC.

Table 5.2: Excitation range of the bearing test system

Parameter		**Value**
Tilting moment	M_x	+/- 5kNm
Self-aligning moment	M_z	+/- 5kNm
Longitudinal force	F_x	+/- 15kN
Lateral force	F_y	+/- 15kN
Vertical force	F_z	+/- 15kN
Rotational speed	ω	0-3000 rpm
Load bandwidth		up to 10Hz

5.3 Test vehicle

To test and validate the load measurement approach and perform application studies on load based dynamics control a 2009 BMW 5-series production vehicle was modified and instrumented. As detailed in Figure 5.3 several modifications are made to the test vehicle, which are categorized by (1) Miscellaneous, (2) Load estimation and (3) Dynamics control modifications.

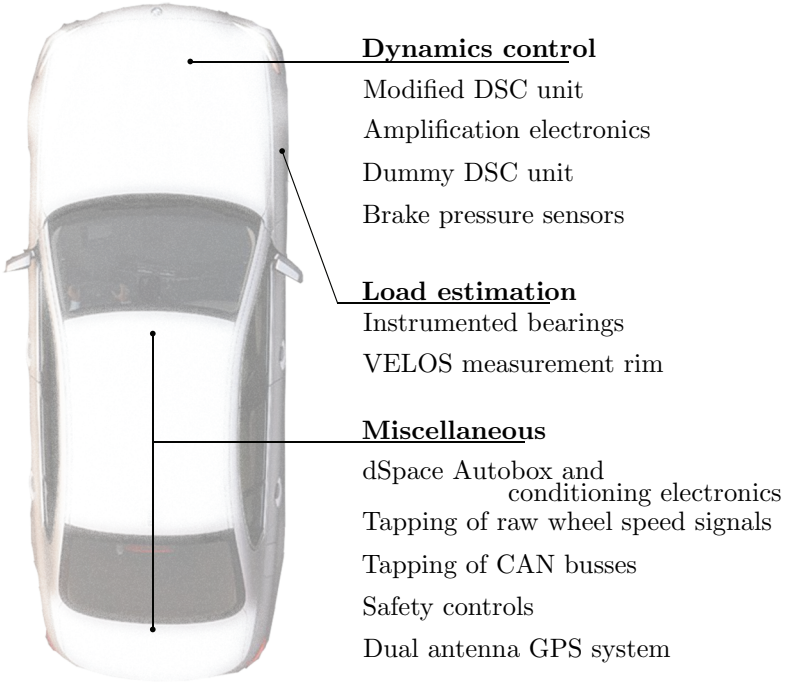

Figure 5.3: Modifications made to the test vehicle for this thesis

5.3.1 Miscellaneous

First of all, for the purpose of data acquisition, processing and real-time control determination a *dSPACE Autobox* platform (ds1005) is fitted in the trunk of the vehicle. The system is equipped with an AD/DA conversion board (DS2003), PWM / IO board (DS4002) and CAN communications board (DS4302).

Wheel speed signals are tapped directly from the original ABS sensors to obtain the raw data and minimal latency on the wheel speed readout. As the wheel-speed signals originally are current based, conditioning electronics are implemented to obtain a voltage based block signal that is then acquired by the dSPACE Autobox DS4002 PWM/IO board.

Both the powertrain (PT) and chassis (F) CAN busses are tapped to capture important vehicle information. The signals are tapped near the steering wheel and data acquisition is performed using the dSPACE Autobox DS4302 board.

A *dual antenna GPS system* on the roof of the vehicle is fitted for accurate measurement of the vehicle speed, direction and its location. Although the dual GPS antenna was added for other studies performed on the test vehicle, it was found very useful for the tracking of vehicle manoeuvers in the vast amount of data collected of the current study.

Lastly, *safety control* in the form of a safety button is added in the middle console of the dashboard. Pressing the safety button will turn of all actuation electronics (DSC control) in case of an emergency. The system is designed such that all sensors and data acquisition remains active when the safety button is pressed.

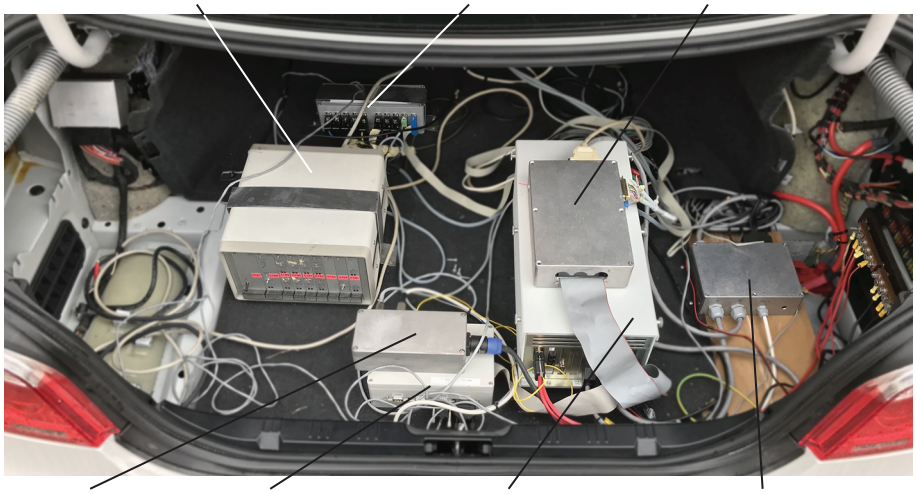

Figure 5.4: The trunk of the Delft University of Technology BMW test vehicle

5.3.2 Load estimation

Each wheel-end bearing is replaced by an *instrumented bearing* as detailed in Section 5.1. Well shielded wires connect these four instrumented bearings to the two (Peekel 9236 type) strain gauge amplifier boxes (1 for both front and 1 for both rear bearings). Data acquisition is performed by the DS2003 AD board of the dSPACE Autobox.

A VEhicle LOad Sensor (VELOS) *measurement rim* [82] is used as reference measurement of the tire forces and moments. The measurement rim has a mechanical decoupling between the various loading directions allowing for an accurate

measurement of each load by the use of strain gauges on its flexible members. A conditioning box in the rear of the vehicle serves as power supply and data conversion. Logging is performed using the dSPACE Autobox DS2003 AD board.

An important aspect for the experimental study is the alignment of the reference load measurement and bearing load estimate. As the measurement wheels coordinate system does not coincide with the bearing axis, a translation to the VELOS measurement output is applied. Furthermore, based on the steering wheel angle information obtained from the F-CAN, a correction is applied for rotation of both the measurement wheel and bearing based to ensure the axis system as presented in Section 6.1.

5.3.3 Dynamics control

The original Bosch *Dynamic Stability Control* (DSC) 8 unit is modified for active dynamics control. By dismantling the original DSC unit and installation of a custom coil pack and power electronics control of all hydraulic actuators (valves and pump) is obtained.

The *power electronics* are implemented to amplify the signals coming from the dSPACE AutoBox towards the hydraulic unit stage of the DSC unit. The control signals to the power electronics are generated by the DS4002 board installed in the dSPACE Autobox.

The modification on the DSC unit leaves the DSC ECU disconnected. As this leads to issues on the original vehicle software, a *dummy DSC unit* is installed in the vehicle. The original DSC cable is connected to this dummy unit and thereby

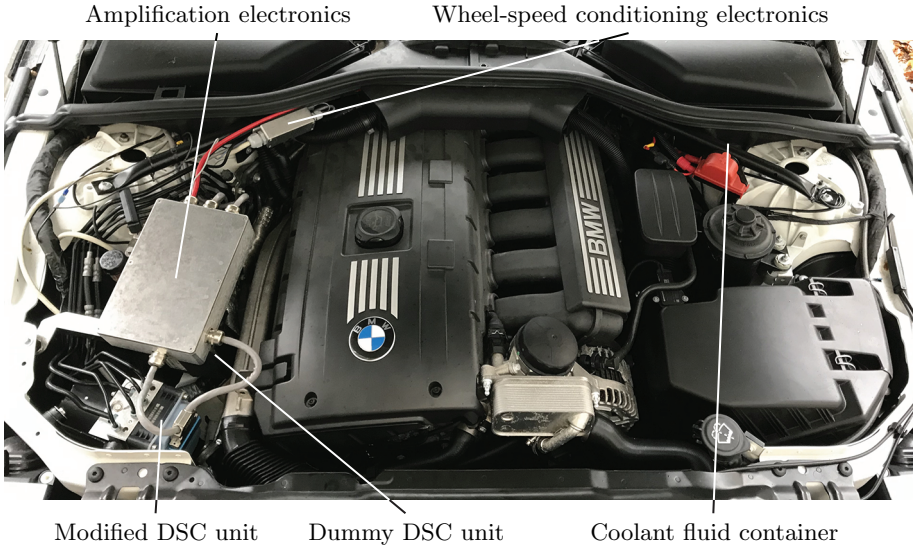

Figure 5.5: Modifications under the hood of the vehicle

software errors are avoided. As the dummy DSC is not connected to brake system hydraulics, its control actions are unanswered.

Brake pressure sensors are installed near each brake calliper to allow for closed loop brake pressure control. The brake pressure sensors are read out by the DS2003 AD board on the dSPACE Autobox.

5.4 Test track

Experimental testing with the test vehicle was performed on an old military airport. On this facility two different areas were available for testing: the runway was used for straight line braking and slaloming, whereas a the large airport apron was used for various manoeuvres as slaloming, constant cornering and step steering. Figure 5.6 and 5.6 show respectively the Valkenburg airstrip and apron.

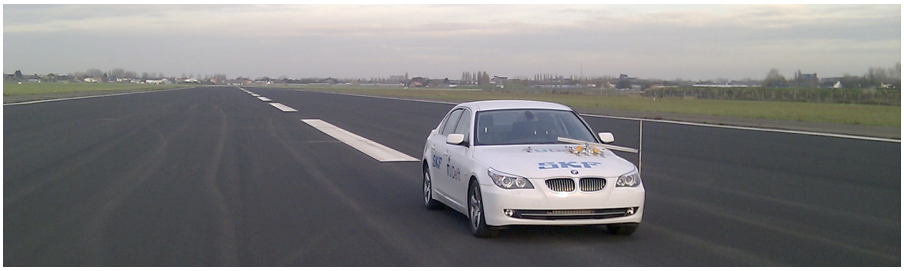

Figure 5.6: Test vehicle at the Valkenburg airstrip

Figure 5.7: Part of the Valkenburg apron

Chapter 6

Laboratory and Field Validation

This Chapter considers the experimental validation of the algorithms developed in Chapter 4 in both laboratory and field conditions. By analysis and comparison of the estimation results of each algorithm, the proposed strain conditioning and load calculations stages are assessed. The validation study shows that the proposed local strain conditioning approach leads to more accurate results than the state-of-the-art bulk deformation-based approach, due to invariance to thermal effects and the increased output dimensionality. The study furthermore shows that the proposed load calculation method outperforms the data-driven reference approach, because combined and alternative load cases are captured more accurately. The latter is a result of the knowledge introduced by modelling, which reduces the chances of overfitting and extends the functional domain beyond the calibrated region.

S. Kerst, B. Shyrokau and E. Holweg. "A model-based approach for the estimation of bearing forces and moments using outer-ring deformation", *Transactions on Industrial Electronics (2019): 10.1109/TIE.2019.2897510*.

6.1 Introduction

In this Chapter the three algorithms developed in Chapter 4 are experimentally validated by assessment of their functioning and estimation accuracy. As noted in Chapter 5, the validation study considers a vehicle wheel-end bearing. Although bearing load measurement would be of interest in various applications, this automotive application is of particular interest as various studies have emphasized the improvement in dynamics and safety systems that could be achieved based on wheel load information. Additionally, wheel-end bearings consider extensive variation in loading conditions and rotational speed, and therefore serve as an interesting case study.

As explained in Chapter 5, the bearing considered is a BMW 5-series wheel-end bearing. Validation is performed in both laboratory and field conditions with a dedicated test-rig and test vehicle respectively. By the use of load-cells (test rig) and a VELOS measurement rim (test vehicle) a reference bearing load measurement is available on each setup. Based on this reference measurement, each algorithm is assessed on its load estimation accuracy in both quantitative and qualitative terms.

As no experimental measures are available to analyse inner-behaviour of the bearing, algorithm validation is based on load estimation quality only. This complicates assessment of the signal conditioning and load calculation stages independently, as results might be unambiguous. However, due to the design of the three algorithms, a comparison study can be applied for proper assessment of both stages. As the *bulk-* and *local strain data-driven approaches* share a similar load reconstruction phase comparison of algorithm results allows for addressing the bulk and local strain conditioning methods. The *local strain data-driven* and *local strain model based approach* furthermore apply similar conditioning methods, and therefore allow for assessment of the data-driven and model based load reconstruction phases. Assessment based on only addressing the load estimation quality thus suffices to draw conclusions on both conditioning and load calculation stages due to the design of the three proposed algorithms.

In the following of this Chapter first algorithm calibration is discussed. This is followed by the experimental results including a brief analysis for each test. Afterwards a discussion is presented that reflects on the results. Finally conclusions are drawn.

6.2 Calibration

The estimation quality of each of the bearing load reconstruction approaches, as for any measurement approach, depends on the quality of calibration. For the current study, the latter is strongly related to the applied load cases during calibration, and more specifically, to the load magnitudes and orthogonality. The coefficient based load calculation stage in particular is highly dependent on calibration for proper functioning due to its data-driven nature.

In order to achieve good load estimation results for wheel-end conditions, a calibration set considering a variation of realistic wheel-end loading conditions is applied. Based on load measurements obtained during various test drives an extensive set of loading conditions is developed. The set includes step-steer, cornering, braking in the turn and slalom manoeuvers according to ISO standards. The load cases are combined and supplemented with noise and uncorrelated biases on individual channels to increase dimensionality and richness of the dataset. The calibration load pattern, which spans a total of 161 seconds, is applied to the instrumented bearing on the bearing test-rig. The results of this experiment are used according to the specific calibration procedures described in Chapter 4 to calibrate each algorithm.

It was chosen to perform calibration in laboratory conditions only as the test rig allows for more varied and orthogonal load cases than the test vehicle. Furthermore, a calibration in laboratory conditions is of interest from an industrialization point of view.

It must be noted that during braking the instrumented bearing and measurement rim loading differ due to their different location. As a consequence of their position, the brake tangential force is not noted by the VELOS measurement rim, whilst the instrumented bearing does observe this tangential force. In order to avoid issues related to this matter, no straight braking is considered for the field experiments. For the laboratory experiments braking is mimicked by supplementing the load case by a pure longitudinal braking force whilst omitting the brake tangential force. Although the latter is not reflective for braking in field conditions, it suffices for assessment of load reconstruction capabilities of the measurement approach.

6.3 Experimental results

The experimental validation considers a study on both the test rig and test vehicle. For the test rig two wheel-end realistic and one alternative load case are presented. The field experiment considers a cornering manoeuvre. For each load case a qualitative and quantitative analysis based on time domain results and root-mean-square (RMS) error are performed. The RMS error results are provided in both absolute and relative terms, where the latter is related to the Full Scale (FS) experimental excitation range. The FS excitation range for this study is indicated in Table 6.1. For each load case a brief discussion of important observations is provided. Afterwards the discussion section focuses on an in depth analysis and comparison of the different algorithm results to address the proposed signal conditioning and load calculation methods.

The load cases are evaluated on the estimation accuracy of longitudinal force F_x, vertical force F_z, tilting moment M_x and self-aligning moment M_z according to the sign convention as indicated in Figure 6.1. Lateral force F_y is omitted as the achieved accuracy by the use of only four strain gauges was too low. Additionally, the lateral force can be well estimated by the use of tilting moment M_x as they are physically linked. It is therefore considered more effective to estimate lateral force F_y by the use of tilting moment M_x.

Table 6.1: Full scale (FS) excitation range

Load		**Min**	**Max**
Longitudinal force	F_x	-5.5 kN	0.5 kN
Vertical force	F_z	1.5 kN	10.0 kN
Tilting moment	M_x	-0.7 kNm	2.1 kNm
Self-aligning moment	M_z	-0.4 kNm	0.2 kNm

Figure 6.1: Coordinate system considered for the experimental study

The experimental study focuses on load estimation in low-frequency and close to steady-state conditions to address the conditioning and load reconstruction approaches of all algorithms. A study to estimation bandwidth is omitted, as this is considered out of scope of this thesis. Nonetheless, the application study of Chapter 7 does confirm sufficient bandwidth for active dynamics control in automotive applications of the bulk deformation based approach. Considering the focus on low-frequency content of this Chapter, the laboratory and field data results are filtered using a 2^{nd} order Butterworth low pass filter with a cutoff frequency of 1 Hz.

6.3.1 Test rig: Cornering and braking combined loading

This first load case considers the bearing loading while cornering and braking to analyse the estimation results for combined loading. The experiment is performed on the bearing test rig at a constant rotational speed of 1000 rpm, resembling a driving speed of approximately 120 km/h. The time domain results are presented in Figure 6.2. The quantitative evaluation in both absolute as relative sense are presented in Table 6.2 and 6.3 respectively.

Regarding the *bulk deformation data-driven approach* one can observe a considerably biased but decent dynamic tracking of vertical force F_z and tilting moment M_x. Self-aligning moment M_z is well estimated whereas longitudinal force F_x is both offsetted and badly tracking the applied loading. The latter is best observed in the longitudinal force step at $t = 6$s. The noted biases are attributed to thermal drift of the bulk deformation measure, whereas the difficulty in tracking of longitudinal force F_x relates to inaccuracy of the coefficient based load calculation phase.

The *local strain data-driven approach* time domain results show notably good tracking of all loads except longitudinal force F_x. The latter is confirmed by the low RMS errors (all below 3.9% FS) for vertical force F_z, tilting moment M_x and self-aligning moment M_z whilst longitudinal force F_x is as high as 9.5 % FS. No thermal bias is noted on any of the load estimates. The low accuracy of longitudinal force F_x is attributed to limitations of the coefficient based load calculation phase.

The time domain results of the *local strain model based approach* shows good tracking of both forces and tilting moment M_x whilst the self-aligning moment M_z is estimated inaccurately. The latter is also noted in the high relative RMS error of 10.5 % FS, which is partially due to the limited FS domain for self-aligning moment M_z. The relatively larger error on M_z is related to the model based load

Table 6.2: Absolute RMS errors of load case 1

Load		**Bulk data-driven**	**Local data-driven**	**Local model-driven**
Longitudinal force	F_x	506 N	568 N	285 N
Vertical force	F_z	714 N	260 N	387 N
Tilting moment	M_x	288 Nm	47 Nm	56 Nm
Self-aligning moment	M_z	27 Nm	24 Nm	63 Nm

Table 6.3: Relative RMS errors of load case 1

Load		**Bulk data-driven**	**Local data-driven**	**Local model-driven**
Longitudinal force	F_x	8.5 %	9.5 %	4.7 %
Vertical force	F_z	8.4 %	3.1 %	4.6 %
Tilting moment	M_x	10.3 %	1.7 %	2.0 %
Self-aligning moment	M_z	4.4 %	3.9 %	10.5 %

calculation stage and flexibility or rotation of the test setup. The latter is detailed in the discussion section.

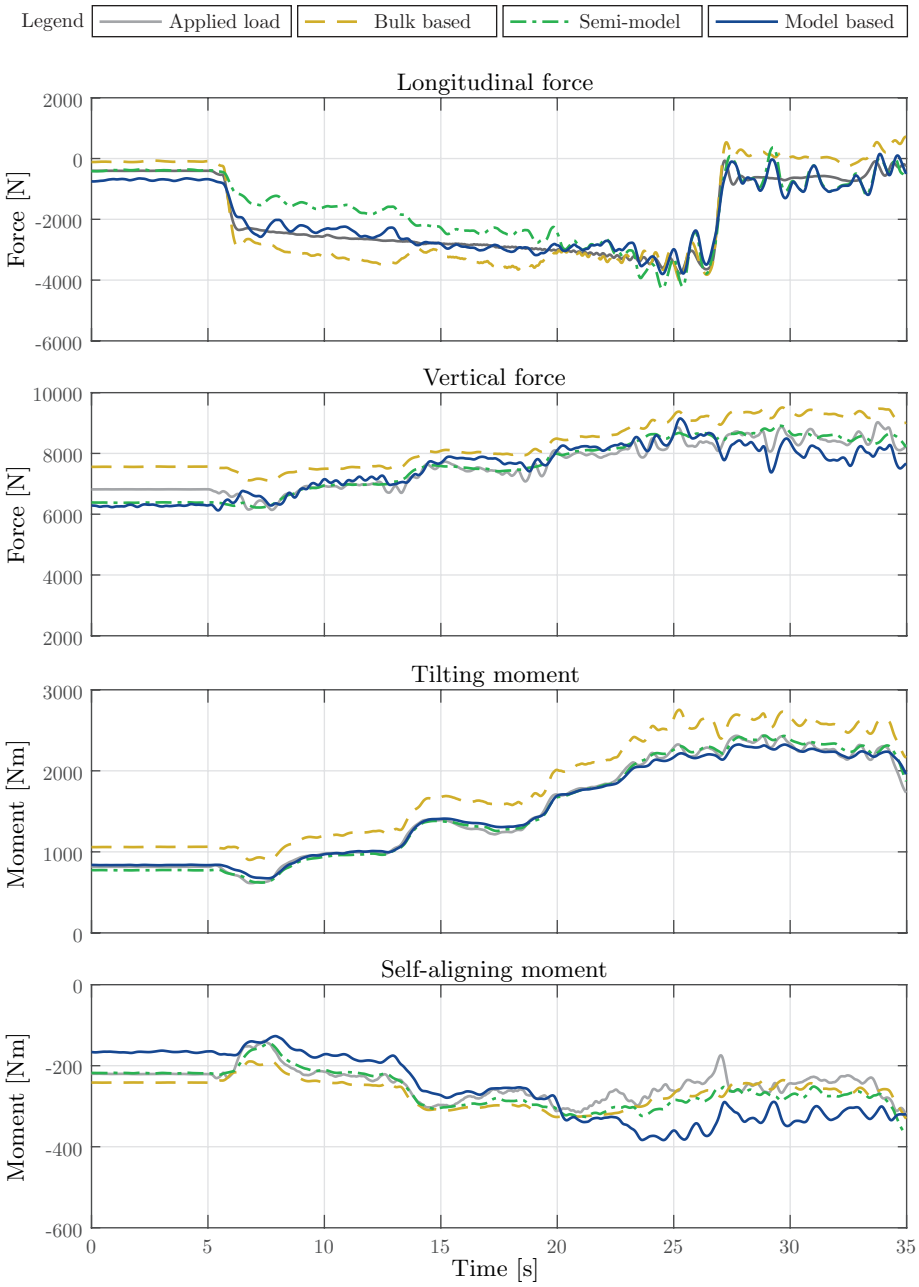

Figure 6.2: Time domain results of load case 1 performed on the bearing test rig

6.3.2 Test rig: Slalom manoeuver

This second load case regards the loading during a slalom manoeuvre to analyse the estimation quality for large internal bearing load variations. For this purpose a slalom manoeuver is particularly suitable, as it leads to an alternating loading on in- and outboard raceways. The test is performed at a constant rotational speed of 1000 rpm. Figure 6.3 shows the experimental results over time for all considered loads as well as the indication of the time domain used for the quantitative results presented in Table 6.4 and 6.5.

The *bulk deformation data-driven approach* for this load case leads to decent results for both force estimates, whereas notable errors on both moment estimates are observed. Tilting moment M_x is clearly underestimated in cornering conditions whilst self-aligning moment M_z is erroneous during cornering in one particular direction. In contradiction to load case 1, no bias related to thermal drift is observed. The estimation errors on both moment estimates are attributed to the incorrect mapping by the coefficient based load calculation phase.

The *local strain data-driven approach* shows a good tracking of all considered loads, which is reflected by the RMS errors that are all below 5 % FS. Although differences are small it is noted that longitudinal force F_x, albeit being unloaded, is again estimated with least accuracy. Although applying a similar load calculation phase as the bulk deformation based approach, it is noted that during cornering the tilting moment M_x is estimated more accurately. This difference is addressed in the discussion section.

For the *local strain model based approach* different regions in estimation quality can be observed; during the application of tilting moment M_x a good tracking is observed whilst large errors are encountered in the switching periods in-between. These errors are related to a complex interaction between both model based phases,

Table 6.4: Absolute RMS errors of load case 2

Load		**Bulk data-driven**	**Local data-driven**	**Local model-driven**
Longitudinal force	F_x	174 N	283 N	480 N
Vertical force	F_z	270 N	276 N	459 N
Tilting moment	M_x	157 Nm	46 Nm	57 Nm
Self-aligning moment	M_z	41 Nm	27 Nm	23 Nm

Table 6.5: Relative RMS errors of load case 2

Load		**Bulk data-driven**	**Local data-driven**	**Local model-driven**
Longitudinal force	F_x	2.9 %	4.7 %	8.0 %
Vertical force	F_z	3.2 %	3.2 %	5.4 %
Tilting moment	M_x	5.6 %	1.7 %	2.0 %
Self-aligning moment	M_z	6.9 %	4.5 %	3.8 %

and is discussed in the discussion section. For this experiment, the full model based approach results in the lowest accuracy when comparing to the other two methods.

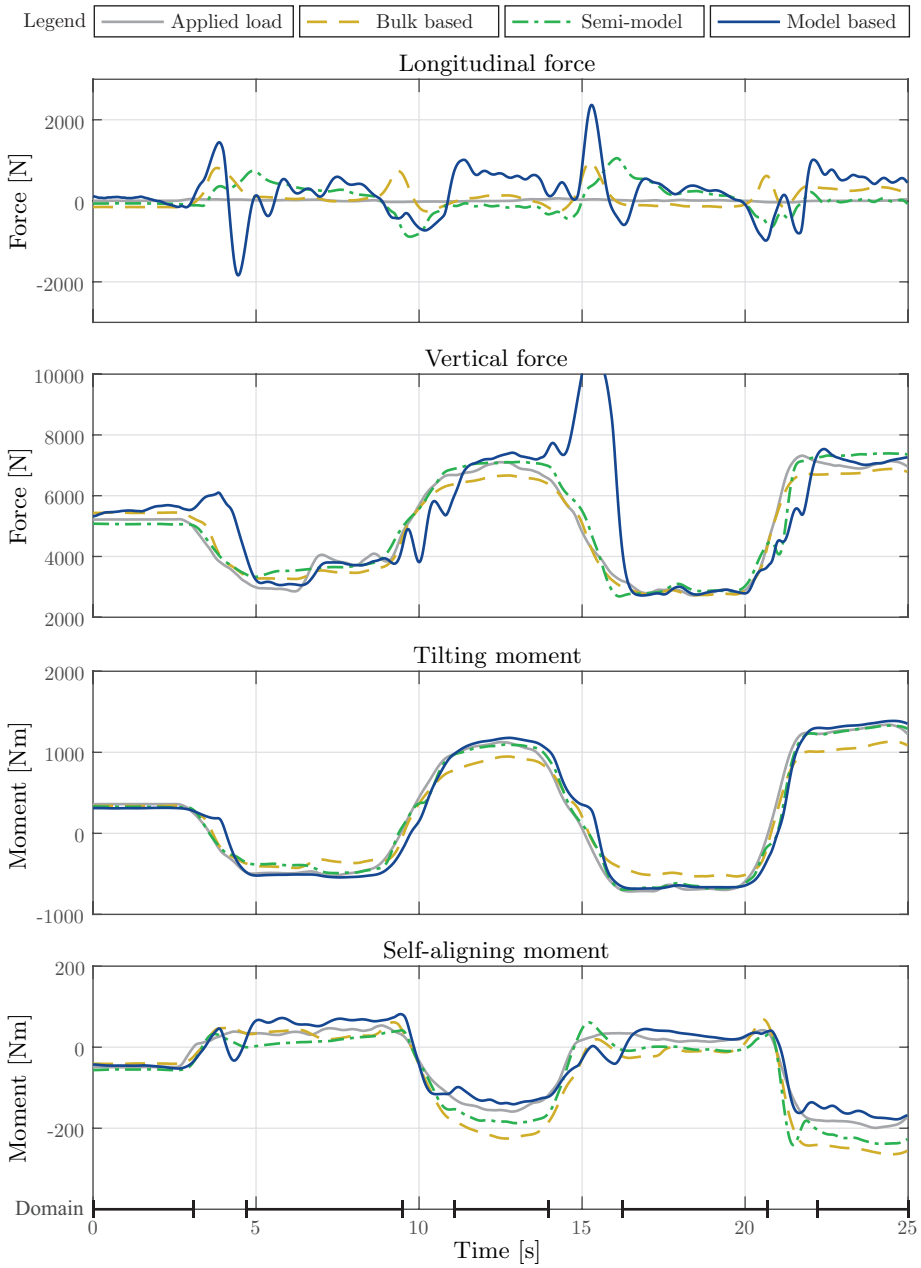

Figure 6.3: Time domain results of load case 2 performed on the bearing test rig including the domain indication for the quantitative results

6.3.3 Test rig: Alternative loading

This third load case regards an alternative loading which is not representative of any realistic wheel-end load as the lateral force normally accompanying tilting moment M_x is kept at 0 N. This load case shows less similarity to the calibration set and therefore allows for analysis of the predictive qualities of each reconstruction approach. The test is performed at a constant rotational speed of 1000 rpm. Figure 6.4 shows the time domain results and Tables 6.6 and 6.7 show the absolute and relative quantitative results of each approach.

The *bulk deformation data-driven approach* shows significant offsets and dynamic errors for all considered loads. Especially the moment estimates show little similarity to the applied loading showing RMS errors are as high as 21.6 and 29.5 % FS for tilting moment M_x and self-aligning moment M_z respectively. The considerable crosstalk observed in all estimates is a result of inaccuracy of the load reconstruction phase.

The results from the *local strain data-driven approach* are, in line with the bulk method, considerably erroneous. Crosstalk is observed in each estimate leading to bad tracking of the applied loads. The high RMS errors reflect this observation. The load calculation phase is of debit of these errors, as its predictive qualities are very limited.

The *local strain model based approach*, in contradiction to the other methods, shows good estimation results for all loads although an bias in vertical load F_z is noted. Omitting the bias, it is observed that the dynamic tracking of each load is good. Both moments are estimated particularly accurate, which is reflected by the low RMS errors of only 0.8 and 2.0 % FS for tilting moment M_x and self-aligning moment M_z respectively. Another interesting observation is made in vertical force estimate F_z, that shows some instability when tilting moment M_z becomes smaller.

Table 6.6: Absolute RMS errors of load case 3

Load		**Bulk data-driven**	**Local data-driven**	**Local model-driven**
Longitudinal force	F_x	417 N	826 N	235 N
Vertical force	F_z	818 N	2234 N	703 N
Tilting moment	M_x	604 Nm	212 Nm	23 Nm
Self-aligning moment	M_z	177 Nm	122 Nm	12 Nm

Table 6.7: Relative RMS errors of load case 3

Load		**Bulk data-driven**	**Local data-driven**	**Local model-driven**
Longitudinal force	F_x	6.9 %	13.8 %	3.9 %
Vertical force	F_z	9.6 %	26.2 %	8.3 %
Tilting moment	M_x	21.6 %	7.6 %	0.8 %
Self-aligning moment	M_z	29.5 %	20.4 %	2.0 %

This bearing model UKF related issue is extended in the discussion section.

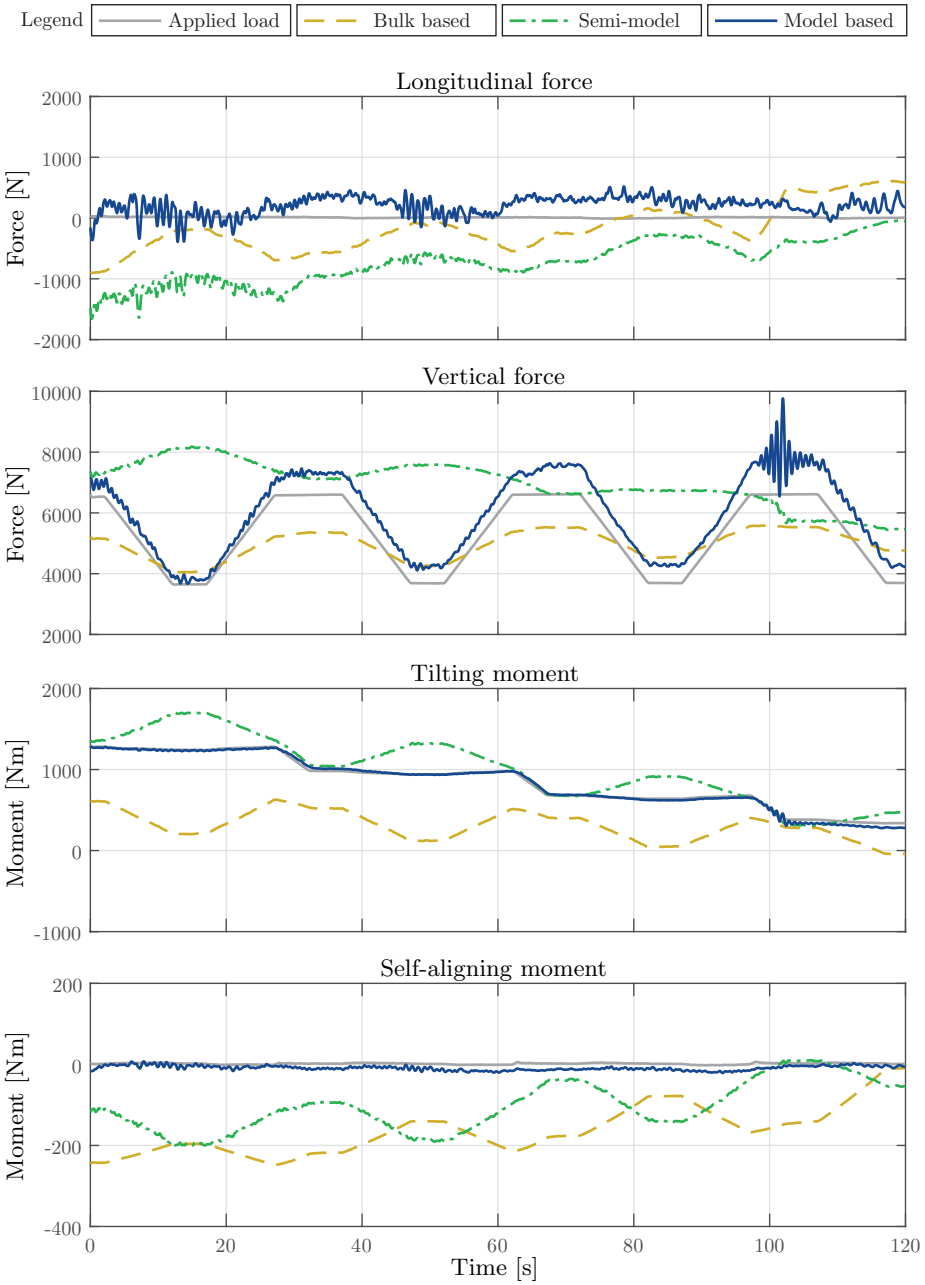

Figure 6.4: Time domain results of alternative load case 3

6.3.4 Test vehicle: Cornering

This fourth and last load case considers a cornering manoeuvre on the test vehicle. The test is performed at a slowly increasing driving speed from 35 km/h to 60 km/h whilst a constant cornering radius of approximately 50 m is maintained. Time and quantitative results of this 100 second long experiment are presented in Figure 6.5 and Tables 6.8 and 6.9 respectively.

In line with load case 1, the *bulk deformation data-driven approach* shows a considerable thermal related bias but decent dynamic tracking of both tilting moment M_x and vertical force F_z. Furthermore, the longitudinal force F_x again shows a varying error that is attributed to crosstalk in the load reconstruction phase. All estimation errors are significant, which is well observed from the RMS error results.

The *local strain data-driven approach* results show that both moments are estimated well, with a small error on tilting moment M_x in heavily loaded conditions and a minor offset on self-aligning moment M_z. Furthermore it is observed that longitudinal force F_x and vertical force F_z become inaccurate in heavily loaded conditions. Considering a test rig calibration only and field conditions, the results are considered quite well as the RMS errors are all below 7 % FS.

The results of the *local strain model based approach* are slightly better with respect to the local strain data-driven approach. For over-turning moment M_x good results are achieved, whereas self-aligning moment M_z is slightly off in heavily cornering conditions. Longitudinal force F_x furthermore tracks the reference well, although its precision is low, especially in heavy cornering conditions. For the vertical force F_z a slight underestimation is noted.

Table 6.8: Absolute RMS errors of load case 4

Load		**Bulk data-driven**	**Local data-driven**	**Local model-driven**
Longitudinal force	F_x	697 N	366 N	366 N
Vertical force	F_z	887 N	581 N	541 N
Tilting moment	M_x	355 Nm	103 Nm	49 Nm
Self-aligning moment	M_z	40 Nm	40 Nm	32 Nm

Table 6.9: Relative RMS errors of load case 4

Load		**Bulk data-driven**	**Local data-driven**	**Local model-driven**
Longitudinal force	F_x	11.6 %	6.1 %	6.1 %
Vertical force	F_z	10.4 %	6.8 %	6.4 %
Tilting moment	M_x	12.7 %	3.7 %	1.7 %
Self-aligning moment	M_z	6.7 %	6.7 %	5.3 %

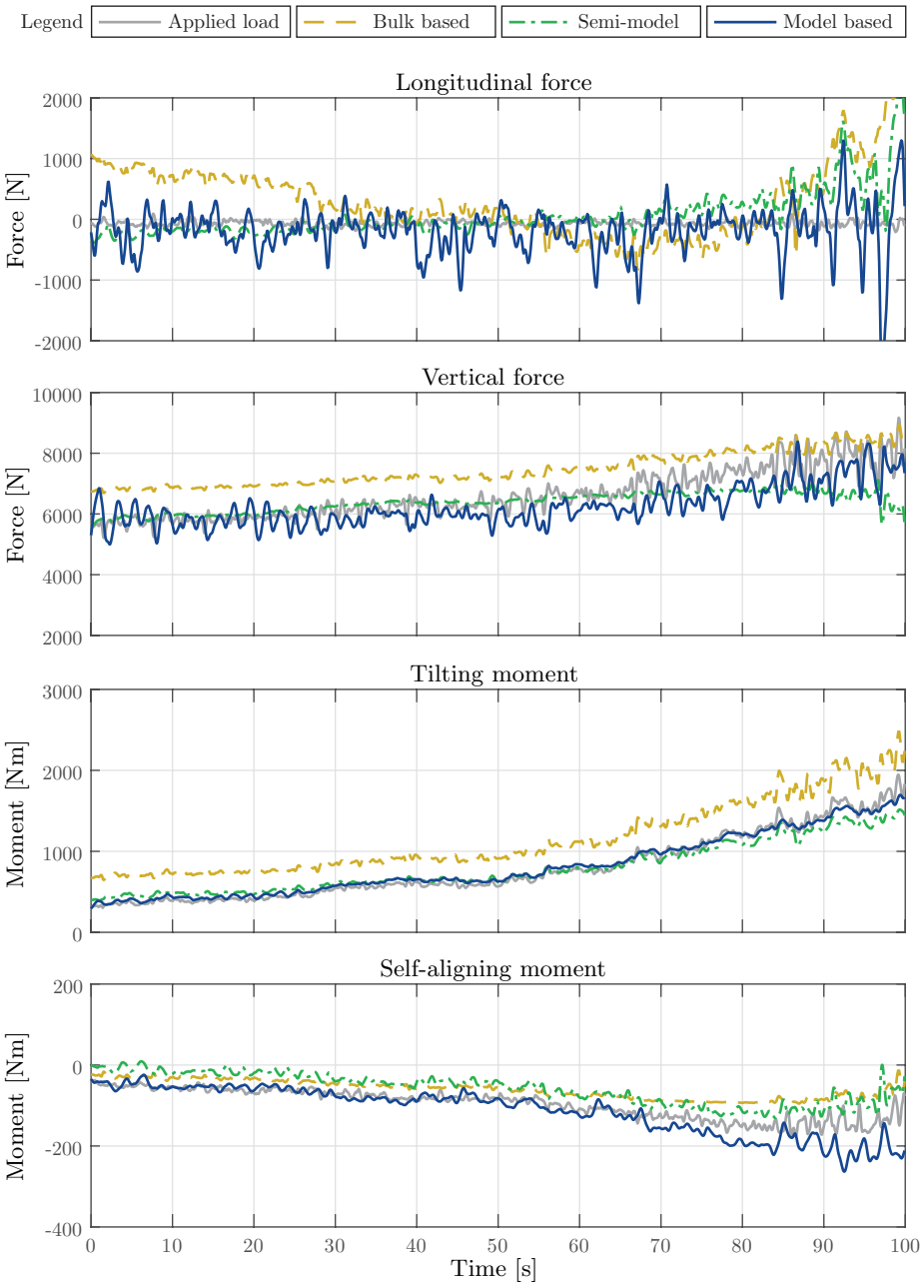

Figure 6.5: Time domain results of load case 4 performed on the test vehicle

6.4 Discussion

Before the in-depth discussion of each of the load reconstruction algorithms, first several general aspects that affect any deformation based load estimation algorithm must be noted.

Although only a limited amount of load cases are presented in the previous, the results are reflective for the vast amount of experiments performed during this thesis. All load cases have been tested multiple times to assess repeatability and it was found that results are consistent over various tests. The results therefore provide a good representation of the general performance of each approach.

Due to the small axial distance between bearing raceways the arm-length for generating moment loading by the bearing is limited. Any applied moment on the bearing therefore leads to relatively large internal rolling element loads and consequent bulk and local deformation. The higher sensitivity of the outer-ring deformation for moments than forces leads to a more accurate estimation of moments, which is well observed when comparing their absolute RMS errors. As the FS excitation ranges vary considerably between each considered load, relative results show slightly different results. Self-aligning moment M_z in particular shows large relative RMS errors due to its very limited FS range.

The main challenge in the load calculation phase is related to representing the non-linear behaviour of the internal rolling element load distribution. As extended in Chapter 2 this load distribution is dependent on the combined bearing loading and heavily affected by outer-ring flexibility. Due to its dependency on the combination of all 5 bearing loads any individual bearing load can be reflected by different rolling element load distributions. As the strain measurement locations furthermore are fixed, each of these locations has a varying sensitivity to any individual loading depending on the combined bearing load. This non-linear effect is the root cause for the observed errors on longitudinal force F_x for the coefficient based load estimation. Next to that it leads to the varying and bearing load dependent precision that is best observed for the longitudinal force estimate F_x of the full-model based approach.

An important factor affecting the estimation results is the rotation of the bearing in the laboratory setup due to flexibility arising from the inclusion of the steering knuckle as discussed in the experimental setup Section 5.2. Although the effect is limited, it does lead to crosstalk for both force and moment estimates due to misalignment of the bearing and reference coordinate systems. Due to different dependency on calibration, the data-driven and model based load calculation stage react differently to this issue. As the calibration of the data-driven calculation phase can implicitly account for the rotational effect in coefficient matrix β, it is hardly noticed in the laboratory experiments of both data-driven approaches. However, when switching to field conditions, this implicit compensation may lead to erroneous estimates as observed for longitudinal force estimate F_x of both approaches.

Due to the limited dependency on calibration of the model based approach, it in contradiction does not compensate for this misalignment. In laboratory conditions this is well observed in load case 1 for the self-aligning moment estimate M_z.

6.4.1 Bulk deformation data-driven approach

The results of the *bulk deformation data-driven approach* show decent dynamic tracking of all estimates for the road realistic load cases although considerable biases due to thermal drift are noted. The decent tracking of dynamic behaviour shows that indeed the bulk deformation is informative for reconstruction of the bearing loading. However, even with regular recalibration of thermal coefficient vector ζ (every 5 minutes for test rig experiments) the thermal influence on the bulk deformation measure in most experiments is significant, which reflects the relatively large magnitude and short time-constant of the thermal effect on the bulk deformation.

From the observed biases it is noted that especially vertical force F_z and tilting moment M_x are prone to thermal drift, whilst longitudinal force F_x and self-aligning moment M_z are apparently less affected. As F_z and M_x share correlation to the top and bottom strain gauges, whereas F_x and M_z are most strongly correlated to the front and rear strain measurement, this difference can be explained by the uneven thermal bulk deformation of the bearing outer-ring. Regardless of the exact cause, thermal effects lead to an unacceptable low reproducibility of absolute load estimates when the bulk deformation is considered. It can be noted however, that dynamic tracking remains good even when significant thermal bias is present.

When omitting the thermal induced errors and focusing on the coefficient based load calculation phase, one can observe that decent load estimates are achieved as long as the estimation region is close to the calibration domain. The erroneous longitudinal force estimate F_x during load case 1 is attributed to the previously discussed non-linear rolling element behaviour that is not accurately captured by the coefficient based load calculation phase. The underestimation of tilting moment M_x in load case 2 is attributed to an additional non-linearity as a result of the lumping of in- and outboard deformation. The alternative load case 3 shows that estimation outside the calibration bounds leads to large estimation errors. It shows the limited description and lack of predictive qualities that the coefficient based calculation phase provides.

The field experiment results show similar thermal biases as the laboratory tests, as well as the decent dynamic tracking of vertical force F_z and tilting moment M_x. Longitudinal force estimate F_x on the other hand behaves different and highly erroneous. The latter is explained by the previously discussed test-rig rotation and calibration. Furthermore, bearing rotation due to suspension travel as well as differences in boundary conditions of the laboratory and field setup might affect

the estimation quality. The significance of each contribution however cannot be addressed based on the current study.

6.4.2 Local strain data-driven approach

The *local strain data-driven approach* shows no notable estimation biases and at the same time decent tracking of load dynamics throughout all road realistic load cases. This confirms the invariance of the local strain to thermal effects and shows the effective extraction of the local strain amplitude by the model based conditioning approach.

As the model based conditioning approach estimates both in- and outboard strain contributions from the lumped measurement, more information is extracted from the instrumented bearing than by conditioning of the lumped bulk deformation. The input dimensionality to the coefficient based load calculation therefore increases, allowing for a more accurate reconstruction of the bearing loading. The latter is noted by the improved tilting moment estimate M_x in the slalom load case. However, in line with the bulk deformation based approach, notable errors are observed for longitudinal force estimate F_x during load case 1. The latter is a result of the previously discussed non-linear bearing behaviour, that in particular is noted for combined loading situations. From the alternative load case it is furthermore observed that, although the input dimensionality has increased, the coefficient based load calculation phase is unable to provide decent load estimates outside the calibration domain. It is apparent that, even with a considerably increased dimensionality of the input, the load calculation method lacks predictive qualities for the non-linear strain-to-load relationship.

The field test results by the semi-model based approach are decent as the tilting moment M_x is well estimated whilst the self-aligning moment is only slightly underestimated. Longitudinal force F_x and vertical force F_z are initially estimated well but become erroneous when overall bearing loading increases. The latter is most probably related to the test-rig calibration that includes flexibility and rotation which is not noted during field testing. As discussed, especially in heavily loaded conditions a misalignment of the bearing and test-rig was observed which is implicitly accounted for in coefficient matrix β. It is inevitable that this then affects estimation in different (non-affected) conditions. Furthermore, differences in both test setups and suspension related bearing rotation will negatively affect results.

6.4.3 Local strain model based approach

The *local strain model based approach* leads to unbiased estimates with good dynamic tracking during all road realistic load cases, although considerable errors are noted during the switching of moment direction in load case 2. Furthermore, in

contradiction to previous approaches, longitudinal force estimate F_x in load case 1 is well estimated and estimation results for the alternative load case are relatively good.

The errors noted during switching of moment direction originate from the conditioning phase of the algorithm. Due to the relatively low loading and consequent bearing deformation in these switching conditions, limited information is obtained from the strain measurement whilst at the same time states are changing quickly. The strain model EKF therefore has difficulties in discriminating the super-positioned in/outboard rolling element loads that transfer rapidly. The erroneous rolling element load estimates Q_i and Q_o result in an incorrect estimation of the bearing state and bearing loading. After moment switching, when bearing loading increases again, the EKF filter recovers due to increasing signal strength. Subsequently the bearing state and load estimates recover, showing the overall robustness of the approach.

Besides the moment switching error, the observed instability on tilting moment estimate M_x during the alternative load case also originates from observability issues of the local strain EKF during a relatively low deformation state of the bearing. As the EKF covariance matrixes are tuned for the relatively higher loading conditions, the filter is too aggressive during lower deformation states which leads to the observed oscillatory behaviour. Adapting the covariance matrixes of the EKF filter during low bearing excitation would help to mitigate both switching and stability issues.

Note that, although using a similar EKF signal conditioning, the local strain data-driven approach is not notably affected by both issues. This is a result of the calibration procedure of coefficient matrix β, that minimizes the significance of the affected EKF outputs during minimization of the quadratic errors.

Omitting the difficulties in low-excitation states due to signal conditioning, it is noted that the model based load reconstruction phase leads to better results than the coefficient based methodology. Due to the model based description of the nonlinear bearing behaviour, longitudinal force F_x during load case 1 is estimated accurately. The model based approach furthermore leads to a good description of the alternative load case which is reflected by the good tracking performance and minor bias on vertical force F_z. The good reflection of the strain-to-load relationship, even outside of the calibration domain, is a result of the applied modelling that is used to define principal relationships. Calibration in this approach only serves to define the strain gauge sensitivity, and therefore has a limited effect on the overall load calculation. Although this is advantageous when the model and test setup align well, it is less flexible in correcting minor errors like the noted test rig flexibility and rotation. This latter is well reflected by the noted crosstalk in self-aligning moment M_z in load case 1 that, in contradiction to both coefficient based approaches, is not implicitly corrected for by calibration.

The full-model based approach performs good in field conditions. Tilting mo-

ment M_x is estimated accurately, whilst self-aligning moment M_z is over-estimated in heavily loaded conditions. Vertical force F_z is slightly underestimated and both forces are considerably less precise than during laboratory experiments. The minor errors observed are not related to any specific cause as different aspects like the rotational errors, differences between both test setups and increased noise levels on the field setup probably all have limited contributions.

6.5 Conclusion

This Chapter presents an experimental validadation in both laboratory and field conditions for the developed load reconstruction algorithms. Due to the stage-wise differences between the algorithms the experimental study allows for an extensive analysis of the proposed conditioning and load reconstruction methodologies.

With respect to signal conditioning, a bulk deformation and local strain model based approach are evaluated. The results show that the local strain model based approach performs better, in particular due to its invariance to thermal effects. Although the observed gain is strongly case specific often improvements of over 5 percentage points of FS can be noted. Furthermore by the use of this method more information is extracted from the instrumented bearing as in- and outboard contributions are separated. The output dimensionality therefore increases which is advantageous for the subsequent load calculation phase.

Both a data-driven and model based load reconstruction phase are applied and compared. In combination with conditioning of local strain, the coefficient based approach leads to decent load estimates when loading is within the calibration domain. Difficulties arise when combined loading is considered, as the coefficient based approach cannot capture the complex non-linear strain-to-load relationship. Furthermore, large errors result when the applied loading exceed the calibration domain as the coefficient based approach has limited predictive qualities.

By capturing the bearing non-linear behaviour by modelling, the model based load reconstruction approach leads to better results than the coefficient based approach. In the combined loading test case an improvement of over 5 percentage points is observed for the radial longitudinal force F_x. However, other load estimates for load cases within the calibration domain show variable results as the model based approach is more heavily affected by inaccuracy in conditioning and test-rig alignment due to the limited correction capabilities of calibration. For load cases outside of the calibration domain however, the model based approach provides a clear improvement with an accuracy increase ranging from 6.8 percentage points for tilting moment M_x to 18.4 percentage points for self-aligning moment M_z. The latter is a significant improvement with respect to a fitting based approach, and shows that the approach is much better capable of handling unknown situations.

The improved results observed for load conditions outside of the calibration do-

main can be attributed to the information and relationships that are contained within the physical model. As important behaviour is defined by modelling the chances of overfitting are reduced and the algorithm's functional domain is extended. The model knowledge that is introduced helps to improve the calibration routine as less data is required whilst a larger domain can be mapped accurately. The latter is a valuable improvement, in particular when considering commercialization of the approach.

The performance in field conditions is decent for both of the methods applied. For the cornering test case the data-driven and model-driven load calculation approaches provide similar performance. The main difficulties that are observed are attributed to bearing rotation resulting in crosstalk between load estimates. As the latter is related to the experimental setup, the transfer from laboratory to field experiments shows no difficulties for the proposed load reconstruction methodologies and their calibration. It is promising to observe that the test rig calibration performs well during field experiments, as this is logically an important aspect for future commercialization of the approach.

Chapter 7

Anti-Lock Braking Application Study

To study the advantages of bearing load reconstruction for automotive applications, in this Chapter a load-based anti-lock braking algorithm is developed and tested. A novel method of wheel slip control based on load information is presented, and subsequently this approach is implemented in a load-based anti-lock braking control algorithm. Due to the usage of wheel load information, traditional kinematic-based difficulties such as velocity estimation and slip threshold determination are circumvented. Additionally, the effects of road friction fluctuations and brake efficiency are minimized. The approach is experimentally validated on the test vehicle, presenting both the load estimation accuracy and bandwidth of the bulk deformation-based load reconstruction approach, as well as the potential of wheel load information for vehicle dynamic control purposes.

S. Kerst, B. Shyrokau and E. Holweg. "Anti-lock braking control based on bearing load sensing", *Proc. of EuroBrake 2015, Dresden, Germany (2015): 4-6*. [42]

7.1 Introduction

Nowadays the anti-lock braking system is a mandatory active safety system in road vehicles. Its primary function is to prevent wheel lock during heavy braking to guarantee brake performance while simultaneously maintaining vehicle steerability and stability. Although research activities in ABS have been started many years ago, new approaches are continuously being developed and discussed in the automotive research society.

The diversity of the applied control methods in ABS design ranges from bang-bang control up to modern control techniques like model predictive control, iterative learning and others [2, 35]. It should be noted that in literature the investigation of novel ABS control algorithms is often limited by idealistic conditions such as a quarter-car model, homogeneous road friction, simplification of brake system dynamics and other significant assumptions. In industrial realizations, ABS controllers are typically based on a complex set of heuristic rules based on both wheel slip and deceleration. Although this approach dominates in industry, its application requires extra effort to solve well known problems that arise in wheel slip control based on a standard set of vehicle sensors. This includes reference velocity estimation, slip threshold determination and adaptation and functionality at low vehicle speeds.

From a control perspective a force based approach has more potential compared to a kinematic approach. Usage of tire forces allows for the design of less complex algorithms whilst robustness to changing conditions is maintained and performance can be enhanced [15, 76]. Estimation techniques or direct/indirect measurement approaches can be used to obtain the control variables. The first approach can be based on a standard set of vehicle sensors; however, it requires a precise system model in real-time causing high computational costs [78]. Methods for direct / indirect wheel force estimation include: tire sidewall or suspension bushing deformation [89], wheel rim strain measurements [30], tire inner liner accelerometer based measurements [12] and a bearing deformation based approach [59]. However, most of these approaches will not offer sufficient bandwidth on the force estimation at the highly nonlinear operation region of ABS.

In this Chapter a novel wheel load based ABS algorithm is presented and tested. The ABS algorithm uses only wheel loads as control variables, in contrast to [7, 15, 19], such to avoid the usage of extra sensors and estimators. Furthermore, whilst other literature uses more idealistic laboratory conditions as a tire test rig [7, 19] or a HIL test bench without rotating parts [7], in this study on-road experiments are carried out. The functionality of the algorithm as well as the quality of wheel load estimation using a bearing bulk deformation based approach is investigated and discussed.

7.2 Wheel corner dynamics

For the development of wheel load based slip derivative control first the quarter car dynamics need to be described. As depicted in Figure 7.1, wheel dynamics can be described by:

$$J\dot{\omega} = r_w F_x - T_b \tag{7.1}$$

where $\dot{\omega}$ is the angular acceleration of the wheel, F_x is the longitudinal tire force, T_b is the brake torque, J is the moment of inertia of the wheel and r_w is dynamic tire radius. The brake torque is generated through the tangential force at the effective radius of the brake as follows:

$$T_b = r_b F_{TD} \tag{7.2}$$

where F_{TD} is the tangential force and r_b is the effective friction radius. The tangential force itself is generated by the application of brake pressure to the calliper, this relation is described by:

$$F_{TD} = 2\mu_b P_b A \tag{7.3}$$

where P_b is the brake pressure at the brake calliper, A is the brake cylinder area and μ_b is the friction coefficient between brake pad and disc. During the braking process the friction coefficient may change due to changes in contact pressure, temperature and velocity.

The longitudinal tire force F_x in (7.1) depends on numerous factors including wheel slip, road surface conditions, tire pressure, wheel loading and tire wear. For straight driving this longitudinal force can be approximated as:

$$F_x = F_z \mu(\lambda, \vartheta) \tag{7.4}$$

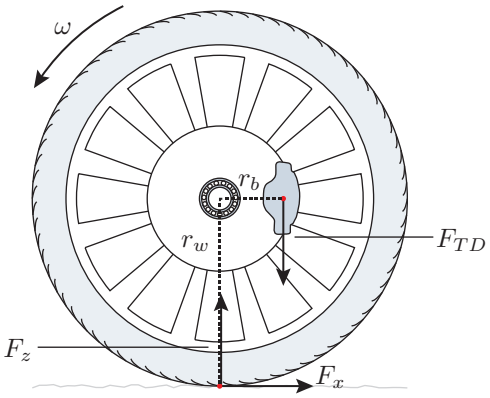

Figure 7.1: Wheel corner model

where F_z is the normal load on the tire and μ is the road-tire friction coefficient. This latter is a non-linear function of wheel slip λ and road surface parameters ϑ. The non-linear friction coefficient is of significant interest in literature and can be described in various ways as for instance piecewise, trigonometric or exponential polynomials [71]. The road surface parameters ϑ characterize the shape of the static tire-road friction curve, whilst the wheel slip determines the actual position on the curve.

During braking, wheel slip λ is defined as:

$$\lambda = \frac{v - r_w\omega}{v} \quad , \quad \lambda \in [0, 1] \tag{7.5}$$

where v represents the vehicle speed and ω is the rotational speed of the wheel.

The longitudinal vehicle dynamics, after neglecting aerodynamic drag, rolling resistance and forces due to road gradients, can be described by:

$$\dot{v} = -\frac{1}{m}\sum_{i=1}^{4} F_{x,i} \tag{7.6}$$

where m is the vehicle total mass and the sub-indexes i of the longitudinal force indicate the four individual wheels.

7.3 Load based wheel slip derivative control

The algorithm proposed in this Chapter is based on control of the wheel slip derivative using wheel load measurements F_x and T_b. The following will present the main theory on which the algorithm relies. As focus lies on pure load based wheel slip control, wheel and vehicle speeds and accelerations are assumed to be unknown.

First consider the wheel slip derivative, which is obtained by time derivation of (7.5):

$$\dot{\lambda} = \frac{r_w\omega}{v^2}\dot{v} - \frac{r_w}{v}\dot{\omega} \tag{7.7}$$

Note that wheel slip control is represented by control of the left hand side (LHS) of this equation. The right hand side (RHS) of the equation contains unknown vehicle and wheel speeds and accelerations. Now by substituting $\dot{\omega}$ using (7.1), $\dot{v}$ using (7.6) and multiplying both left and right hand side by v, one obtains:

$$v\dot{\lambda} = -\frac{r_w\omega}{v}\frac{1}{m}\sum_{i=1}^{4} F_{x,i} - \frac{r_w}{J}(r_w F_x - T_b) \tag{7.8}$$

During the situation currently under consideration v is always positive definite,

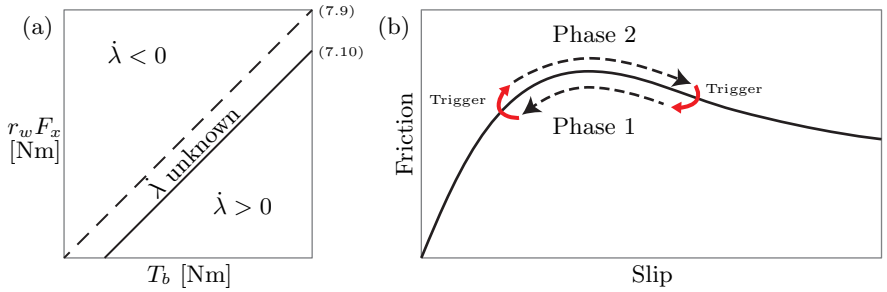

Figure 7.2: (a) Visualisation of boundary conditions provided by (7.9) and (7.10) (b) Overview of intended algorithm behaviour in the slip-friction plane

and thus the RHS is indicative for the sign of $\dot{\lambda}$. The RHS can be closely approximated using wheel load measurements F_x and T_b, as will be shown in the following.

The first term in the RHS of (7.8), which is the influence of vehicle deceleration on the wheel slip derivative, consists of a vehicle deceleration part, $-1/m \sum_{i=1}^{4} F_{x,i}$, and a vehicle to wheel speed relational term, $(r_w \omega)/v$. The former term can be closely approximated by the use of the longitudinal force measurements on all wheels and an on-line estimation of the vehicle mass. The wheel speed relational term on the other hand is unknown. However, its bounds can be easily found to be $\in [0, 1]$ as the minimum wheel speed is zero, whilst the maximum while braking is limited by the vehicle speed.

The second RHS term in (7.8) is governed by the measured loads, wheel inertia J and the dynamic tire radius r_w. In this work, wheel inertia and dynamic tire radius are assumed to be constant and known.

Note that the complete RHS of (7.8) can thus be on-line approximated by load measurements, known boundary values and assumed known parameters. It is therefore possible to define conditions that guarantee a decreasing or increasing wheel slip as follows:

$$\text{IF} \quad T_b - r_w F_x < 0 \qquad \Rightarrow \dot{\lambda} < 0 \tag{7.9}$$

$$\text{IF} \quad T_b - r_w F_x > \frac{J}{r_w} \frac{1}{m} \sum_{i=1}^{4} F_{x,i} \qquad \Rightarrow \dot{\lambda} > 0 \tag{7.10}$$

As the wheel-vehicle speed relation is unknown, a small region remains in which the slip derivative cannot be determined. This is visualized in Figure 7.2 (a), where the boundary conditions of (7.9) and (7.10) are presented by a dotted and solid line respectively. The $\dot{\lambda}$ region of uncertainty, which can be avoided by a

proper control action, is described by:

$$0 \geq T_b - r_w F_x \leq \frac{J}{r_w}\frac{1}{m}\sum_{i=1}^{4} F_{x,i} \quad \Rightarrow \dot{\lambda} \text{ unknown} \tag{7.11}$$

Note that as road surface conditions, tire conditions and vertical loading are not within the formulations the methodology is invariant to their states.

7.4 Proposed anti-lock braking algorithm

The proposed algorithm is a two-phase hybrid controller which ensures a wheel slip limit cycle near the peak of the friction curve. The cyclic behaviour is obtained by the use of two opposing phases: phase 1 ensures a decreasing wheel slip value and phase 2 guarantees an increasing wheel slip. A longitudinal force based mechanism is employed to trigger phase switching. This all results in the cyclic behaviour as depicted in Figure 7.2 (b).

Phase 2 and the triggering mechanism both make use of the maximum longitudinal force encountered within each phase, which is defined as:

$$\hat{F}_{max}(t) = \max_{t_s \leq \tau \leq t}(F_x(\tau)) \tag{7.12}$$

where $\hat{F}_{max}$ is the maximum in-phase longitudinal force, t is the current time and t_s is the phase start time. As can be deduced from its definition, the maximum in-phase longitudinal force is reset upon entering a new phase.

7.4.1 Phase 1 – decreasing wheel slip

This phase is initialized when the wheel slip is at the unstable right side of the friction peak, and its goal is to return the wheel slip to the stable left side of the friction peak. By doing so, it will increase the road-tire friction. In the proposed algorithm, this is accomplished by ensuring a continuous decrease of wheel slip by setting a brake torque T_b based on the state space boundary condition presented in (7.9).

As a specific control action is required, it is chosen to offset the boundary condition by an offset parameter. This offset parameter additionally provides robustness to measurement uncertainties and noise. The following brake torque control law is proposed:

$$T_b(t) = r_w F_x(t) - \Delta T_b^- \tag{7.13}$$

where $\Delta T_b^- \in \langle 0, \infty]$, is the offset parameter. The proposed control law will guarantee a decreasing wheel slip for all road-tire friction conditions.

7.4.2 Phase 2 – increasing wheel slip

After the return to the stable left side of the friction peak in phase 1, this phase aims to increase road-tire friction by increasing wheel slip using the state space boundary conditions for brake torque T_b proposed in (7.10).

In line with phase 1, an offset parameter is introduced to generate a specific brake torque control action. Besides providing robustness to measurement uncertainties and noise this offset also allows the algorithm to cope with upward changes of the friction peak. Furthermore, in order to optimize the initial brake torque setting, the maximum longitudinal force encountered in the previous phase is used as reference in the initial setting of brake torque. This results in the following control law:

$$T_b(t) = \frac{J}{r_w}\frac{1}{m}\sum_{i=1}^{4} F_{x,i} + r_w \max(\hat{F}_{sp}, \hat{F}_{max}(t)) + \Delta T_b^+ \tag{7.14}$$

where $\Delta T_b^+, \in \langle 0, \infty]$ is the offset parameter and $\hat{F}_{sp}$ is the longitudinal force set point value. On phase entering the longitudinal force set point value is set such that it contains a scaled value of previous phase's encountered maximum longitudinal force:

$$\hat{F}_{sp} = \alpha_F \hat{F}_{max}(t) \tag{7.15}$$

where α_F is the longitudinal force scaling parameter which is applied to improve algorithm cycling. The control law is able to cope with changes in friction curve characteristics of both increasing as decreasing friction peak. The decreasing peak is handled as the $\hat{F}_{max}$ setting is reset every phase. The usage of the combination of $\hat{F}_{max}$ and ΔT_b^+ allows for handling of an increasing friction peak, as the brake torque setting is set higher than the estimate of the maximum longitudinal force.

7.4.3 Phase triggering mechanism

When slip boundary conditions of either phase 1 or 2 are satisfied the longitudinal force can be used to determine whether the system is evolving towards or from the friction peak. An increasing longitudinal force represents a movement towards the friction peak while on the other hand a decreasing longitudinal force represents an evolution from the friction peak. The latter should cause a trigger to a subsequent phase.

In order to determine phase triggering, the maximum in-phase longitudinal force defined in (7.12) is used. Whenever the current measured longitudinal force has decreased more than a set amount from the maximum in-phase longitudinal force,

the next phase is triggered. This statement can be condensed to the following rule:

$$F_x(t) < \hat{F}_{max}(t) - \Delta F_{tr} \tag{7.16}$$

where ΔF_{tr} is an a priori determined force offset. This offset is set such that it both minimizes false triggering due to vertical force variations and measurement inaccuracy as well as friction curve overshoot. The longitudinal force is only indicative of the evaluation of slip with respect to the friction peak when the boundary conditions of (7.9) and (7.10) are satisfied. The mechanism is therefore only allowed to trigger phases when the system states satisfy these equations. It must furthermore be noted that this triggering mechanism only works on road surfaces with sufficient friction decrease at the unstable side of the friction peak.

7.4.4 Activation logic

Activation of the algorithm will take place when similar conditions occur as when the algorithm switches from phase 2 to phase 1. Brake torque should be such that a wheel slip is increasing, while a decrease of longitudinal wheel force is detected.

The proposed control logic is summarized in Figure 7.3.

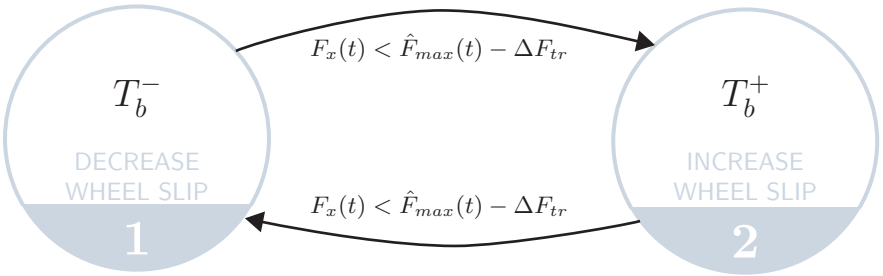

$$T_b^- = r_w F_x(t) - \Delta T_b^-$$

$$T_b^+ = \tfrac{J}{r_w}\tfrac{1}{m}\sum_{i=1}^{4} F_{x,i} + r_w \max(\hat{F}_{sp}, \hat{F}_{max}(t)) + \Delta T_b^+$$

Figure 7.3: Overview of algorithm logic

7.5 Experimental setup

For experimental validation of the proposed algorithm the BMW 5-series test vehicle with instrumented bearings as introduced in Chapter 5 is used. As the experimental testing was performed during an early stage of this thesis the first prototype version of the instrumented bearings, with six strain gauges, are used. In addition to Chapter 5 this section details some relevant details regarding the experimental setup of the application study.

7.5.1 Bearing load measurement

In this experimental application study, the *bulk deformation data-driven* algorithm is applied for load reconstruction. An in-situ vehicle calibration is applied using the method described in Chapter 4 for reconstruction of longitudinal force F_x and brake torque T_b. Although brake torque T_b acts on the rotational degree of freedom of the bearing and thus cannot be measured directly, it is estimated using the brake tangential force F_{TD} which is linearly related. The thermal offset vector ζ, applied for correcting thermal drift, is recalibrated just prior to each braking manoeuvre.

7.5.2 Brake torque control

Vehicle braking is controlled through control of the original Bosch DSC 8 hydraulic unit, by dismantling the original DSC unit and installation of a custom coil pack and power electronics. Pressure sensors are installed in the brake lines close to each brake calliper. A feedforward controller, based on a static mapping of the brake system dynamics, allows for brake pressure control at each individual wheel using the described modifications. As the relation between brake pressure and brake torque can be measured using the installed bearings, brake torque can be controlled directly via brake pressure control.

7.5.3 Test procedure

All test were performed on a single day during clear weather at the military air strip as introduced in Chapter 5. The airstrip asphalt is a high friction surface resulting in a tire-road friction coefficient with an estimated peak friction at a relatively low level of slip (approximately $\lambda = 0.06$) and a moderate drop-off at the unstable side of the peak. Figure 7.4 shows the curve fitted Burckhardt friction model based on measured data during the field test.

The test procedure consisted of accelerating the vehicle to the speed of 100 km/h and then applying heavy braking, such to cause ABS activation. Braking was only performed on the front wheels, in order to guarantee lateral stability. Over the course of different tests algorithm parameters ΔT_b^-,ΔT_b^-, ΔF_{tr} and α_{F_x}

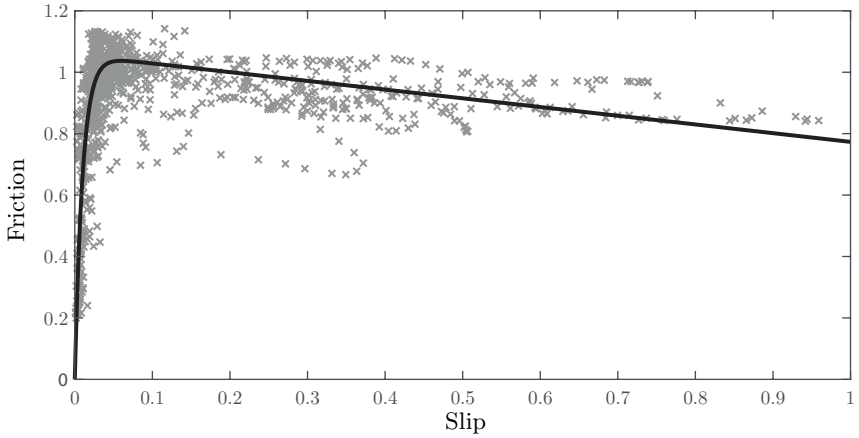

Figure 7.4: Friction curve estimate of the test track by fitting a Burckhardt model on experimental data obtained during ABS testing

were tuned in order to improve algorithm performance.

7.5.4 Algorithm modifications

As the modified DSC unit only allows for stepwise brake pressure modulation, the continuous control is translated towards discrete pressure steps. At the initiation of each phase the continuous control is sampled at 30ms, such that stepwise brake torque evaluation will result.

7.6 Experimental results

7.6.1 Reconstruction of wheel loading

In this application study, the estimation accuracy and bandwidth is important for proper functioning of the algorithm. A brief representative capture of both longitudinal force and brake torque in the time domain is shown in Figure 7.5. Phase 2 of the algorithm is triggered at $t \approx 2.33$ s, which can be clearly seen from the brake torque increase and subsequent increase of longitudinal force. It can be noted that both longitudinal force F_x and brake torque estimate T_b are close to the VELOS benchmark measurements with minimal to no delay, which reflects the estimation accuracy and bandwidth of the approach.

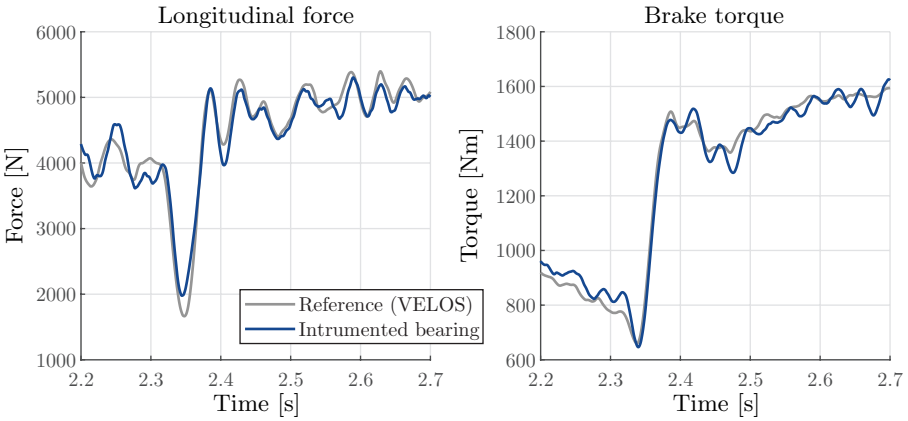

Figure 7.5: Longitudinal force and brake torque over time

The performance of the applied measurement technique is summarized in Table 7.1. It is based on 9 experiments which have an average length of 5 seconds each. Three of these experiments were used for calibration, whilst the six others are for validation. It can be seen that mean errors are minimal, whilst standard deviations are significant.

Figure 7.6 shows the power spectral density for estimation of longitudinal force F_x and brake torque T_b using the VELOS measurement rim and load-sensing bearing based on the same set of experiments as used in Table 7.1. It can be

Table 7.1: Mean error and standard deviation results

Load		Average load	**Mean error**		**Std deviation**	
Long. force	F_x	3948.9 N	10.5 N	0.27 %	278.4 N	7.05 %
Brake torque	T_b	1147.9 Nm	3.3 Nm	0.29 %	60.7 Nm	5.29 %

observed that estimation of both longitudinal force and brake torque using the load-sensing bearings is performed precisely for frequencies up to about 10 Hz. For higher frequencies noise in both estimated parameters is increased.

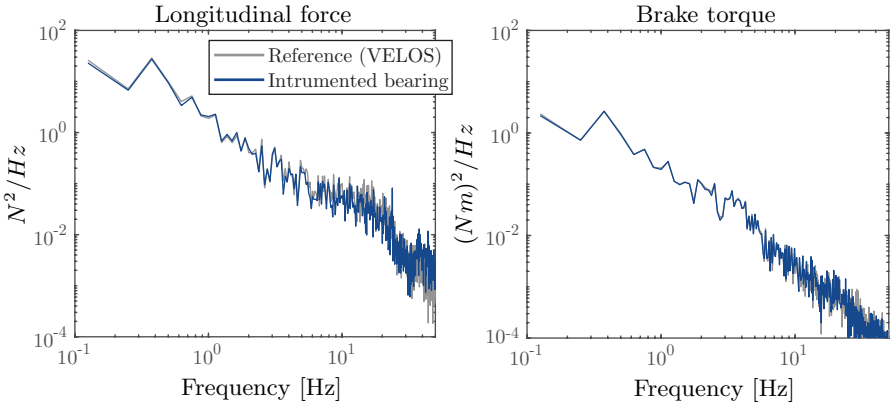

Figure 7.6: FFT of reference (VELOS) and Intrumented bearing measurements

7.6.2 Anti-lock braking algorithm

Figure 7.7 shows the wheel speed, vehicle speed and brake pressure during activation of the proposed algorithm. Five cycles of the algorithm can be observed, which avoids wheel lock from occurring.

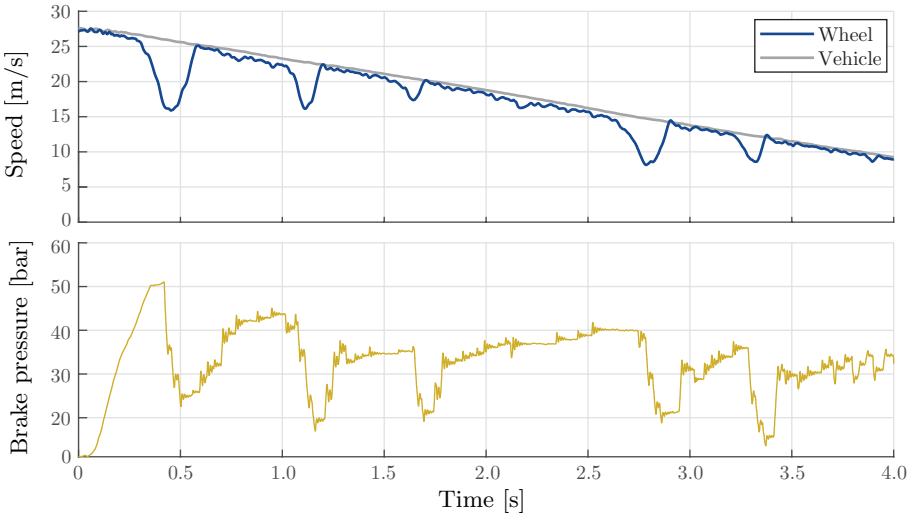

Figure 7.7: Wheel speed, vehicle speed and brake pressure over time during a load based ABS braking manoeuver

Cycling of the algorithm is slightly slower as intended as the brake pressure controller has difficulties performing small pressure increases, which are usually requested in the later stages of phase 2. This problem can be fixed by the improvement of the current approach of brake pressure control.

In Figure 7.8 the wheel slip and load-based wheel slip derivative control data of a single cycle of the proposed ABS algorithm are presented. The difference in brake torque and torque due to the longitudinal force ($T_b - r_w F_x$) is plotted in blue. The boundary conditions of (7.9) and (7.10) are represented by respectively the black dotted and black solid line. It is clearly visible that wheel slip increases when the torque difference complies to (7.10) and slip decreases when (7.9) is fulfilled.

Note that measurement errors and noise affect the torque difference ($T_b - r_w F_x$) estimate. Therefore the sign of the slip derivative might be incorrectly estimated, in particular near zero. This can be avoided by proper control settings, i.e. significantly low or high brake torque values.

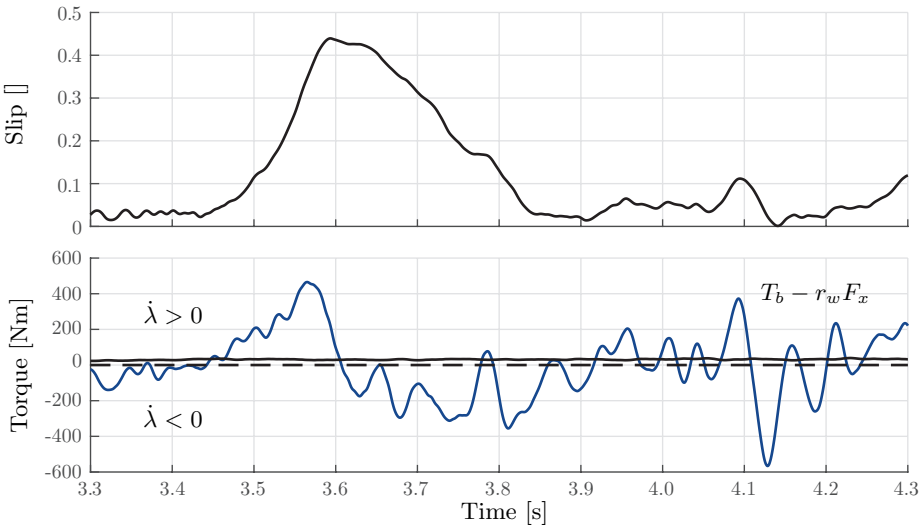

Figure 7.8: Load based wheel slip derivative control: when the torque difference is above the solid line (7.10) or below the dotted line (7.9) the wheel slip respectively increases or decreases

Figure 7.9 shows the triggering mechanism at work in phase 2 and phase 1 respectively, firing at $t \approx 6.32$ s and $t \approx 6.45$ s. The mechanism triggers a subsequent phase in line with 7.16.

The figure also shows that occasionally, as for instance during $6.35 < t < 6.45$ s, the longitudinal force is significantly influenced by other factors than changes in wheel slip and the subsequent changes of friction. The force variance is contributed to changes in vertical loading due to load transfer, road irregularities or tire unroundness. The force triggering offset ΔF_{tr} is tuned as discussed in Subsection

7.4.3 such that false triggering due to these disturbances is minimal.

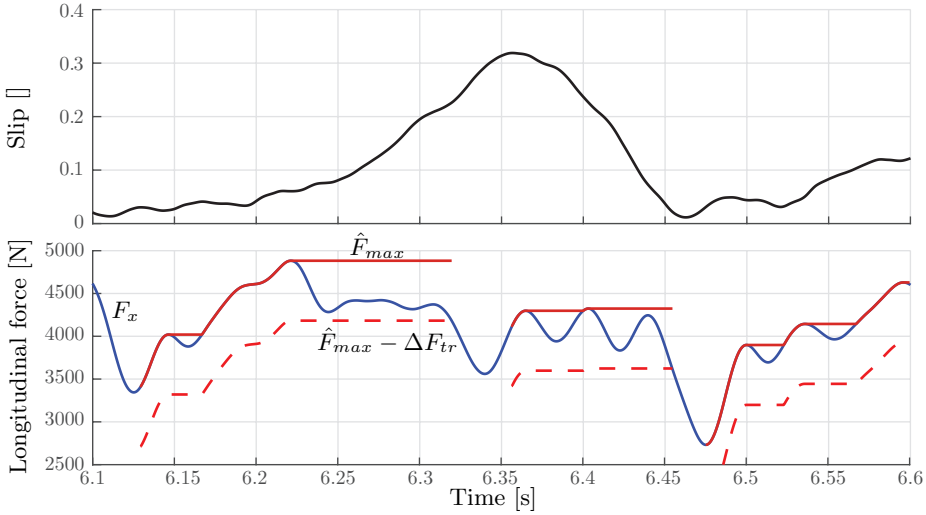

Figure 7.9: Longitudinal force based triggering mechanism over time

Future work will focus on eliminating the normal load dependency of the triggering mechanism by normalization using vertical load F_z. This latter is not implemented yet as the current load-sensing methodology does not provide sufficient accuracy and bandwidth in the normal load estimation.

A quantitative analysis of the algorithm performance remains a matter of further investigation as improvements to the brake pressure controller are required for optimal performance.

7.7 Conclusion

This Chapter presents a method to control the wheel slip derivative based on wheel load information. Based on this slip control methodology a novel two phase ABS algorithm with a force based phase switching mechanism is developed. Due to the usage of wheel loads, available by this thesis' developed bearing load reconstruction methodology, traditional ABS difficulties like velocity estimation and slip threshold determination and adaptation are circumvented and effects of road friction fluctuations and brake efficiency are minimized. The performance of the load measurement methodology and the proposed ABS algorithm is investigated using the instrumented test vehicle in real road conditions. Although the variation of vertical load is still an open issue for the proposed triggering mechanism and performance is still sub-optimal, the results of the presented experimental investigations demonstrate the feasibility and advantages of wheel load information for vehicle dynamics control.

Chapter 8

Discussion and Conclusion

Bearing load measurement can serve as a valuable addition to the fields of condition monitoring and system analysis and control. Although it would be advantageous for a variety of applications, in this thesis the automotive wheel-end bearing is of specific interest; in particular since it would provide a new source of information that enables improved performance, higher robustness and less complex algorithms for dynamics control, active safety and automated driving features. The latter is reflected in several academic studies and is confirmed by the application study in this thesis. However, an accurate, robust and cost-effective approach for the measurement of bearing loading is not available up to this date. This may be caused by several technical challenges in signal conditioning, load calculation and calibration effort of the (data-driven) state-of-the-art. In order to address these issues, the following research objective is defined for this thesis:

To develop a generally valid bearing load reconstruction approach for the estimation of all relevant bearing loads while limiting the number of parameters subject to calibration

To meet this objective, a simulation and experiment-based study is performed. First, the state-of-the-art is reproduced in order to assess its limitations and analyse bearing behaviour in detail. Based on these findings, a novel physics-based approach is proposed and developed. This includes the development of a novel bearing strain and bearing load model, as well as their implementation in a cascaded Kalman filter based load estimation approach. The reconstruction algorithm is validated in both laboratory and field conditions. Finally, an application study shows the potential benefits of bearing load measurement for vehicle dynamics control.

8.1 Reflection on the state-of-the-art

The state-of-the-art in deformation-based load reconstruction shows that two different deformation effects, bulk and local deformation, are considered for bearing load measurement. Bulk deformation is defined as the average strain during rotation and is dependent on the bulk stiffness of the bearing and its supporting structure. Local deformation on the other hand is the strain variance during bearing rotation and is found to be dependent on local geometry, material and the local rolling element loading, location and contact angle. As the physical origin of both effects differs, they require different conditioning methods, lead to different results and consequently are used in different applications.

8.1.1 On conditioning

The state-of-the-art on local strain conditioning applies peak-to-peak detection or signal power analysis to detect local bearing loading. Due to the application of basic conditioning methods, only simple load cases and single-row bearings can be considered, while at the same time signal bandwidth and accuracy are sub-optimal. Since the local strain originates from the reallocation of rolling elements, bearing rotation is a prerequisite. The experimental study shows that the local strain is invariant to thermal effects and therefore is suitable for absolute measurements.

Conditioning of the bulk deformation is achieved by low-pass filtering or specific strain gauge design to measure modal deformation. It can be applied to more complex loading conditions and is applicable to both single- and double-row bearings. The experimental study shows that thermal effects considerably bias the bulk deformation measure. As thermal correction methods have been unsuccessful in the past, the bulk deformation is deemed inapplicable for absolute load measurement.

8.1.2 On load reconstruction

Data-driven methods using regression coefficients and neural networks form the state-of-the-art in bearing load reconstruction. In this thesis, load behaviour is studied in simulation and a state-of-the-art coefficient driven approach is experimentally evaluated. It is noted that bearing load behaviour is affected by the external loading, and in particular by its dimensionality. As a consequence of this non-linearity, the coefficient-based approach results in considerable errors during combined loading conditions, whilst single DoF load cases are reconstructed accurately. Although the application of higher-order fitting or a neural network could address this non-linearity, this would inevitably lead to a large number of coefficients subject to calibration. Hence, a model-based approach for load reconstruction is presented.

8.2 Concluding discussion

8.2.1 On bearing model development

Given the aim of model-based load reconstruction, a bearing model is required that provides an accurate yet computationally low-cost relationship between bearing- and rolling element loading. As significant raceway deformation was observed during operating conditions of the considered bearing, a phenomenon that heavily affecting the element load distribution, inclusion of outer-ring flexibility is considered paramount. Due to various limitations of currently available bearing models, a novel model is developed for this specific purpose.

The proposed model is founded on traditional rigid bearing modelling theory with the addition of outer-raceway flexibility by the use of deformation shapes and a Fourier series-based compliance approximation. Additionally, a Finite Element study to determine the Fourier coefficients is presented, in order to tune the case-specific bearing outer-ring deformation behaviour.

The model is validated by a comparison study to SKF's BEAST bearing simulation software, showing that the proposed model provides accurate rolling element load estimates and contact angles for the considered bearing under various realistic operating conditions for a fraction of the computational costs. Compared to rigid bearing modelling an accuracy improvement of 60% to 80% is obtained for the various tested load cases.

8.2.2 On strain model development

For the purpose of model-based local strain conditioning, a continuous description of the local strain is necessary. Therefore, a strain model is proposed that defines the outer-ring local strain as a function of the local rolling element loading, its location and its contact angle. Although this provides a considerably simplified description of the physical behaviour, the proposed model suits the proposed approach well, since it provides a continuous description of the local strain as a function of rolling element loading, is of low computational cost and allows for modelling errors to be attenuated by calibration. Explicit model validation by simulation is not considered within the scope of this thesis, as the experimental results provide an implicit validation of the proposed model.

8.2.3 On model-based strain conditioning

The strain model is included in an Extended Kalman Filtering approach to extract local rolling element loads from local strain measurements. By including plant knowledge and continuous conditioning, the bandwidth and accuracy are improved with respect to state-of-the-art local strain conditioning approaches. Additionally, in- and outboard local strain effects are estimated independently, such

that the output dimensionality increases and traditional limitations on double row bearings are alleviated. The results furthermore show good reproducibility and invariance to thermal effects, reflecting the applicability for absolute load reconstruction. With respect to state-of-the-art bulk deformation-based conditioning, a clear improvement is achieved due to (i) invariance to thermal effects and (ii) an increased output dimensionality. The latter is reflected by an accuracy improvement of up to 5 percentage points FS for various load estimates.

8.2.4 On model-based load reconstruction

The bearing model is included in an Unscented Kalman Filter to determine the bearing loading based on the estimated rolling element loads, obtained from the novel conditioning method. Experiments show that usage of a model-based approach for load reconstruction provides numerous advantages compared to the data-driven approaches applied in the state-of-the-art. First of all, as the nonlinear bearing behaviour is explicitly captured by the bearing model, more accurate results are obtained, in particular for combined loading conditions, for which an improvement of over 5 percentage points FS is observed. Additionally, due to the definition of principal relationships by modelling, considerably better results are achieved outside of the calibration domain, as chances of overfitting are reduced. The latter is reflected by an accuracy improvement of 6.8 to 18.4 percentage points FS for the various different loads. The modelling relations furthermore lead to a decrease in the number of parameters subject to calibration with respect to the data-driven state-of-the-art. At the same time, these parameters obtain physical meaning, which could allow for more effective calibration routines.

8.2.5 On load-based anti-lock braking

To study the applicability of wheel-end load measurement, a novel approach to anti-lock braking was investigated. Based on a theoretical derivation, it is shown that by usage of wheel loads only, the wheel slip derivative can be controlled. Combined with a force-based switching mechanism, a two-phase ABS algorithm is proposed. The algorithm is tested in field conditions, showing that it acts in line with expectations and is successful in avoiding wheel lock-up.

Although performance could be enhanced by improved tuning and more sophisticated control, the successful tests show that by using wheel load information, traditional ABS difficulties like velocity estimation and slip threshold determination and adaptation can be circumvented and the effects of road friction fluctuations and brake efficiency can be minimized. Additionally, the experimental study shows that bearing load measurement can provide the signal accuracy and bandwidth required for active vehicle dynamics control. This is a promising result, as other automated vehicle and safety functions often have less strict requirements.

8.3 Recommendations

By pursuing a physics-based approach for bearing load estimation, important issues such as the limited estimation domain, errors due to thermal effects and heavy dependency on calibration that defined the research question are challenged. Thus, the feasibility of bearing load estimation for commercial purposes has increased significantly, which is reflected by the development in the wake of this thesis. However, it is clear to the author that the current solution is just one of many possibilities and contains numerous limitations. With additional research, therefore, numerous improvements could be made. The following list provides the main recommendations for further research by the author:

- Improvement of the local strain model: although the developed model allows for an effective estimation of rolling element forces based on local strain, the model could be significantly improved if varying rolling element forces over the bearing azimuth would be captured. In order to develop such model, a simulation-based study could be considered in order to independently investigate the effects of geometry, boundary conditions, strain gauge placement and rolling element location with respect to local strain.

- Improvement on the bearing load model: the bearing model provides a computationally cost-effective, robust and accurate physical description of the element forces and bearing loading. Although it runs in real-time on standard test equipment, its computational complexity could be further optimized, because the physical behaviour could be simplified. Non-linearities like the Herzian contacts could for instance be linearized, possibly without significantly affecting the model output.

- Improvement of the calibration routine: the validation study shows that with an identical calibration set, the model-based approach results in a more accurate description than the data-driven reference method. This is a consequence of the physical model, that defines several important relationships within the data, resulting in an extended estimation domain and fewer parameters subject to calibration. It would be interesting to study how the calibration routine could be optimized considering this model knowledge, in particular as the routine could possibly be shortened without loss of accuracy.

- Improvements on algorithm implementation: the current study considers a full model-based approach in a Kalman filtering implementation. For improved convergence and robustness, different filtering techniques or constraints could be applied. In particular, the practical implementation of adaptive rule-based constraints on the state variables could be beneficial.

- Bearing design for load reconstruction: apart from studies on the improvement of modelling and implementation, a considerable gain is to be expected if bearing and housing geometry would be tailored for load estimation. In particular, one could investigate a geometry to improve robustness and precision over the entire functional domain.
- Further development of anti-lock braking application: from an application perspective, numerous improvements are possible, as the study mainly proves the viability of bearing load estimation for anti-lock braking. As load information is more informative than current measurands, the author believes that more pro-active approaches could be developed, limiting the need for cycling between the stable and unstable domain.

8.4 Conclusion

By the use of a novel model-based load reconstruction algorithm, all considered bearing loads can be accurately determined for various laboratory and field experiments. Due to the usage of physical modelling, the number of parameters subject to calibration is kept at a minimum. The research objective is thereby accomplished, and the following conclusions can be drawn:

- The outer-ring local deformation is more suitable for bearing load reconstruction than the outer-ring bulk deformation.
- Model-based conditioning of local strain allows for discrimination of in- and outboard strain components and provides an improved bandwidth with respect to state-of-the-art conditioning approaches.
- A model-based approach to bearing load reconstruction leads to a more general and more robust solution, whilst requiring fewer coefficients subject to calibration.
- Bearing load measurement leads to better vehicle dynamics control, since direct access to the most important control variables allows for improved performance and robustness whilst complexity can be decreased.

Acknowledgements

Eight years have passed since my endeavour on the topic of bearing load measurement started. Initially on a one-year contract as researcher, it unfolded into a PhD study that eventually offered exciting valorisation opportunities within industry. Although by times my research might have felt as a never-ending story, especially for others, I have enjoyed every year of it as it shaped my personal interests and professional career. Nonetheless, I'm very pleased to finally conclude the work and hence it is time to thank everyone for their help. Although the act of "promoveren" is a journey into the unknown that one takes on its own, it cannot escape the fact that all in life is governed by interaction. In the following I therefore want to thank everyone that in some way provided the inspiration, opportunities, support, willpower and determination to fulfil this journey.

First I would like to show my gratitude to my initial promotor and driving force behind the idea of bearing load sensing, Edward Holweg. Your can-do mentality, insights, in-depth discussions and dedication have been both inspiring and essential to the research. I'm truly grateful for the opportunities and support you have provided to me. Then I would like to thank my current promotor, Riender Happee, which has been a positive support in my academic career ever since my Master thesis and has helped me through the last phase of my PhD. Next to your positive attitude, your perseverance helped me speed up, and your critical reviews have significantly improved the work. Lastly, of my direct academic colleagues, my biggest thanks go to my copromotor and daily supervisor Barys Shyrokau. You have been absolutely essential for my academic development as you pushed me in the right direction many times. Furthermore it was a joy working with you because of your pleasant personality and attitude. I will never forget the great times we had in office, on the test track, South-Korea and our ongoing catch-up dinners in the Bierfabriek.

Furthermore, I would like to thank Cees Slinkman for his support on the electronic hardware development for the test vehicle as well as Ben Koperdraad from SKF for the brilliant support he has provided in fabrication of the bearing prototypes. Additionally I want to thank Igor Dorrestijn, as he was an important source of inspiration during my part-time PhD era.

Next to my direct colleagues I want to thank all those that I shared office with, in particular my colleagues of the department of Precision and Microsystems Engineering, with whom I spend a great time. Although this now over four years ago,

the countless coffees, discussions, laughter, Thursday evening drinks and bitterballen and the Octoberfest are not forgotten. What a fun and inspirational time that was.

Outside of the office I have many people to thank for the abundant positive energy that has surrounded and supported me. In particular I would like to thank those that had to deal with me on a daily basis. Joep and Steffan; living with you guys definitely was an enhancing experience. And Stan; thank you for your ear and support to my emotional rants and philosophical thoughts. Furthermore I want to thank all of my other friends that cannot be named in this short two-pager. It is important not to underestimate the impact of all our encounters, laughter and discussions in the course of our lives. And therefore I'm absolutely grateful to all those that I enjoy to spend my time with.

Lastly, and most importantly, I would like to thank my family. For the last years, I more and more have realized how important you all have been, how happy I'm with the core values of life that I unconsciously have been brought up with, and how much joy I have when we are together. It certainly was the most influential support for achieving the thesis that is now in front of you. And of course you all should be named here; so Ruud & Anastasia, Yvonne & Jesse, Eric, Agnes and Cees Kerst, thank you!

Curriculum Vitæ

Stijn Kerst was born in Raamsdonk, The Netherlands, on October 25th 1986. He received his B.Sc. degree in Industrial Design Engineering and M.Sc. degree in Mechanical Engineering from Delft University of Technology in 2009 and 2012 respectively. His master thesis was on the design and implementation of a force and brake pressure based anti-lock braking system, and he continued this study on a one year appointment as researcher at Delft University of Technology. In 2013 this unfolded in a PhD study towards the development of a bearing load reconstruction algorithm. After pitching the work to various car manufacturers, interest from industry resulted in a part-time position at SKF in 2017 as product development engineer to work on the valorisation of this research. In 2019 he left SKF to later join Arrival in London as control and automation engineer. As of summer 2020 he moved back to the Netherlands to start his own company focussing on a novel approach to embedded real-time data processing.

List of Publications

Journal publications

S. Kerst, B. Shyrokau and E. Holweg. "A model-based approach for the estimation of bearing forces and moments using outer-ring deformation", *Transactions on Industrial Electronics (2019): 10.1109/TIE.2019.2897510*.

S. Kerst, B. Shyrokau and E. Holweg. "A semi-analytical bearing model considering outer race flexibility for model based bearing load monitoring", *Mechanical Systems and Signal Processing 104 (2018): 384-397*.

S. Kerst, B. Shyrokau and E. Holweg. "Reconstruction of wheel forces using an intelligent bearing", *SAE International Journal of Passenger Cars-Electronic and Electrical Systems 9.2016-01-0092 (2016): 196-203*.

Conference proceedings

S. Kerst, B. Shyrokau and E. Holweg. "Wheel force measurement for vehicle dynamics control using an intelligent bearing", *Proceedings of the 13th International Symposium on Advanced Vehicle Control (AVEC), Munich, Germany. Vol. 1316. 2016*.

S. Kerst, B. Shyrokau and E. Holweg. "Anti-lock braking control based on bearing load sensing", *Proc. of EuroBrake2015, Dresden, Germany (2015): 4-6*.

Patent application

H, Mol, E. Holweg, and S. Kerst. "Slip control system for vehicles and a vehicle provided with a slip control system." *U.S. Patent Application No. 14/891,428.*

Bibliography

[1] A. Albinsson, F. Bruzelius, M. Jonasson, and B. Jacobson. Tire force estimation utilizing wheel torque measurements and validation in simulations and experiments. In *12th International Symposium on Advanced Vehicle Control (AVEC'14), Tokyo Japan*, pages 294–299, 2014.

[2] L. Austin and D. Morrey. Recent advances in antilock braking systems and traction control systems. *Proceedings of the Institution of Mechanical Engineers, Part D: Journal of Automobile Engineering*, 214(6):625–638, 2000.

[3] M. Baeuml, F. Dobre, H. Hochmuth, M. Kraus, H. Krehmer, R. Langer, and D. Reif. The chassis of the future. In *Schaeffler Seminar*, 2014.

[4] S. Bagavathiappan, B. Lahiri, T. Saravanan, J. Philip, and T. Jayakumar. Infrared thermography for condition monitoring – a review. *Infrared Physics and Technology*, 60:35–55, 2013.

[5] A. Bourdon, J.F. Rigal, and D. Play. Static rolling bearing models in a cad environment for the study of complex mechanisms: Part i—rolling bearing model. *Journal of Tribology*, 121(2):205–214, 1999.

[6] W. Caesarendra, B. Kosasih, A. Tieu, H. Zhu, C. Moodie, and Q. Zhu. Acoustic emission-based condition monitoring methods: Review and application for low speed slew bearing. *Mechanical Systems and Signal Processing*, 72–73:134–159, 2016.

[7] D. Capra, E. Galvagno, V. Ondrak, B. Van Leeuwen, and A. Vigliani. An abs control logic based on wheel force measurement. *Vehicle system dynamics*, 50(12):1779–1796, 2012.

[8] G. Cavallaro, D. Nélias, and F. Bon. Analysis of high-speed intershaft cylindrical roller bearing with flexible rings. *Tribology transactions*, 48(2):154–164, 2005.

[9] C. Chae, B. Bae, K. Kim, J. Park, and N. Choe. A feasibility study on indirect identification of transmission forces through rubber bushing in vehicle suspension system by using vibration signals measured on links. *Vehicle System Dynamics*, 33(5):327–349, 2000.

[10] F. Cheli. Cyber tyre: A novel sensor to improve vehicle's safety. Technical Report 0148-7191, SAE Technical Paper, 2011.

[11] F. Cheli, D. Ivone, and E. Sabbioni. Smart tyre induced benefits in sideslip angle and friction coefficient estimation. In *Sensors and Instrumentation, Volume 5*, pages 73–83. Springer, 2015.

[12] F. Cheli, E. Sabbioni, M. Sbrosi, M. Brusarosco, and S. Melzi. Enhancement of abs performance through on-board estimation of the tires' response by means of smart tires. Technical Report 0148-7191, SAE Technical Paper, 2011.

[13] W. Chen, R. Mills, and R.S. Dwyer-Joyce. Direct load monitoring of rolling bearing contacts using ultrasonic time of flight. *Proc. R. Soc. A*, 471(2180):20150103, 2015.

[14] Comsol. Comsol multiphysics user's guide. *Version: September*, 10:333, 2005.

[15] M. Corno, M. Gerard, M. Verhaegen, and E. Holweg. Hybrid abs control using force measurement. *IEEE Transactions on Control Systems Technology*, 20(5):1223–1235, 2011.

[16] A. Daidié, Z. Chaib, and A. Ghosn. 3d simplified finite elements analysis of load and contact angle in a slewing ball bearing. *Journal of Mechanical Design*, 130(8):082601, 2008.

[17] H. de Azevedo, A. Araújo, and N. Bouchonneau. A review of wind turbine bearing condition monitoring: State of the art and challenges. *Renewable and Sustainable Energy Reviews*, 56:368–379, 2016.

[18] D.T.J. De Bot. A temperature state estimator for a load sensing hub bearing unit. Master's thesis, Delft University of Technology, 2009.

[19] E. de Bruijn, M. Gerard, M. Corno, M. Verhaegen, and E. Holweg. On the performance increase of wheel deceleration control through force sensing. In *2010 IEEE International Conference on Control Applications*, pages 161–166. IEEE, 2010.

[20] J. de Mul, J. Vree, and D. Maas. Equilibrium and associated load distribution in ball and roller bearings loaded in five degrees of freedom while neglecting friction—part i: General theory and application to ball bearings. *Journal of Tribology*, 111(1):142–148, 1989.

[21] C. Defaye, D. Nélias, A. Leblanc, and F. Bon. Theoretical analysis of high-speed cylindrical roller bearing with flexible rings mounted in a squeeze film damper. *Tribology Transactions*, 51(6):762–770, 2008.

[22] J.A. Den Engelse. Estimation of the lateral force, acting at the tire contact patch of a vehicle wheel, using a hub bearing unit instrumented with strain gauges and eddy-current sensors. Master's thesis, Delft University of Technology, 2013.

[23] B. Dolenc, P. Boskoski, and D. Juricic. Distributed bearing fault diagnosis based on vibration analysis. *Mechanical Systems and Signal Processing*, 66–67:521–532, 2016.

[24] I. El-Thalji and E. Jantunen. A summary of fault modelling and predictive health monitoring of rolling element bearings. *Mechanical Systems and Signal Processing*, 60–61:252–272, 2015.

[25] S. Ericsson, N. Grip, E. Johansson, L. Persson, R. Sjöberg, and J. Strömberg. Towards automatic detection of local bearing defects in rotating machines. *Mechanical Systems and Signal Processing*, 19(3):509–535, 2005.

[26] J. Fiszer, T. Tamarozzi, B. Blockmans, and W. Desmet. A time-dependent parametric model order reduction technique for modelling indirect bearing force measurements. *Mechanism and Machine Theory*, 83:152–174, 2015.

[27] Y. Furukawa and M. Abe. Advanced chassis control systems for vehicle handling and active safety. *Vehicle System Dynamics*, 28(2-3):59–86, 1997.

[28] D. Garcia-Pozuelo, O. Olatunbosun, S. Strano, and M. Terzo. A real-time physical model for strain-based intelligent tires. *Sensors and Actuators A: Physical*, 2019.

[29] M. Gerard. *Global chassis control and braking control using tyre forces measurement.* PhD thesis, PhD thesis, Delft University of Technology, 2011.

[30] M. Gobbi, J. Botero, and G. Mastinu. Global chassis control by sensing forces/moments at the wheels. *International Journal of Vehicle Autonomous Systems*, 7(3-4):221–242, 2009.

[31] J. Goos, A. P. Teerhuis, A. J. C. Schmeitz, I. Besselink, and H. Nijmeijer. Model-based state estimator for an intelligent tire. In *13th International Symposium on Advanced Vehicle Control (AVEC 2016)*, pages 503–508. CRC Press/Balkema, 2017.

[32] H. Grunbaum. Arrangement for measuring a radial force applied to a bearing. U.S. Patent No. 4,112,751, 1978.

[33] T. Harris. *Rolling bearing analysis.* John Wiley and sons, 2001.

[34] ISO. 15243: 2004 rolling bearings—damage and failures—terms, characteristics and causes, 2004.

[35] V. Ivanov, D. Savitski, and B. Shyrokau. A survey of traction control and antilock braking systems of full electric vehicles with individually controlled electric motors. *IEEE Transactions on Vehicular Technology*, 64(9):3878–3896, 2014.

[36] K. Iyer, B. Shyrokau, and V. Ivanov. Offline and online tyre model reconstruction by locally weighted projection regression. *IEEE International Workshop on Advanced Motion Control*, Norway, 2020.

[37] A. Jayashankar. Experimental & modeling study of the influence of support stiffness on load sensing bearings. Master's thesis, Delft University of Technology, 2011.

[38] C. H. Jeong, J. Y. Kim, and D. H. Jung. Research on vehicle stability technology based on wheel force. *International Journal of Automotive Technology*, 16(3):435–445, 2015.

[39] A.B. Jones. A general theory for elastically constrained ball and radial roller bearings under arbitrary load and speed conditions. *ASME J. Basic Eng*, 82(21):309–320, 1960.

[40] S. J. Julier and J. K. Uhlmann. New extension of the kalman filter to nonlinear systems. In *Signal processing, sensor fusion, and target recognition VI*, volume 3068, pages 182–193. International Society for Optics and Photonics, 1997.

[41] R. E. Kalman. A new approach to linear filtering and prediction problems. 1960.

[42] S. Kerst, B. Shyrokau, and E. Holweg. Anti-lock braking control based on bearing load sensing. In *EuroBrake*, pages 4–10, Dresden, Germany, 2015.

[43] S. Kerst, B. Shyrokau, and E. Holweg. Reconstruction of wheel forces using an intelligent bearing. *SAE International Journal of Passenger Cars-Electronic and Electrical Systems*, 9(2016-01-0092):196–203, 2016.

[44] S. Kerst, B. Shyrokau, and E. Holweg. Wheel force measurement for vehicle dynamics control using an intelligent bearing. In *Advanced Vehicle Control*, pages 547–552, 2016.

[45] S. Kerst, B. Shyrokau, and E. Holweg. A semi-analytical bearing model considering outer race flexibility for model based bearing load monitoring. *Mechanical Systems and Signal Processing*, 104:384–397, 2018.

[46] S. Kerst, B. Shyrokau, and E. Holweg. A model-based approach for the estimation of bearing forces and moments using outer ring deformation. *IEEE Transactions on Industrial Electronics*, 67(1):461–470, 2019.

[47] M. Kraus and M. Bäuml. Continuous wheel force measurement for passenger vehicles and commercial vehicles. In *6th International Munich Chassis Symposium*, pages 717–717, Munich, Germany, 2015. Springer.

[48] S. Lacroix, D. Nélias, and A. Leblanc. Four-point contact ball bearing model with deformable rings. *Journal of Tribology*, 135(3):031402, 2013.

[49] A. Leblanc, D. Nélias, and C. Defaye. Nonlinear dynamic analysis of cylindrical roller bearing with flexible rings. *Journal of Sound and Vibration*, 325(1):145–160, 2009.

[50] G.B. Lechler. Apparatus for measuring bearing forces. U.S. Patent No. 4,203,319, 1980.

[51] H. Lee and S. Taheri. Intelligent tires? a review of tire characterization literature. *IEEE Intelligent Transportation Systems Magazine*, 9(2):114–135, 2017.

[52] J. Lee, F. Wu, W. Zhao, M. Ghaffari, L. Liao, and D. Siegel. Prognostics and health management design for rotary machinery systems—reviews, methodology and applications. *Mechanical Systems and Signal Processing*, 42(1–2):314–334, 2014.

[53] B. Leeuwen and J. Zuurbier. Vehicle state estimation based on load sensing. In *Vehicle Dynamics Expo*, 2007.

[54] G. Lim, Y. Ali, and B. Yang. The fault diagnosis and monitoring of rotating machines by thermography. In *Engineering Asset Management and Infrastructure Sustainability: Proceedings of the 5th World Congress on Engineering Asset Management*, pages 557–565. Springer London, London, 2012.

[55] T. Liu and J. Mengel. Intelligent monitoring of ball bearing conditions. *Mechanical Systems and Signal Processing*, 6(5):419–431, 1992.

[56] A. Madhusudhanan, M. Corno, M. Arat, and E. Holweg. Load sensing bearing based road-tyre friction estimation considering combined tyre slip. *Mechatronics*, 39:136–146, 2016.

[57] A. Madhusudhanan, M. Corno, and E. Holweg. Vehicle sideslip estimator using load sensing bearings. *Control Engineering Practice*, 54:46–57, 2016.

[58] H.A. Mol, S. Van Ballegooij, and J.M. Storken. Load determining system for a rolling element bearing. U.S. Patent App. 15/106,345, 2016.

[59] H.A. Mol and G.C. Van Nijen. Method and sensor arrangement for load measurement on rolling element bearing. U.S. Patent No. 7,444,888, 2008.

[60] A. Morhain and D. Mba. Bearing defect diagnosis and acoustic emission. *Proceedings of the Institution of Mechanical Engineers, Part J: Journal of Engineering Tribology*, 217(4):257–272, 2003.

[61] B. Muruganatham, M. Sanjith, B. Krishnakumar, and S. Satya Murty. Roller element bearing fault diagnosis using singular spectrum analysis. *Mechanical Systems and Signal Processing*, 35(1–2):150–166, 2013.

[62] I. Nakhimovski. *Modeling and simulation of contacting flexible bodies in multibody systems.* PhD thesis, Institutionen för datavetenskap, 2002.

[63] I. Nakhimovski. *Contributions to the modeling and simulation of mechanical systems with detailed contact analyses.* PhD thesis, Linköping University Electronic Press, 2006.

[64] K. Nam. Application of novel lateral tire force sensors to vehicle parameter estimation of electric vehicles. *Sensors*, 15(11):28385–28401, 2015.

[65] M. Nässelqvist, R. Gustavsson, and J. O. Aidanpää. Bearing load measurement in a hydropower unit using strain gauges installed inside pivot pin. *Experimental mechanics*, 52(4):361–369, 2012.

[66] A. Nembhard, J. Sinha, A. Pinkerton, and K. Elbhbah. Combined vibration and thermal analysis for the condition monitoring of rotating machinery. *Structural Health Monitoring*, 13(3):281–295, 2014.

[67] K. Nishikawa. Hub bearing with integrated multi-axis load sensor. *Technical Review*, 2011.

[68] NSK. Hub unit bearings. *http://www.bearing.co.il/E4201.pdf*, NSK, 2019.

[69] N. Ohkubo, T. Horiuchi, O. Yamamoto, and H. Inagaki. Brake torque sensing for enhancement of vehicle dynamics control systems. Technical Report 0148-7191, SAE Technical Paper, 2007.

[70] K. Ono, T. Takizawa, and M. Aoki. Preload measuring device for double row rolling bearing unit. U.S. Patent No. 8,864,382. 2014.

[71] H. Pacejka. *Tire and vehicle dynamics.* Elsevier, 2005.

[72] C. Peeters, P. Guillaume, and J. Helsen. A comparison of cepstral editing methods as signal pre-processing techniques for vibration-based bearing fault detection. *Mechanical Systems and Signal Processing*, 91:354–381, 2017.

[73] Z. Peng and N. Kessissoglou. An integrated approach to fault diagnosis of machinery using wear debris and vibration analysis. *Wear*, 255(7):1221–1232, 2003.

[74] A. Pohl, R. Steindl, and L. Reindl. The" intelligent tire" utilizing passive saw sensors measurement of tire friction. *IEEE transactions on instrumentation and measurement*, 48(6):1041–1046, 1999.

[75] F. Pretagostini, L. Ferranti, G. Berardo, V. Ivanov, and B. Shyrokau. Survey on wheel slip control design strategies, evaluation and application to antilock braking systems. *IEEE Access*, 8:10951–10970, 2020.

[76] F. Pretagostini, B. Shyrokau, and G. Berardo. Anti-lock braking control design using a nonlinear model predictive approach and wheel information. In *2019 IEEE International Conference on Mechatronics (ICM)*, volume 1, pages 525–530. IEEE, 2019.

[77] L. Rasolofondraibe, B. Pottier, P. Marconnet, and X. Chiementin. Capacitive sensor device for measuring loads on bearings. *IEEE Sensors Journal*, 12(6):2186–2191, 2012.

[78] L. R. Ray. Nonlinear tire force estimation and road friction identification: simulation and experiments. *Automatica*, 33(10):1819–1833, 1997.

[79] A. Reedman and H. Yang. Bearing monitoring using a fibre bragg grating. U.S. Patent No. 8,790,013. 2014.

[80] J. Reichel, R. Eisenkolb, and F.H.I. Ebhart. Roadyn™-ein entwicklungswerkzeug für felge und radaufhängung. 2002.

[81] A. Rupp and V. Grubisic. Reliable determination of multi-axial road loads and tire deformations on buses and heavy trucks for the design and proof out. Technical Report 0148-7191, SAE Technical Paper, 1997.

[82] A. Rupp, V. Grubisic, and J. Neugebauer. Development of a multi-component wheel force transducer-a tool to support vehicle design and validation. Technical Report 0148-7191, SAE Technical Paper, 1993.

[83] B. Shyrokau, D. Wang, D. Savitski, K. Hoepping, and V. Ivanov. Vehicle motion control with subsystem prioritization. *Mechatronics*, 30:297–315, 2015.

[84] K. B. Singh and S. Taheri. Integrated state and parameter estimation for vehicle dynamics control. *International journal of vehicle performance*, 5(4):329–376, 2019.

[85] SKF. Skf hub bearing units for automotive and industrial applications, SKF, 2015.

[86] L. Stacke and D. Fritzson. Dynamic behaviour of rolling bearings: simulations and experiments. *Proceedings of the Institution of Mechanical Engineers, Part J: Journal of Engineering Tribology*, 215(6):499–508, 2001.

[87] L. Stacke, D. Fritzson, and P. Nordling. Beast—a rolling bearing simulation tool. *Proceedings of the Institution of Mechanical Engineers, Part K: Journal of Multi-body Dynamics*, 213(2):63–71, 1999.

[88] T. Stoferle and W. Sack. Arrangement for measuring and/or monitoring an axial force. U.S. Patent No. 4,168,160, 1979.

[89] M. Suzuki, K. Nakano, A. Miyoshi, A. Katagiri, and M. Kunii. Method for sensing tire force in three directional components and vehicle control using this method. Technical Report 0148-7191, SAE Technical Paper, 2007.

[90] N. Tandon and A. Choudhury. A review of vibration and acoustic measurement methods for the detection of defects in rolling element bearings. *Tribology international*, 32(8):469–480, 1999.

[91] A. Tuononen and L. Hartikainen. Optical position detection sensor to measure tyre carcass deflections in aquaplaning. *International Journal of Vehicle Systems Modelling and Testing*, 3(3):189–197, 2008.

[92] A. J. Tuononen, M. Ovaska, and A. Niskanen. Review on tire-road-friction potential estimation technologies. In *The IAVSD International Symposium on Dynamics of Vehicles on Roads and Tracks*, pages 1027–1032. Springer, 2019.

[93] S. van Aalst. *Virtual Sensing for Vehicle Dynamics*. PhD thesis, 2020.

[94] H. van der Knokke, R. Wunderlich, K. Hauser, and R. Hollweck. Force-sensing bearing. U.S. Patent No. 7,316,168. 2008.

[95] J. Van Doornik. Haptic feedback on the steering wheel near the vehicle's handling limits using wheel load sensing. Master's thesis, Delft University of Technology, 2014.

[96] E. van Genuchten and L. Kahlman. Fiber optical sensing of bearing performance and pump conditions. In *Proceedings of the 33rd International Pump Users Symposium*. Turbomachinery Laboratory, Texas AM Engineering Experiment Station, 2017.

[97] C. Wagner, A. Krinner, T. Thümmel, and D. Rixen. Full dynamic ball bearing model with elastic outer ring for high speed applications. *Lubricants*, 5(2):17, 2017.

[98] E. A. Wan and R. Van Der Merwe. The unscented kalman filter for nonlinear estimation. In *Proceedings of the IEEE 2000 Adaptive Systems for Signal Processing, Communications, and Control Symposium (Cat. No. 00EX373)*, pages 153–158. Ieee, 2000.

[99] T. Williams, X. Ribadeneira, S. Billington, and T. Kurfess. Rolling element bearing diagnostics in run-to-failure lifetime testing. *Mechanical Systems and Signal Processing*, 15(5):979–993, 2001.

[100] Y. Xiong and A. Tuononen. A laser-based sensor system for tire tread deformation measurement. *Measurement Science and Technology*, 25(11):115103, 2014.

[101] T. Yanagisawa, K. Matsuoka, I. Sakatani, and S. Kumagai. Load-measuring device for rolling bearing unit and rolling bearing unit for load measurement. U.S. Patent No. 7,212,927. 2007.

[102] X. Zhu, C. Zhong, and J. Zhe. Lubricating oil conditioning sensors for online machine health monitoring–a review. *Tribology International*, 2017.

Propositions

1. Load measurement allows for improved performance and safety margins for intelligent vehicles (this thesis)
2. A physical model based approach provides a more robust and accurate solution for bearing load measurement than a data driven approach (this thesis)
3. It is the change of states that must be understood and processed for accurate bearing load measurement (this thesis)
4. Measurement is the quantization of a physical effect, and as such it has considerable implications to our interpretation of the actual effect
5. Thermal gradients negatively affect bearing load reconstruction, likewise they negatively affect the productivity of people at work
6. As our work evolves and increases in effectivity, so should the spending of our time
7. The growing institutionalization of our University challenges the core academic values of independence and responsibility
8. The ease in which context is overlooked in modern society is problematic is many ways, but in particular as it is often context that provides meaning and value to events
9. Globalization serves the few while tricking the many
10. In pursuit of happiness, one should focus on personal development over success

Deze stellingen worden opponeerbaar en verdedigbaar geacht en zijn als zodanig goedgekeurd door de promotor dr. Ir. R. Happee en copromotor dr. B. Shyrokau.